Structural and functional studies of oxygen-evolving photosystem II

March, 2019

Yoshiki Nakajima

The Graduate School of

Natural Science and Technology

(Doctor's Course)

OKAYAMA UNIVERSITY

ABBREVIATIONS

ATP: adenosine 5' –triposphate

Chl *a*: chlorophyll *a*

Cyt: cytochrome

D1: reaction center binding polupeptide of PSII, a product of *psbA* gene

D2: reaction center binding polupeptide of PSII, a product of *psbD* gene

DCMU: 3-(3,4-dichlorophenyl)-1, demethylurea

DDM: n-dodecyl-β-d-maltoside

DGDG: digalactosyl-diacylglycerol

DL : delayed light emission

DMSO: dimethyl sulfoxide

Hepes: 2-[4-(2-hydroxyethyl)-1-piperazinyl] ethanesulfonic acid

HTG: heptyl-β-D-thioglucoside

LDAO: laulyldimethylamin-N-oxide

LHC: light harvest complex

Mes: 2-(N-morpholino)ethanesulfonic acid

MGDG: monogalactosyl-diacylglycerol

NADP: nicotineamide adenine dinucleotide phosphate

OEC: oxygen evolving complex

PEG: polyethylene glycol

Pheo: pheophytin

PG: phophatidyl-glycerol

PQ: plastoquinone

PSI: photosysytem I

PSII: photosystem II

SFX: serial femtosecond crystallography

SQDG: sulfoquinovosyl-diacylglycerol

TL: thermoluminescence

XFEL: X-ray free electron laser

Y_D: tyrosine D (D2Y160)

INDEX

General introduction

1. Photosynthetic light energy conversion reactions 6
2. History of crystal structure analysis in PSII 9
3. Crystal structure of PSII dimer complex and feature of each subunit 10
4. Structure and function of the Mn_4CaO_5 cluster 12
5. Hydrogen bond networks in PSII 14
6. Cofactors of PSII 15
7. Research contents of this study 17
8. REFERENCES 19

Chapter 1. Optimization of micro-crystallization for crystal structure analysis of intermediate state of PSII

1. ABSTRACT 22
2. INTRODUCTION 23
3. MATERIALS AND METHODS 24
Cell culture and purification 24
Oxygen evolution 25
Clear Native PAGE 26
Micro-crystallization 26
1) Pipetting method 26
2) Seeding method 26
3) Tube vortex method 27
Procedure of cryoprotectant treatment 27
Screening of grease 28
Optimization of the condition of cryoprotection 28
Resolution check of crystals treated by several conditions in SPring-8 28
4. RESULTS 29
Purity and activity of the PSII dimers 29

Optimization of method of micro-crystallization and screening of optimal kinds of grease 30
Optimization of the conditions for the treatment of cryoprotectants 34
Structural changes induced by 2-flash illumination 39
5. DISCUSSIONS 42
6. REFFERENCES....44

Chapter 2. Effects of cryo-protectants on the efficiency of S-state transitions of oxygen-evolving photosystem II

1. ABSTRACT 47
2. INTRODUCTION....48
3. MATERIALS AND METHODS 49
Cell culture and purification 49
Thermoluminescence analysis....49
O_2 evolving activity 49
4. RESULTS.... 50
TL analysis in PSII dimer treated by high concentration of PEG and glycerol 50
Comparison of TL curves between PSII samples treated with high concentrations of glycerol or DMSO....51
Effects of the treatment with the high concentration of DMSO on O_2 evolution activity 52
5. DISCUSSIONS 55
6. REFFERENCES....58

Chapter 3. Thylakoid membrane lipid sulfoquinovosyl-diacylglycerol (SQDG) is required for full functioning of photosystem II in *Thermosynechococcus elongatus*

1. ABSTRACT 61
2. INTRODUCTION....62
3. MATERIALS AND METHODS 65
Cell culture and purification 65
Clear Native PAGE and gel-filtration chromatography 66
Oxygen evolution, TL and DL measurements....67

FTIR measurements.....67
Lipid analysis.....68
Crystallization and structural analysis.....68
4. RESULTS.....69
Analyses on the content of PSII dimer and oxygen evolution.....69
Clear Native PAGE (CN-PAGE) and gel-filtration chromatography.....71
Spectroscopic analyses (TL, FTIR and DL measurements) of the PSII activities.....72
Crystal structure analysis of the ΔSQDG-PSII dimer.....75
Lipid content of the mutant PSII dimer.....76
Structural changes caused by the depletion of SQDG.....81
5. DISCUSSIONS.....85
6. REFFERENCES.....88

GENERAL CONCLUSIONS.....92
REFFERENCES.....94
ACKOWLDGEMENTS.....95

General introduction

1. Photosynthetic light energy conversion reactions

Molecular oxygen (O_2) in the atmosphere starts to accumulate owing to the birth of ancient oxygen-evolving photosynthetic organisms cyanobacteria around 30 billion years ago (1). The dramatic increase of oxygen in the atmosphere occurred in 23-25 billion years ago enabled the birth and evolution of aerobic lives on the earth, involving the ancestor of ourselves (2–4). Thus, photosynthesis is one of the most important natural chemical reactions, because this process converts light energy into the form of chemical energy that sustains almost all life forms on the earth, and produces O_2 that sustains aerobic lives. The overall reaction of photosynthesis is represented by the following equations [1].

$$2\ H_2O + 4\ \text{photons} \longrightarrow O_2 + 4\ e^- + 4\ H^+$$
$$4\ e^- + 4\ H^+ + CO_2 \longrightarrow [CH_2O]_n + H_2O \qquad [1]$$

The above reactions are driven by the energy of sun light converted through a series of pigment-protein complexes located in the thylakoid membranes of photosynthetic organisms (Fig.0-1A). The light energy is first absorbed by pigments such as chlorophyll (Chl), carotenoids and phycobilins, etc, associated with various light-harvesting complexes (LHC), resulting in the excitation of these pigments. These light-harvesting antenna proteins surround the photosystem I (PSI) and II (PSII) reaction centers closely, and can transfer the excitation energy effectively to the reaction centers. Different types of light-harvesting antennae are found in different photosynthetic organisms. In green algae and higher plants, membrane-spanning LHCI and LHCII are found to associate with the PSI and PSII reaction centers respectively (5–7), whereas in cyanobacteria, water-soluble phycobilisome proteins are used as the light-harvesting antenna of PSII (8). In the primitive eukaryotic red algae, phycobilisome is the major antenna of PSII whereas membrane-spanning LHCI is the major antenna of PSI (9, 10).

The excitation energy reached the core antenna of PSII finally excites the special pair Chl, P680, resulting in the formation of the excited singlet state P680*. Electron is separated from the excited P680* and transferred to the secondary quinone acceptor Q_B through $Pheo_{D1}$ and Q_A. After two-electron reduction, Q_B is converted to a plastoquinole (PQH_2) molecule by taking in two protons from the stromal side. PQH_2 is then released from its binding-site and transferred to the plastoquinone pool located in the

interior of the thylakoid membrane. On the other hand, after transferring the electron to the accepter side, P680* became $P680^+$ and is reduced to its original state P680 by extracting an electron from Tyr_Z, a tyrosine residue of the D1 subunit (D1-Tyr161) located close to P680. The oxidized Tyr_Z in turn extracts electrons from a Mn_4CaO_5-cluster, which is the catalytic center for water-splitting. After four electrons are extracted from the Mn_4CaO_5-cluster sequentially, two water molecules are split into 4 electrons, 4 protons and 1 molecule of oxygen.

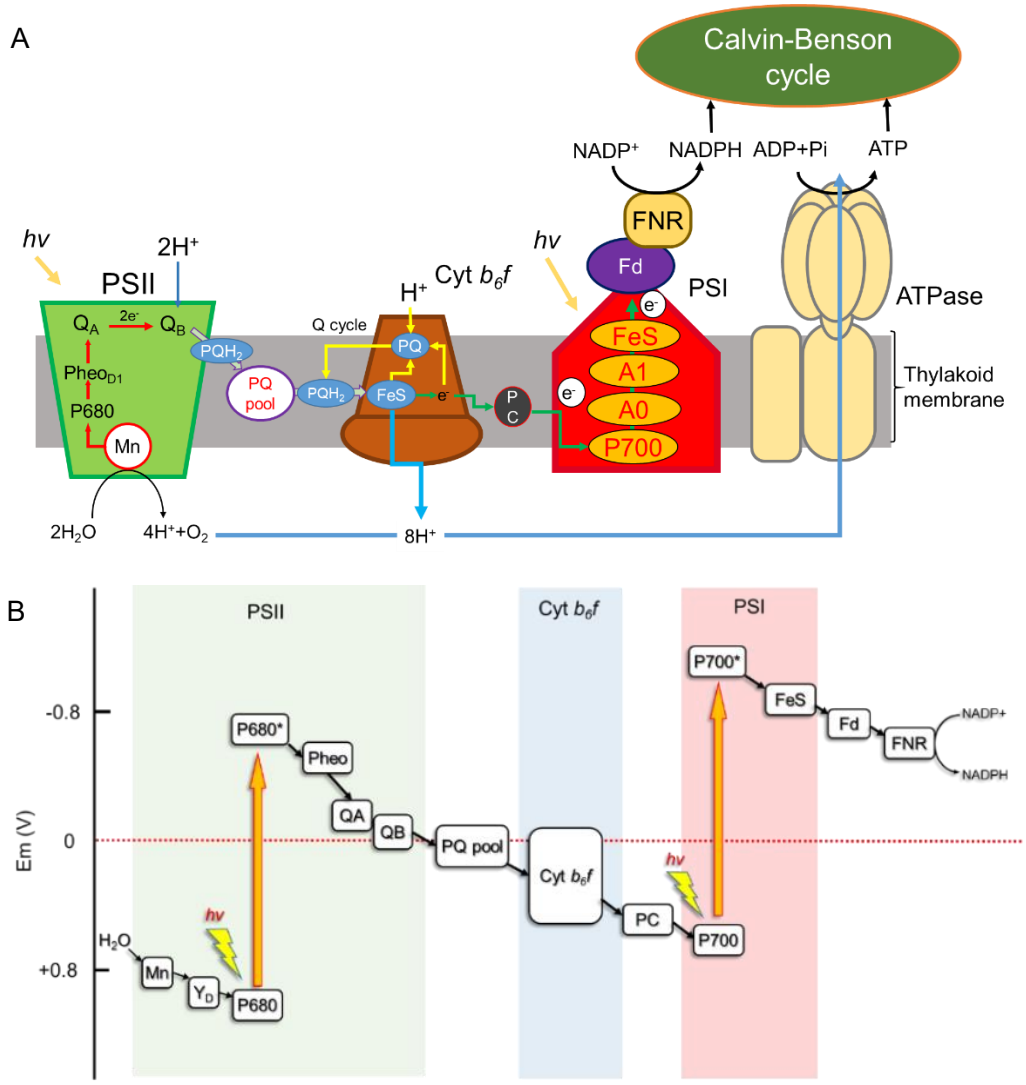

Fig. 0-1. A, Overall view of the photosynthetic light energy conversion reactions occurring in the thylakoid membrane. B, The Z-scheme for the electron transfer of oxygenic photosynthesis.

PQH_2 released from PSII is oxidized by the cytochrome (Cyt) *b_6f* complex from which, the electrons released are transferred to the mobile electron carrier plastocyanin (PC), and the protons are released to

the luminal side, contributing to the formation of the proton gradient across the membrane. Meanwhile, the oxidized PQ binds to another binding cavity (Qx site) of the Cyt *b*$_6$*f* complex located at the stromal side, which takes in protons from the stromal side upon protonation. This proton transfer cycle from the stromal side to the lumen side via quinone is called Q-cycle, which contributes to the formation of the proton gradient between the inner and outer sides of thylakoid membrane and provides driving force for ATP synthesis by the ATP synthase (ATPase) (11).

The reduced PC moves from Cyt *b*$_6$*f* to PSI, and transfers electrons to PsaF, one of the PSI subunits, within the membrane of the luminal side. The positively charged region of the PsaF subunit and negatively charged region of PC can interact with each other by Coulomb force to facilitate the electron transfer. The core of the PSI reaction center is also a special pair of Chls called P700, which is excited to the singlet state P700* upon excitation by the light energy from the PSI antenna proteins. The excited P700* transfers an electron to the acceptor side of PSI, producing the oxidized state Chl $P700^+$. $P700^+$ returns to P700 by accepting an electron from PC. On the other hand, electrons released from P700* are transferred to ferredoxin (Fd) containing a Fe-S cluster at the stromal side via phylloquinones, Q_K-A, Q_K-B. Fd donates electrons to nicotine amide dinucleotide phosphate (NADP) in Fd:$NADP^+$ reductase (FNR), where two electrons transferred from Fd and one proton taken from the stromal side are utilized for the synthesis of NADPH. The NADPH formed is released to the stromal side and provides the reduction power for the fixation of CO_2 into carbohydrates. ATP is also an indispensable factor for the fixation of CO_2 and is synthesized by the ATP synthase (ATPase) located in the thylakoid membrane. ATP synthesis by the ATPase is driven by the H^+ gradient formed across the thylakoid membrane generated by the water splitting reaction of PSII and the Q-cycle of Cyt *b*$_6$*f* as described above. When protons are passed from the lumenal side to the stromal side via transmembrane subunit of ATPase, a huge complex containing six subunits ($\alpha_3\beta_3$ complex) located at the stromal side are rotated, which is caused by rotation of the γ-subunit in the transmembrane region as a pivot of these subunits. Upon a rotation of 240 degrees, the β subunit synthesizes ATP from ADP and phosphoric acid (Pi) (12). The ATP and NADPH produced above are then utilized for producing glucose in the Calvin-Benson cycle.

Fig. 0-1B represents a conceptual diagram that indicates electron flow and redox potential from PSII to PSI in photosynthesis (Z-scheme) (13). The series of this reaction starts from the splitting of water, and ends at the reduction of $NADP^+$ to NADPH, which is utilized for the conversion of CO_2 to carbohydrates. Light energy from the sun is utilized to drive this reaction. Thus, the essence of these

reactions is the conversion of light energy into the form of chemical energy that can be used by various organisms.

2. History of crystal structure analysis of PSII

The structure and functions of PSII have been studied extensively, owing to the important function of PSII to split water to produce O_2 molecules indispensable for all aerobic lives on the earth. Since water is a very sable molecule, it requires a huge amount of energy to split it to produce molecular O_2. PSII is able to split water under ambient pressure and temperature by the use of sun light, but its mechanism has remained obscure for many years, which is largely due to the fact that the atomic structure of PSII and the water oxidation complex (WOC) it contains remained unsolved until recently.

To solve the atomic structure of PSII and WOC, X-ray crystallography is the only possible method that can be used, since PSII is an extremely large membrane-protein complex. For example, the PSII core complex from cyanobacteria contains 20 different subunits with a molecular mass of 350 kDa, and it exists as a dimer with a total molecular mass of 700 kDa. In order to solve the structure of PSII by X-ray crystallography, it has to be crystallized. The first report on the crystallization and crystal structure analysis of PSII was made by Zouni et al. in 2001, who solved the structure of PSII dimer from a thermophilic cyanobacterium *Thermosynechococcus elongates* (*T. elongates*) at 3.8 Å resolution (14). Kamiya and Shen subsequently reported the structure of PSII dimer from another thermophilic cyanobacterium *T. vulcanus* at 3.7 Å resolution in 2003 (15). The crystallization method and conditions were continuously improved, which led to the structure analysis of PSII at 3.0 Å resolution in 2005 (16) and 2.9 Å resolution in 2009 (17). These structure analyses identified all of the subunits and their positions in PSII, and the locations and structures of most cofactors. However, there are still some cofactors and amino acid side chains whose orientations and positions are not clearly defined at these levels of resolutions. In particular, the detailed structure of the catalytic center for water-splitting, namely, the Mn_4CaO_5-cluster, could not be defined, since the position of each atom in this cluster is not clearly located due to the ambiguous electron densities. In 2011, the crystal quality of PSII dimers was dramatically improved, which led to the crystal structure analysis at 1.9 Å resolution (18). This crystal structure clearly showed the electron density distributions for each atom within the Mn_4CaO_5-cluster, thus providing the first atomic structure of the Mn_4CaO_5-cluster. Although this structure showed a cubane-like organization of the Mn_4CaO_5-cluster as already reported in the 3.5 Å resolution structure

previously by Ferreira et al (19), the cubane is not a regular hexahedron but a distorted one (see below), which may have important functional implications.

3. Crystal structure of PSII dimer complex and features of each subunit

The crystal structure of the PSII dimer derived from the thermophilic cyanobacterium *T. vulcanus* at 1.9 Å resolution is shown in Fig. 0-2 (18). The PSII complex consists of 19 subunits; PsbA (D1), PsbB (CP47), PsbC (CP43), PsbD (D2), PsbE (Cyt b_{559} α subunit), PsbF (Cyt b_{559} β subunit), PsbH, PsbI, PsbJ, PsbK, PsbL, PsbM, PsbO, PsbT, PsbU, PsbV (Cyt c_{550}), PsbX, PsbZ, Psb30 (ycf 12) (Fig. 0-2). The PsbY subunit was not found and is likely to be dissociated from PSII in the crystal, although it remained in the Sr-substituted structure of PSII reported later (20).

The PSII reaction center subunits D1 and D2 are located at the center of a PSII monomer and bind all of the electron transfer cofactors of PSII. These two subunits have five transmembrane helices each, and adopt a pseudo *C2*-symmetric structure. The Mn_4CaO_5-cluster and most of the electron transfer cofactors are localized in the D1 subunit, but the primary electron accepter, the first bound plastoquinone acceptor Q_A is bound to the D2 subunit. CP43 and CP47 are two large trans-membrane subunits that enclose the D1 and D2 hetero dimer and play a role as core antenna protein complex. Each of these two subunits has six transmembrane helices, and binds a number of Chls, which mediates excitation energy transfer from the peripheral antenna proteins, LHCII or phycobilisome to P680 in the D1 subunit. Among the low molecular weight subunits, the roles of PsbE and PsbF subunit (Cyt b_{559}) is not clearly defined yet. It has been suggested that Cyt b_{559} could have a role in protection against photoinhibition caused by absorption of excess excitation energy that will result in the singlet oxygen formation and damage of the protein structure (21). Cyt b_{559} may be involved in a secondary electron transfer pathway to dissipate the excess energy, thus protecting PSII from photo-damage. PsbM, PsbL and PsbT subunits are located in the monomer-monomer interface of the PSII dimer, suggesting that these subunits may maintain the dimer formation or stability. In PsbM or PsbT(c) deletion mutants, the PSII activity, assembly and accepter side properties were affected (22), and deletion of PsbL showed more severe effects (23), suggesting the roles of these subunits in maintaining the PSII dimer stability and activity.

Among the PSII subunits, most of the transmembrane subunits are highly conserved from prokaryotic cyanobacteria to eukaryotic higher plants, but the composition of peripheral proteins has been changed during their evolution. Among the peripheral proteins, PsbO is commonly bind to PSII

from prokaryotic to eukaryotic organisms, whereas PsbV and PsbU are found in the cyanobacterial PSII but PsbP and PsbQ are found in green algal and higher plant PSII. In red algae, PsbQ', a homologous protein to green algal and higher plant PsbQ, is present in addition to PsbV and PsbU.

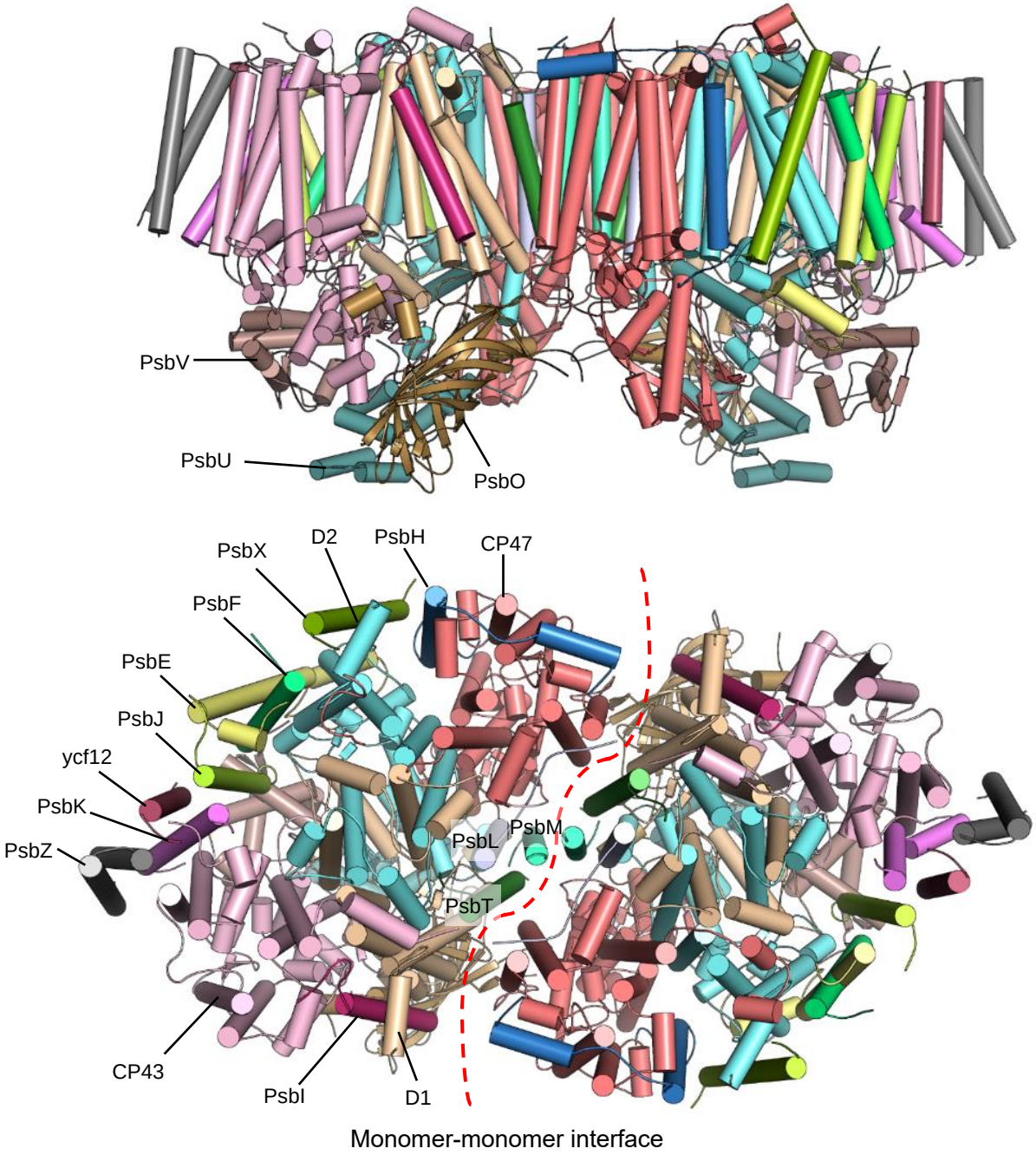

Fig. 0-2. Structure of the PSII dimer at 1.9 Å resolution (PDB code; 3WU2). (A) Side view; **(B)** Top view from the stromal side. All helices were illustrated in the cylindrical mode by Pymol.

4. Structure and function of the Mn_4CaO_5 cluster

The detailed structure of the Mn_4CaO_5-cluster, the catalytic center for water-splitting in PSII (oxygen-evolving center, OEC), was first reported by the structure analysis of PSII at 1.9 Å resolution, which showed that this cluster has a distorted shape (Fig. 0-3A) (18). In this distorted structure, three Mn ions and one Ca are linked by four oxo-bridged oxygen atoms to form a distorted cubane, and the forth Mn is located outside of the cubane and linked with the cubane by two μ-oxo bridges. The cluster is coordinated by 7 amino acid residues, with the Ca ion and the forth Mn ion have two terminal water ligands, respectively. This structure, however, was solved by strong synchrotron radiation X-rays, which was suggested to cause X-ray radiation damages to the metal cluster. Because the X-ray radiation damages are likely to cause the elongation of the bond lengths between each atom in the Mn_4CaO_5-cluster including those between metal atoms, it was difficult to judge that the structure of the distorted Mn_4CaO_5-cluster solved indeed represents the native state or has been changed due to the X-ray radiation damages. In order to solve the radiation damage–free structure of the Mn_4CaO_5-cluster, Suga et al. collected diffraction data from PSII crystals by using femtosecond X-ray free electron lasers (XFEL). XFEL provides X-ray pulses with an intensity 100 trillion times as strong as that provided by synchrotron X-rays in an extremely short pulse time, 10 femtosecond, at the XFEL facility SACLA, Japan. These extremely strong and short X-ray pulses make it possible to collect diffraction images before X-ray radiation damage occurs to cause structural changes of the proteins, which usually occurs in the picosecond time range. Using this approach and a large number of large, well-diffracting and highly isomorphous PSII crystals, the damage-free structure of PSII was solved at 1.95 Å resolution (24). This structure showed a similar distorted structure of the Mn_4CaO_5-cluster in which, some of the Mn-Mn and Mn-ligand distances were shortened by 0.1-0.3 Å (Fig. 0-3B). The Mn-Mn bond lengths observed in the damage-free structure are in good agreement with the previous report from X-ray absorption fine structure measurement (XAFS) (25, 26) and theoretical calculation (27), suggesting that this structure represents the native state of the metal cluster.

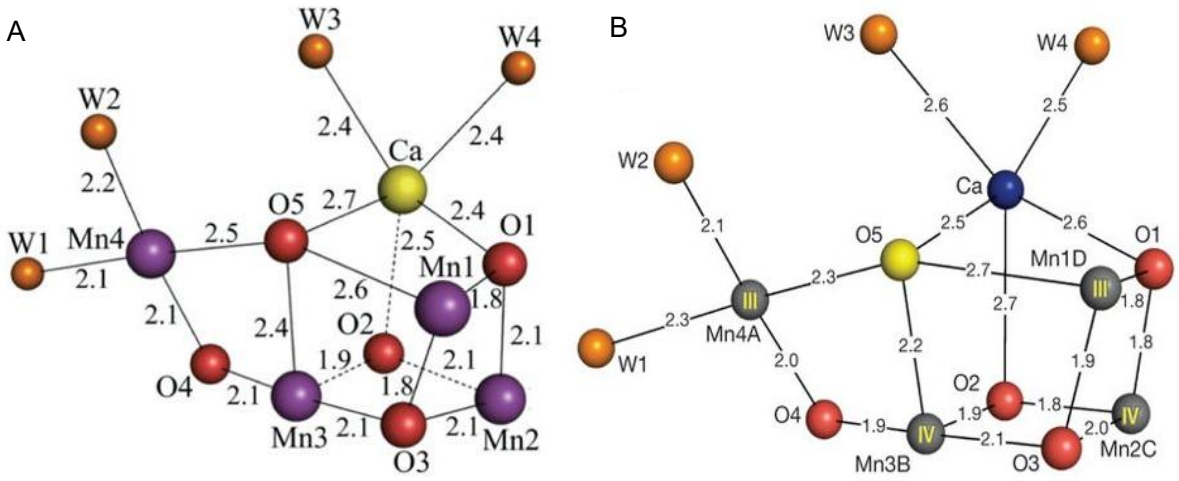

Fig. 0-3. Comparison of atomic distances in the Mn_4CaO_5-cluster between Synchrotron X-ray (18) (A) and XFEL structure (B) of PSII (24).

The distorted, asymmetric structure of the Mn_4CaO_5-cluster is caused by two reasons. One is the longer bond distance between Ca-O than the typical bond distances of Mn-O. The other one is a much longer bond length between O5 and its nearby Mn ions than the typical bond lengths of Mn-O, namely, the bond length of Mn1-O5 is 2.7 Å, Mn4-O5 is 2.3 Å, and Mn3-O5 is 2.2 Å, whereas the typical Mn-O bond lengths are in the range of 1.8-2.0 Å. Based on the existence of longer ligand distance pairs for Mn1 and Mn4, these two Mn ions are proposed to have a Jahn-Taller axis in the direction of Mn1-O5 and Mn4-O5, and therefore are in the +3 oxidation states. Consequently, Mn2 and Mn3 are in the +4 oxidation states in the S_1-state. Theoretical calculation based on XFEL structure of PSII (28) showed that the chemical species of O5 may be OH^-. The unusually longer bond distances between O5 and its nearby atoms (ions) suggest that the binding of O5 to the metal ions are very weak. Therefore, O5 may be cut out during the reaction cycle and provides one of substrate water molecules for O_2 evolution. Thus, the distorted structure of the Mn_4CaO_5-cluster makes it flexible and easy to undergo structural changes during the water-splitting catalytic process. After completion of the reaction cycle, the cluster will return to its original structure.

In the water splitting reaction, four protons and four electrons are extracted from two water molecules and a molecular oxygen is finally evolved. This process proceeds through the Kok cycle (Fig. 0-4) (29), where the Mn_4CaO_5-cluster is suggested to assume five intermediate states, S*i* (*i* = 0-4) and each state is advanced to the next state by one flash (1 photon). Among these states, the S_1-state is stable in

the dark and therefore is the start state for the O_2 evolution process. Both PSII crystal structures analyzed at 1.9 and 1.95 Å resolutions represent this S_1-state structure. During each transition except for the S_4-S_0 step (the O_2 evolution step), electrons are released one by one and O_2 molecule is finally formed after irradiation of first 3 flashed and every 4 flashes thereafter. The S_4-state is instantly transferred to the S_0-state without flash illumination.

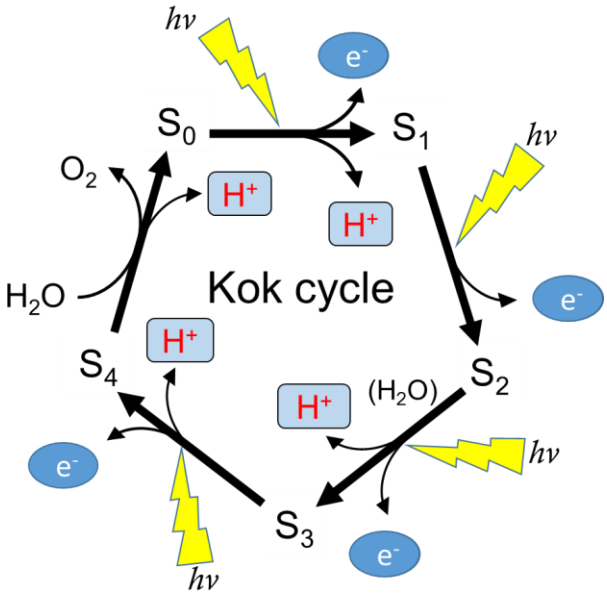

Fig. 0-4. Kok (S-state) cycle of the PSII water splitting reaction.

5. Hydrogen bond networks in PSII

Since the Mn_4CaO_5-cluser is embedded in the interior of the PSII protein complex and covered by a large area of hydrophilic protein region including the three extrinsic subunits and extra-membrane loops of D1, D2, CP47 and CP43, the four protons generated by the water-splitting reaction must be exported through these regions to the outside lumenal space effectively. Otherwise, localization of excess protons at the catalytic site will remarkably decrease the local pH and hence destroy the structure of the Mn_4CaO_5-cluster. Several hydrogen-bonding networks starting from the Mn_4CaO_5-cluster to the lumenal space have been found in the high-resolution structures of PSII, which may mediate effective proton transport. These hydrogen-bonding networks consist of a number of water molecules fixed by hydrophilic residues; protons may be transported by the sequential protonation and deprotonation of these residues and water molecules. One of the hydrogen-bonding networks starts at the Mn_4CaO_5-

cluster and is connected to the peripheral subunit, PsbV via Yz (D1-Tyr161). Because Yz functions to extract electrons from Mn_4CaO_5-cluster and donates them to $P680^+$, this pathway is called "proton-coupled electron transfer pathway". The 1.9 Å resolution structure of PSII showed that Yz forms a hydrogen bond with a water molecule bound to the Ca atom of Mn_4CaO_5-cluster and simultaneously hydrogen-bonds with D1-His190 in the opposite side. This hydrogen-bond network is finally connected to PsbV-Lys129 facing to the cavity of the lumenal side. Thus, protons may be released to the lumenal side through this network. In addition to this pathway, hydrogen-bonding networks from D1-Asp61 to PsbO via a Cl^- ion, from O4 to PsbU and from O1 to PsbV via D1-Glu329 and Yz are also proposed (18, 30, 31). The path via the Cl^- ion has also been suggested to play a role as a pathway for substrate water inlet for O_2 evolution.

6. Cofactors of PSII

The high-resolution crystal structure of PSII showed that it contains 35 Chls, two pheophytins, 11 β-carotenes, more than 20 lipids, two plastoquinones, two haem irons, one non-haem iron and one bicarbonate ion, as cofactors. Chl *a* is found in all oxygenic photosynthetic organisms, whereas other kinds of Chls may be present in different organisms. Most of the Chls function as antenna pigments and a few function in charge separation and electron transfers in the reaction center as described above. Pheophytin is synthesized by the detachment of Mg ion from the Chl *a* molecule and serves as the first electron accepter from excited P680*. The haem irons are present in Cyt b_{559} (PsbE and F) and Cyt c_{550} (PsbV). The function of Cyt b_{559} has been suggested to prevent formation of active oxygen species by quenching the excess excitation energy into the form of heat energy as described above. To fulfill this role, Cyt b_{559} is suggested to form a cyclic electron transfer pathway via plastoquinone electron acceptors.

The thylakoid membranes of photosynthetic organisms contain mainly three types of glycolipids and one types of phospholipid, namely monogalactosyl-diacylglycerol (MGDG), digalactosyl-diacylglycerol (DGDG), sulfoquinovosyl-diacylglycerol (SQDG) and phosphatidyl-glycerol (PG) (Fig. 0-5). These lipid compositions are largely conserved among different species. In the crystal structure of PSII, 6 MGDG, 5 DGDG, 4 SQDG and 5 PG were found per PSII monomer (18). MGDG and DGDG are nonionic lipids, and their head groups are basically oriented toward the lumenal side. On the other hand, SQDG and PG are anionic lipids, and their head groups are oriented toward the stromal side (Fig. 0-6). The nonionic lipids may mainly function as a scaffold for membrane proteins by formation of the

lipid bilayer, whereas the anionic lipids may function to maintain the balance of negative charges in the surface of the membrane. The biosynthesis of these lipids have been well-studied by deletion mutations of various lipid synthase.

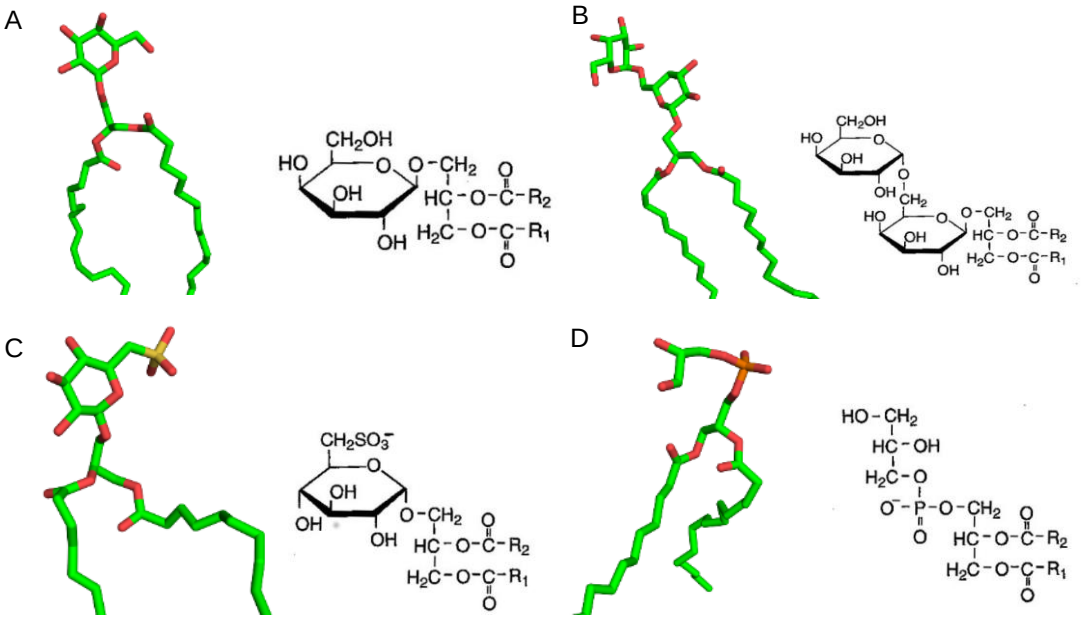

Fig. 0-5. Structures of lipid molecules found in PSII. (A) MGDG; (B) DGDG; (C) SQDG; (D) PG.

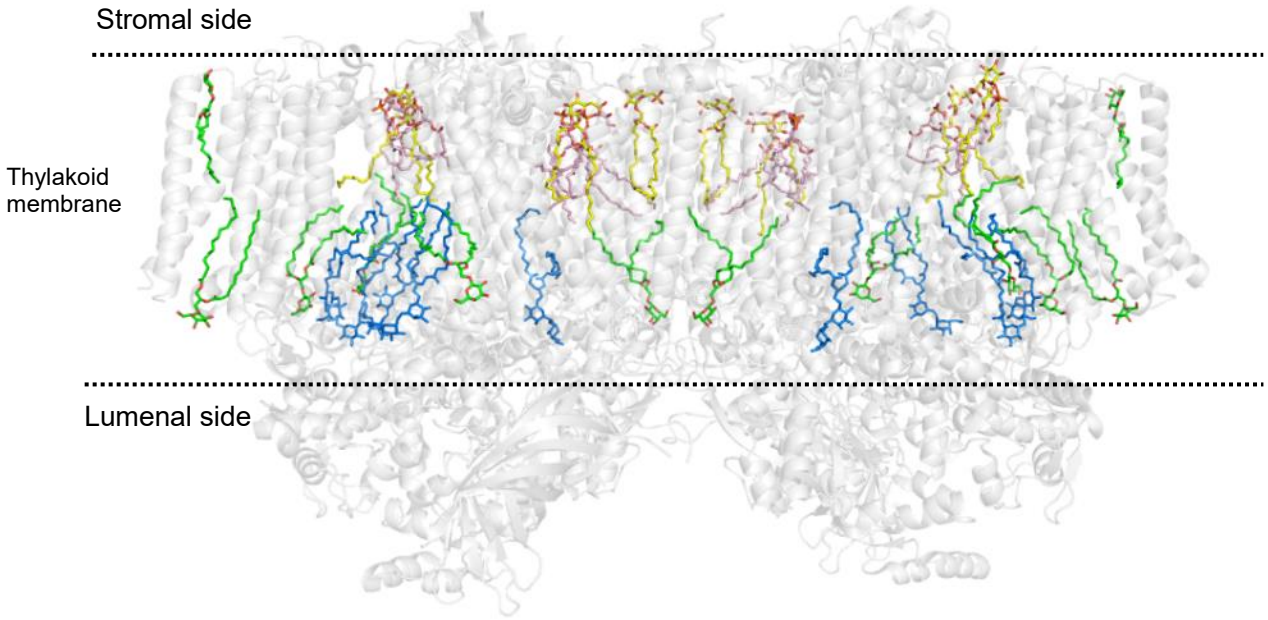

Fig. 0-6. Lipid arrangement in the PSII dimer. MGDG, DGDG, SQDG and PG were depicted by green, blue, yellow and pink sticks, respectively.

7. Research contents of this study

The high resolution crystal structure of PSII dimer revealed not only the detailed structure of the Mn_4CaO_5-cluster but also the presence and structure of several new cofactors including the lipid molecules. To fully understand the mechanism of the water-splitting reaction, however, the structures of four intermediate S-states need to be solved. In addition, the functions of a number of cofactor molecules, including those of the lipid molecules need to be clarified.

In chapter 1, I prepared high-quality PSII micro-crystals to be used for serial femtosecond crystallography with a pump-probe method to determine the intermediate structures of PSII. In order to obtain the high-quality PSII micro-crystals, I established the method of micro-crystallization and screened, improved the post-crystallization conditions. With the methods and conditions established, PSII micro-crystals diffracting to a highest resolution of 2.1 Å were obtained, which led to the determination of 2-flashes induced S_3-state structure of PSII at 2.35 Å resolution. In this structure, a new oxygen atom (O6) was found to be inserted into a position close to O5, suggesting the formation of an O=O bond between O5 and O6.

In chapter 2, to examine the effects of cryoprotectant reagents on the PSII activity, thermoluminescence (TL) was used to monitor the PSII activity under several different cryoprotectant conditions. The results showed that the cryoprotectant condition utilized in the SFX experiment decreased the transition efficiency of the S-state cycle. Furthermore, glycerol used as one of the cryoprotectants caused an upshifted of the TL-peak temperature and appearance of an additional peak, whereas this effect was mitigated by replacement of glycerol with dimethyl sulfoxide DMSO. In the 20% DMSO and PEG condition, the efficiency of S-state transition gradually decreased upon increase of the PEG concentration, indicating that the high concentration of PEG also affected the S-state transition efficiency. Taken together, the results indicate that it would be difficult to analyze the crystal structure of the S-state beyond the S_3-state under the current cryoprotectant condition containing a high concentration of PEG, and screening of new cryoprotectant conditions giving rise to a high transition efficiency will be essential in the future.

In chapter 3, the crystal structure and function of a PSII mutant unable to synthesize SQDG by deleting the SQDG-synthesis gene *sqdB* from *T. elongatus* (ΔSQDG-PSII) were analyzed. SQDG deletion caused a slight decrease in the O_2 evolving activity and cell growth rate as well as an increase in the content of PSII and PSI monomers. The function of purified ΔSQDG-PSII was analysed by

Fourier-transform infra-red (FTIR), delayed luminescence (DL) and TL measurements, and it was found that the exchange process of protonated Q_B with free plastoquinones was retarded in the mutant, which may have caused the decrease of oxygen evolution. Furthermore, the mutant PSII was crystallized, and its crystal structure was analyzed at 2.1 Å resolution. The results showed that all of the four SQDG-binding have been occupied by other types of lipids, among which, the identities of three lipids were not determined whereas the remaining one was identified as a PG. Replacement of SQDG by other types of lipids was found to break most of the hydrogen-bonds formed by the original SQDG with the nearby amino acid residues, which may be the cause for the functional changes in the mutant PSII. These results indicate that SQDG plays essential roles in maintaining the integrity and function of PSII, and its binding sites have to be occupied, and the function of SQDG can be partially compensated for by other lipids, but its binding is necessary to fully maintain the integrity and activity of PSII.

REFFERENCES

1. Canfield, D. E. (2004) The early history of atmospheric oxygen: homage to Robert, M. Garrels. *Annu. Rev. Earth Planet Sci*., **33**, 1–36.
2. Bekker, A., Holland, H. D., Wang, P.-L., Rumble, I. D., Stein, H. J., Hannah, J. L., Coetzee, L. L., and Beukes, N. J. (2004) Dating the rise of atmospheric oxygen. *Nature*, **427**, 117–120.
3. Anbar, A. D., Duan, Y., Lyons, T. W., Arnold, G. L., Kendall, B., Creaser, R. A., Kaufman, A. J., Gordon, G. W., Scott, C., Garvin, J., and Buick, R. (2007) A whiff of oxygen before the great oxidation event? *Science*, **317**, 1903–1906.
4. V., Kranendonk, M. J. (2012) A chronostratigraphic division of the Precambrian. In *The Geologic Time Scale*, pp. 299–392, Elsevier.
5. Su, X., Ma, J., Wei, X., Cao, P., Zhu, D., Chang, W., Liu, Z., Zhang, X., and Li, M. (2017) Structure and assembly mechanism of plant $C_2S_2M_2$-type PSII-LHCII supercomplex. *Science*, **357**, 815–820.
6. Ozawa, S.-I., Bald, T., Onishi, T., Xue, H., Matsumura, T., Kubo, R., Takahashi, H., Hippler, M., and Takahashi, Y. (2018) Configuration of ten light-harvesting chlorophyll a/b complex I subunits in *Chlamydomonas reinhardtii* Photosystem I. *Plant Physiol*., **178**, 583–595.
7. Pan, X., Ma, J., Su, X., Cao, P., Chang, W., Liu, Z., Zhang, X., and Li, M. (2018) Structure of the maize photosystem I supercomplex with light-harvesting complexes I and II. *Science*, **360**, 1109–1113.
8. Blankenship, R. E. (2015) Structural and functional dynamics of photosynthetic antenna complexes. *Proc. Natl. Acad. Sci. U.S.A.*, **112**, 13751–13752.
9. Wolfe, G. R., Cunningham, F. X., Durnfordt, D., Green, B. R., and Gantt, E. (1994) Evidence for a common origin of chloroplasts with light-harvesting complexes of different pigmentation. *Nature*, **367**, 566–568.
10. Durnford, D. G., Deane, J. A., Tan, S., McFadden, G. I., Gantt, E., and Green, B. R. (1999) A phylogenetic assessment of the eukaryotic light-harvesting antenna proteins, with implications for plastid evolution. *J. Mol. Evol.*, **48**, 59–68.
11. Trumpower, B. L. (1990) The protonmotive Q cycle. Energy transduction by coupling of proton translocation to electron transfer by the cytochrome bc_1 complex. *J. Biol. Chem*., **265**, 11409–11412.
12. Adachi, K., Oiwa, K., Nishizaka, T., Furuike, S., Noji, H., Itoh, H., Yoshida, M., and Kinosita, K. (2007) Coupling of rotation and catalysis in F_1-ATPase revealed by single-molecule imaging and manipulation. *Cell*, **130**, 309–321.
13. Govindjee, Shevela, D., and Björn, L. O. (2017) Evolution of the Z-scheme of photosynthesis: a perspective. *Photosynth. Res*., **133**, 5–15.
14. Zouni, A., Witt, H. T., Kern, J., Fromme, P., Krauss, N., Saenger, W., and Orth, P. (2001) Crystal structure of photosystem II from *Synechococcus elongatus* at 3.8 Å resolution. *Nature,* **409,** 739-743.
15. Kamiya, N., and Shen, J.-R. (2003) Crystal structure of oxygen-evolving photosystem II from *Thermosynechococcus vulcanus* at 3.7-Å resolution. *Proc. Natl. Acad. Sci. U.S.A.*, **100**, 98–103.

16. Loll, B., Kern, J., Saenger, W., Zouni, A., and Biesiadka. J. (2005) Towards complete cofactor arrangement in the 3.0 Å resolution structure of photosystem II. *Nature*, **438**, 1040-1044.
17. Guskov, A., Kern, J., Gabdulkhakov, A., Broser, M., Zouni, A., and Saenger, W. (2009) Cyanobacteral photosystem II at 2.9-Å resolution and the role of quinones, lipids, channels and chloride. *Nat. Struc. Mol. Biol.*, **16**, 334–42.
18. Umena, Y., Kawakami, K., Shen, J.-R., and Kamiya, N. (2011) Crystal structure of oxygen-evolving photosystem II at a resolution of 1.9 Å. *Nature*, **473**, 55–60.
19. Ferreira, K. N., Iverson, T. M., Maghlaoui, K., Barber, J., and Iwata, S. (2004) Architecture of the photosynthetic oxygen-evolving center. *Science*, **303**, 1831–1838.
20. Koua, F. H. M., Umena, Y., Kawakami, K., and Shen, J.-R. (2013) Structure of Sr-substituted photosystem II at 2.1 Å resolution and its implications in the mechanism of water oxidation. *Proc. Natl. Acad. Sci. U.S.A.*, **110**, 3889–3894.
21. Shinopoulos, K. E., and Brudvig, G. W. (2012) Cytochrome b559 and cyclic electron transfer within photosystem II. *Bioch. Biophys. Acta*, 1817, 66–75.
22. Bentley, F. K., Luo, H., Dilbeck, P., Burnap, R. L., and Eaton-Rye, J. J. (2008) Effects of inactivating psbM and psbT on photodamage and assembly of photosystem II in *Synechocystis* sp. PCC 6803. *Biochemistry*, **47**, 11637–11646.
23. Suorsa, M., Regel, R. E., Paakkarinen, V., Battchikova, N., Herrmann, R. G., and Aro, E.-M. (2004) Protein assembly of photosystem II and accumulation of subcomplexes in the absence of low molecular mass subunits PsbL and PsbJ. *Eur. J. Biochem.*, **271**, 96−107.
24. Suga, M., Akita, F., Hirata, K., Ueno, G., Murakami, H., Nakajima, Y., Shimizu, T., Yamashita, K., Yamamoto, M., Ago, H., and Shen, J.-R. (2015) Native structure of photosystem II at 1.95 Å resolution viewed by femtosecond X-ray pulses. *Nature*, **517**, 99−103.
25. Glöckner, C., Kern, J., Broser, M., Zouni, A., Yachandra, V., and Yano, J. (2013) Structural changes of the oxygen-evolving complex in Photosystem II during the catalytic cycle. *J. Biol. Chem.,* **288**, 22607–22620.
26. Dau, H., Grundmeier, A., Loja P., and Haumann M. (2008) On the structure of the manganese complex of photosystem II: extended-range EXAFS data and specific atomic-resolution models for four S-states. *Philos. Trans. R. Soc. B Biol. Sci*., **363**, 1237–1244.
27. Luber, S., Rivalta, I., Umena, Y., Kawakami, K., Shen, J.-R., Kamiya, N., Brudvig, G. W., and Batista, V. S. (2011) S_1-state model of the O_2-evolving complex of Photosystem II. *Biochemistry*, **50**, 6308–6311.
28. Shoji, M., Isobe, H., Yamanaka, S., Umena, Y., Kawakami, K., Kamiya, N., Shen, J.-R., Nakajima, T., and Yamaguchi, K. (2015) Theoretical modelling of biomolecular systems I. Large-scale QM/MM calculations of hydrogen-bonding networks of the oxygen evolving complex of photosystem II. *Mol. Phys.*, **113**, 359–384.

29. Kok, B., Forbush, B., and McGloin, M. Cooperation of Charges in photosynthetic O_2 evolution–I. a Linear four step mechanism. *Photochem. Photobiol.*, 11, 457–475.
30. Shen, J.-R. (2015) Structure of photosystem II and the mechanism of water oxidation in photosynthesis. *Annu. Rev. Plant Biol.*, 66, 23-48.
31. Nagao, R., Ueoka-Nakanishi, H., and Noguchi, T. (2017) D1-Asn-298 in photosystem II is involved in a hydrogen-bond network near the redox-active tyrosine Y_Z for proton exit during water oxidation. *J. Biol. Chem.*, 292, 20046–20057.

Chapter 1

Optimization of micro-crystallization for crystal structure analysis of intermediate state of PSII

ABSTRACT

The mechanism of O=O bond formation in photosystem II (PSII) remains obscure owing to the lack of intermediate-state structures of PSII. To clarify the formation mechanism of molecular oxygen, structural analysis of intermediate S-states is necessary. For this purpose, time-resolved serial femtosecond crystallography (TR-SFX) with femtosecond free electron X-ray laser pulses (XFEL) is indispensable. For the TR-SFX experiments, a huge amount of PSII micro-crystals must be used, since during the SFX experiments, the PSII crystals must be exchanged continuously to ensure that each crystal receives only one pulse of XFEL irradiation, and also since large PSII crystals do not allow penetration of exciting light to advance the S-state to intermediate ones. In this study, we established a simple micro-crystallization method to obtain micro-crystals of PSII dimers. The size, crystallization conditions and cryo-protectant treatment conditions were screened and optimized to ensure a high resolution of the micro-crystals. As a result, around 100 μm-sized crystals were obtained in a large quantity, and cryo-protectant treatment by incubation in a solution containing high concentrations of polyethylene glycol (PEG) 1450 and glycerol was found to be important to give a high resolution from the PSII micro-crystals. The micro-crystals obtained finally gave a highest diffraction spot 2.1 Å resolution. Using these micro-crystals, diffraction datasets with 2.35 Å resolution from the dark- and 2 flash-illuminated samples were obtained, which lead to structure analyses of the S_1 and S_3-states. Fourier difference maps between these two S-states showed insertion of a new oxygen atom (O6) close to O5, thus giving rise to important clues to the site and mechanism of O=O bond formation in PSII.

INTRODUCTION

The structure of PSII has been analyzed at high-resolutions structures (1, 2); however, these structures represent the dark-stable S_1-state structure. Since the water-splitting reaction catalyzed by the oxygen-evolving center (OEC) of PSII proceeds with the S-state cycle (3), analyses of the intermediate S-state structures are indispensable for elucidation of the mechanism of O=O bond formation and O_2 evolution. Recently, a technique called serial femtosecond X-ray crystallography (SFX) using femtosecond XFEL pulses have been developed, which utilizes ultra-brilliant, femtosecond X-ray pulses to irradiate micro-crystals to obtain diffraction images. Due to the ultra-high intensity of the XFEL pulses, each crystal will be destroyed by irradiation with one single XFEL pulse. Thus, a huge number of crystals must be used to obtain a full diffraction data set available for structural analysis. Owing to the ultra-short XFEL pulses, this approach allows time-resolved serial femtosecond crystallography (TR-SFX) to determine various intermediate states of enzyme reactions, providing an important tool to reveal the catalytic processes of enzymes occurring in a short period of time (4–6). This approach also enables determination of the intermediate S-state structures of PSII which is induced by light illumination and proceed within the time range of several tens of μs to ms. In this case, visible flash light illuminations are used to advance the S-state to certain intermediate S-state, and the XFEL pulses are used to irradiate the micro-crystals after certain delay time to obtain the X-ray diffraction data from the intermediate S-state. This approach is called pump-probe experiment.

In the conventional method, high resolution structural analysis of PSII with synchrotron X-rays, PSII dimer crystals with a size of 1.0-1.2 mm were used (1). However, with the TR-SFX method to determine the intermediate S-state structures, the large PSII crystals cannot be used, and small crystals with sizes below 100 μm must be used. This is due to two reasons. First, the larger PSII crystals do not allow light to penetrate into its interior due to the high density of Chls within the PSII complex, hence it is difficult to advance the S-state to an intermediate state. Second, as described above, the SFX method employs a huge number of small crystals, as each crystal can be irradiated by only one single XFEL pulses. Thus, micro-crystals of PSII are necessary for the TR-SFX experiments to obtain the intermediate S-state structures, and this approach has been used by other groups (5, 7). However, the resolutions of the PSII micro-crystals obtained by these groups are not high enough to obtain meaningful information regarding the mechanism of O=O bond formation and water oxidation (5, 7).

To analyze the intermediate S-state structures of PSII at a higher resolution, we established the method of micro-crystallization for PSII dimers, and screened, optimized the crystallization and cryo-protection conditions. This yielded PSII micro-crystals with sizes up to 100 μm for the longest side in a large amount, and with a highest resolution of 2.1 Å for the diffraction spot at the most outside. Using the micro-crystals of PSII thus produced, the S_3-state structure of PSII induced by 2 flashes illumination was obtained, which provided important information regarding the site of O=O bond formation and mechanism of water-splitting.

MATERIALS AND METHODS

Cell culture and purification

Liquid culture of *T. vulcanus* cells was grown at 50°C with bubbling of air containing 3% (v/v) CO_2 under constant red LED light at an intensity of 20 μmol photons m^{-2} s^{-1} in a plant growth chamber (BIOTRON LH-410PF-SP). For purification of the PSII dimer sample, 60 L of cells were grown for 7 days and the light intensity was increased gradually from 20 to 100 μmol photons m^{-2} s^{-1}. The amount of culture cells for one-time of the SFX experiment is 12-15 times of this amount, namely from around 720 L to 900 L. The cultured cells were harvested by centrifugation at 13.800 g for 15 min (R9A rotor, HITACHI KOKI) and the precipitated cells were washed by a buffer of 40 mM KH_2O_4-KOH (pH 6.8). After centrifugation at 13.800 g for 15 min, the precipitated cells were suspended by a buffer of 0.4 M Mannitol, 40 mM KH_2O_4-KOH (pH 6.8) and incubated for 90 min after addition of 1 mM EDTA-2Na and 0.14% (w/v) lysozyme at final concentration. The incubated cells were centrifuged at 13.800 g for 15 min, and the precipitated cells were suspended by a buffer of 25% glycerol, 20mM Hepes-NaOH (pH 7.0), 10 mM $MgCl_2$ (Buffer-D), and stored at -80°C.

After throwing, cells were diluted about ten times of its volume with a buffer containing 30 mM Hepes-NaOH (pH 7.0), 10 mM $MgCl_2$ (Buffer-C) to give the sample solution an osmotic shock to disrupt the cells. The precipitant after centrifugation at 13,800 g for 15min at 4°C (R9A rotor, HITACHI KOKI) was resuspended by Buffer-D, and treated with 1% (w/v) DNase for 20 min. The solution after the treatment was collected by centrifugation, giving rise to the thylakoid membranes. The thylakoid membrane obtained by the above treatment was solubilized by N, N-dimethyldodecylamine N-oxide (LDAO) twice. At the 1st treatment, after centrifugation of disrupted cells at 13,800 g for 15 min, the

precipitant was suspended by a buffer containing 5% glycerol (w/v), 30 mM Hepes-NaOH (pH 7.0), 10mM $MgCl_2$, to which a final concentration of 0.16% (w/w) LDAO was added from a stock solution of LDAO. After incubation at 5 min, the sample solution was centrifuged at 39,000 g for 60 min, 4 ^oC (R21A rotor, HITACHI KOKI), and the precipitant was suspended with Buffer-D. This solution was used for the 2nd LDAO treatment by adding a final concentration of 0.28% (v/v) LDAO. After mixing by stirrer and incubation on ice for 5 min, insolubilized materials were precipitated by centrifugation at 93,000 g for 60 min (P70A rotor, HITACHI KOKI). The supernatant was recovered, to which a final concentration of 13% (w/v) polyethylene glycol (PEG) 1500 was added, which was then centrifuged at 93,000 g for 30 min. The precipitant obtained was suspended with Buffer-D to a concentration of 1 mg Chl ml^{-1}, which is designated crude PSII sample (LDAO-PSII). To purify the PSII dimer from the crude PSII, anion exchange chromatography was performed using Q-sepharose High performance (GE Health) with a bed volume of 200 ml. The crude PSII was solubilized with 1% (w/v) n-dodecyl-β-d-maltoside (β-DDM) and incubated on ice for 30 min with gentle stirring. The insolubilized materials were removed by centrifugation at 93,000 g for 10 min, and the supernatant was collected, filtered with a 0.45 μm disc filter, and then loaded onto the ion-exchange column. The column was washed with 170 mM NaCl in a solution containing 5% (w/v) glycerol, 30 mM Mes-NaOH (pH 6.0). 3 mM $CaCl_2$ and 0.03% (w/v) β-DDM at 6-10 times of the bed volume, and the concentration of NaCl was increased gradually from 170 to 300 mM with a linear gradient in 10 times of the bed volume for separating the PSII and other fractions. The PSII monomer and dimer fractions were eluted at 200-220 mM and 230-250 mM NaCl, respectively. The eluted solution was collected in glass tubes with a volume of 25 ml for each tube. The PSII dimer fraction obtained was diluted three times by a buffer containing 5% (w/v) glycerol, 30 mM Mes-NaOH (pH 6.0), 3 mM $CaCl_2$, 20 mM NaCl (storage buffer), and a final concentration of 13% (w/v) PEG1500 was added, then the solution was centrifuged at 93,000 g for 30 min. The precipitated PSII dimer was gently suspended by a small volume of the storage buffer to a high Chl concentration, and stored at -180^{o}C (liquid nitrogen) until further utilization. All procedures for the above preparation were performed under dim green light.

Oxygen evolution

Oxygen evolution was measured with a Clark-type oxygen electrode (Hansatech Instruments) under continuous, saturating illumination at 30°C in the storage buffer, with 0.3 mM phenyl-p-benzoquinone

and 1 mM potassium ferricyanide as electron acceptors at a chlorophyll (Chl) concentration of 10 μg Chl ml^{-1}.

Clear Native PAGE

Clear native electrophoresis (CN-PAGE) was performed by using constant 7.5% acrylamide gel, according to the method described previously (7, 8). The voltage and time interval used were the same as those used in the blue native CN-PAGE method (9). All samples were treated with buffer-D containing 1% (w/v) β-DDM, and the thylakoid membrane and crude PSII sample after LDAO treatment were incubated for 20 and 30 min, respectively, followed by centrifugation at 22,000 g for 20 min for both samples to remove insolubilized materials. The incubation time was for 10 min for the PSII dimer sample, and centrifugation was performed. The amounts applied to each lane were 15 μg Chl for the thylakoid membrane, 7 μg Chl for the crude PSII sample and 5 μg Chl for the PSII monomer and dimer, respectively.

Micro-crystallization

Initially, the following two micro-crystallization methods were used:

1) **Pipetting method:** The PSII dimer sample at a concentration of 4.0 mg Chl ml^{-1} was added to a 0.6-ml micro-centrifuge tube (Watson), and then, the same volume of a buffer (precipitant buffer) containing 40 mM Mes-NaOH (pH 6.0), 80 mM $MgSO_4$, 40 mM NaCl, 20 mM $CaCl_2$, 10.0-10.5 % (w/v) PEG1450, 1.7% (w/v) n-heptyl 1-thio-β-D-glucopyranoside (HTG) (Dojindo) was added. (The concentration of PSII dimer and solutions in precipitant buffer became half in the crystallization solution.) The solution was gently mixed immediately with a pipettman for 30 sec on ice. The crystallization solution was incubated at 20°C for 10-15 min. After incubation, the crystallization tubes were examined by a stereoscopic microscope (SZX16, OLYNPUS) under dim green light to see if there are micro-crystals in the tube. If there are no crystals, the crystallization solution was mixed and incubated for 10 min again, and then examined again. If seed-crystals were already produced in the tube, the tube was continuously incubated at 20°C without stirring to allow growth of the micro-crystals. After incubation for 2-3 hour, the size of micro-crystals reaches to around 30-50 μm, and the crystal size was not likely to grow any more.
2) **Seeding method:** First of all, 300-500 μm sized crystals were produced in a 0.6-ml tube in a day

at 4°C. The conditions and method used are almost the same as those used with the pipetting method, but without further mixing after the first mixing. The large crystals obtained were precipitated by centrifuge at 2,400 g for 1 min, and washed by the buffer containing 10% PEG 1450 (w/v) without HTG after removing the supernatant. The washing step was repeated several times, and then the same buffer was added to the tube, and the crystals were gently and elaborately crashed by a homogenizer pestle (AsOne) on ice. This seed solution was added to a crystallization buffer containing slightly lower concentration of PEG than that used for the growth of the seed crystals. The seed solution was added to newly prepared crystallization solutions in ratios (volume/volume) of 1/10, 1/100, 1/500, 1/1000, among which, the condition that gave the optimal size of micro-crystals was selected.

In order to obtain the best size and yield of the PSII micro-crystals, the method for the micro-crystallization was improved as described below:

3) **Tube vortex method**: An amount of 25 µl PSII dimers with a concentration of 4.5 mg Chl ml^{-1} was added to a tube (Watson, 1.5 ml sampling tube), and the same amount of the precipitant buffer containing 40 mM Mes-NaOH (pH 6.0), 80 mM $MgSO_4$, 40 mM NaCl, 20 mM $CaCl_2$, 11.5-12.0 % (w/v) PEG1450, 1.7% HTG was added. This crystallization solution was gently mixed immediately with a small vortex (1-9412-01 AsOne) and incubated at 20°C.

After incubation for 3-5 hour, if the size of the micro-crystals reaches to around 100 µm, crystal growth was stopped by addition of 50 µl of the crystallization buffer in which the concentration of PEG1450 was increased by 1–2% from the crystallization condition (incubation buffer). Micro-crystals grew on inner-surface of the tube were gently detached by gentle stirring with a mixer (TWIN3-28N, SANSYO), and the micro-crystals of 6-8 tubes were harvested into one tube. The micro-crystals were washed for several times with the incubation buffer to remove the PSII protein that were not crystallized as well as too small crystals, and stored in the buffer at 20°C for 1-2 days before SFX experiment or freezing for the fixed-target XFEL experiment.

The total amount of the purified PSII dimers used for one SFX experiment is 100-120 mg Chl.

Procedure of cryoprotectant treatment

Initially, cryoprotectant treatment was performed with a stepwise method in a similar way as that used for large crystals with slight modifications. In the first step, the incubation buffer was removed and

30-40 µl of the cryoprotectant buffer containing 7-8% (w/v) PEG1450, 20 mM Mes-NaOH (pH 6.0), 20 mM NaCl, 10 mM $CaCl_2$ and 0.85% HTG (1 step buffer) was added to micro-crystal tube. Then, 50 µl of the cryoprotectant buffer containing slightly higher concertation of PEG and glycerol was added, and incubated for 10 min. This step was repeated 10 times, until the cryoprotectant PEG and glycerol reach to the highest concentration required. At the final step (step 10), all of the supernatant was removed and 50 µl of the final cryoprotectant buffer was added again and incubated for 15 min.

Screening of grease conditions for SFX

Grease is used as a matrix for the delivery of the micro-crystals in the SFX experiments. To examine the possible effects of greases on the PSII micro-crystals, their shapes were observed with a stereoscopic microscope (SZX16, OLYNPUS) after mixing with three types of greases; an AZ grease (#761, AZ Co.), a synthesize grease (Super Lube, #21030, Synco Chemical Co.) and a nuclear grade grease (Super Lube, #42150, Synco Chemical Co). The crystal images were taken by an infrared camera (ARTCAM-130MI-NIR-WOM, ARTRAY).

Optimization of the conditions for cryoprotection

The conditions of cryoprotection were screened with an in-house X-ray machine to find the best condition that give rise to highest resolution. For the measurements of diffraction at room temperature, the MicroRT™ Room Temperature Starter Kit (Mitogen) was utilized to mount the crystals.

Examination of resolutions of the crystals treated by several different conditions at SPring-8

To check the resolutions of the PSII micro-crystal treated by different cryoprotectant buffers, the micro-crystals were mounted on a nylon loop with a pipettman and then flash-frozen in a nitrogen gas stream at 100 K after cryoprotection. The “multiple centering mode” of the BSS software in the beamlines of SPring-8 was used to achieve multiple diffraction images. This program enables automatic irradiation of the X-ray to the locations pre-registered to obtain diffraction images from multiple micro-crystals automatically and continuously.

RESULTS

Purity and activity of the PSII dimers

Before micro-crystallization, the purity and activity of different batches of the PSII dimers were assessed by Clear Native PAGE and O_2 evolving activity measurement. Some examples of these analyses are shown in Fig. 1-1. The samples suitable for the SFX experiments were selected with the criteria that the contamination of PSI trimer is as little as possible and the O_2 evolving activity reaches 2000-2500 μmol O_2 mg Chl^{-1} h^{-1}.

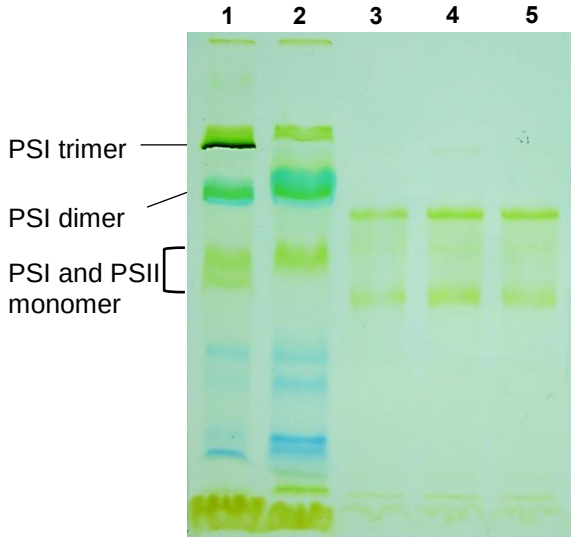

Purification lot No.	oxygen-evolving activity (μmol O_2・mg Chl^{-1}・h^{-1})
Lot. 1	2140 ± 110
Lot. 2	2240 ± 130
Lot. 3	2080 ± 140

Each values are averages of 5 independent samples.

Fig. 1-1. Clear Native PAGE (left) and O_2 evolving activity (right) of PSII dimer used for SFX experiment. Left: Lane 1, Thylakoid membrane; Lane 2, Crude PSII core after LDAO treatment; Lane 3, 4 and 5, Different batches of the purified PSII dimers.

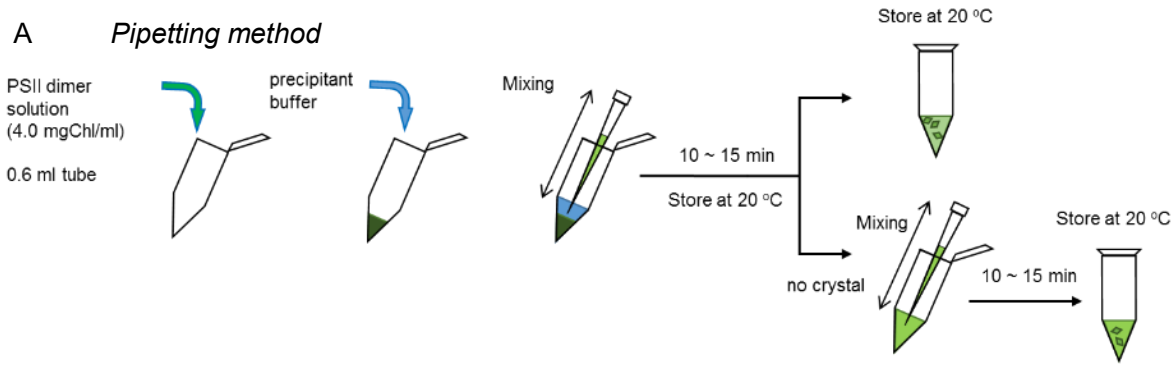

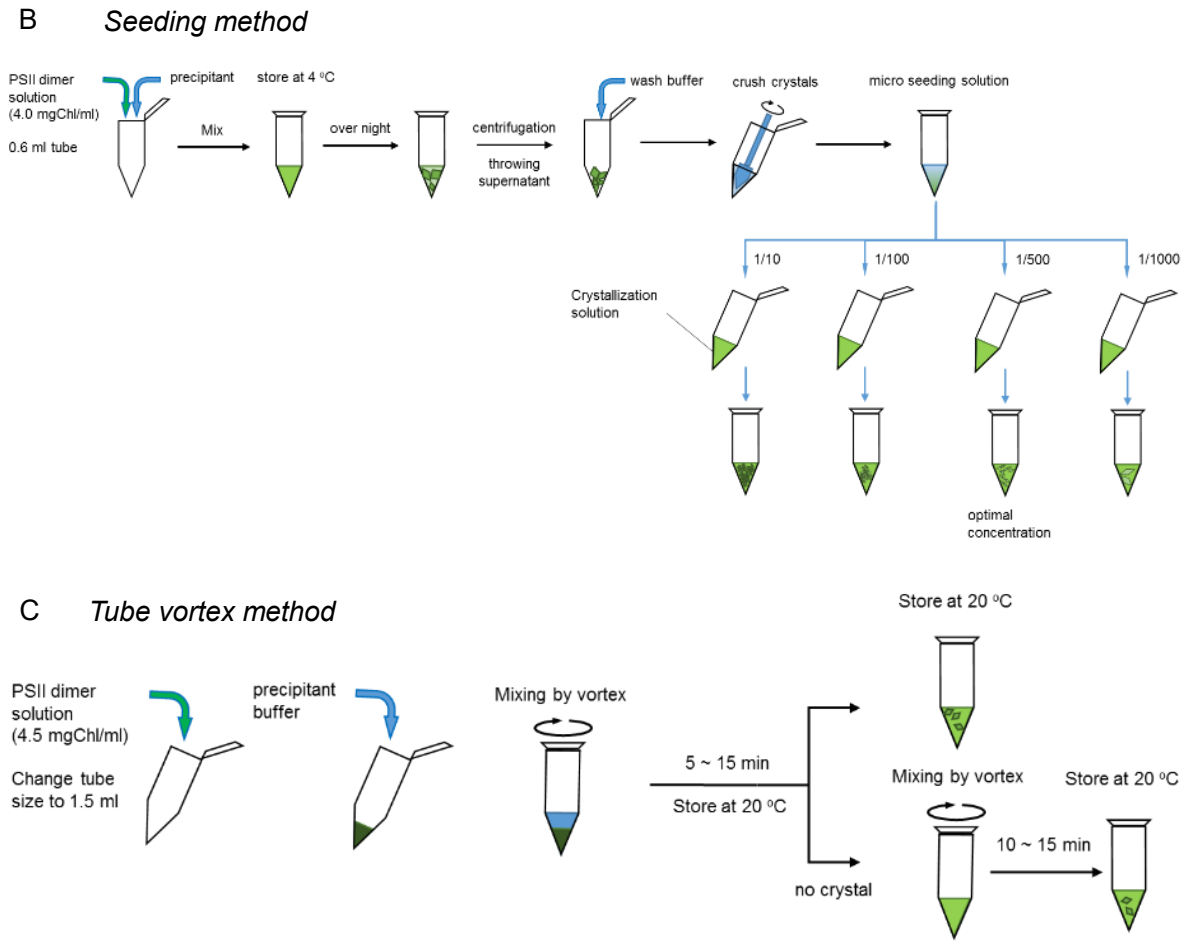

Fig. 1-2. Methods for the micro-crystallization of PSII dimers.

Optimization of the method for micro-crystallization and screening of the optimal kinds of greases

In order to ensure effective excitation by the pump lasers, PSII micro-crystals with a size of 20-30 μm were initially prepared. Crystallization by the "pipetting method" (Fig. 1-2A) yielded 10-20 μm sized micro-crystals, most of which had a round shape and were present in a form of multi-clusters (Fig. 1-3A, B). In this method, the micro-crystals appeared rapidly as soon as the crystallization solutions were mixed within the tubes, and the resulted micro-crystals soon precipitated in the bottom of the tubes. In contrast, micro-crystals obtained by the "seeding method" (Fig. 1-2B) showed sharp edges but thin, and regular size of 30 μm (Fig. 1-3D). In this method, the micro-crystals grow slowly so that many of them attach to the surface of the inner wall of the tube (Fig. 1-3C).

For the delivery of the micro-crystals in the SFX experiments, we used a grease matrix (10) to mix with the PSII micro-crystals. In order to find the best grease that gives little effects on the crystal quality and resolution, the PSII micro-crystals were mixed with three kinds of greases, and their shapes were examined under an optical microscope with an infrared camera. As a result, the AZ grease and synthesize grease affected the PSII micro-crystals remarkably; the PSII micro-crystals are aggregated and their shapes became round upon mixing with these greases (Fig.1-4B, C). This suggests that some of the micro-crystal may have been dissolved and/or broken by these greases. In contrast, the nuclear grade grease showed few changes in the shapes and behaviors of the micro-crystals (Fig. 1-4D). Therefore, the nuclear grade grease suitable for the SFX experiments was selected.

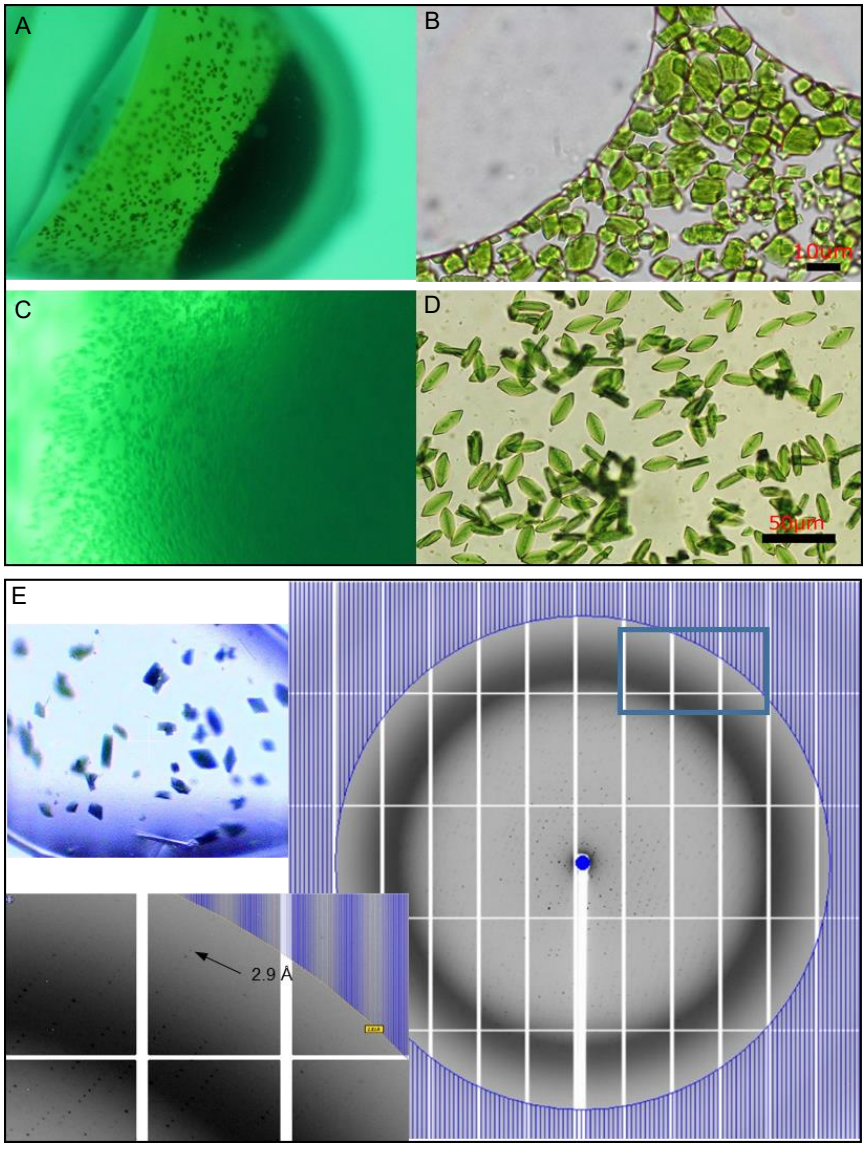

Fig. 1-3. PSII micro-crystals grown with the "pipetting method" (A, B) and the "seeding method" (C, D), and one of the diffraction images (E) obtained from the micro-crystals at BL41XU of SPring-8. Panel C shows the crystals growing on the surface of the inner wall of a tube by the "seeding method". E indicates frozen micro-crystals mounted on a loop and a diffraction image with the best resolution from a micro-crystal made by the "pipetting method" with BL41XU of SPring-8. The lower left-side image is an enlarged view of a square region in the right image of E. Arrow indicates the maximum diffraction spot.

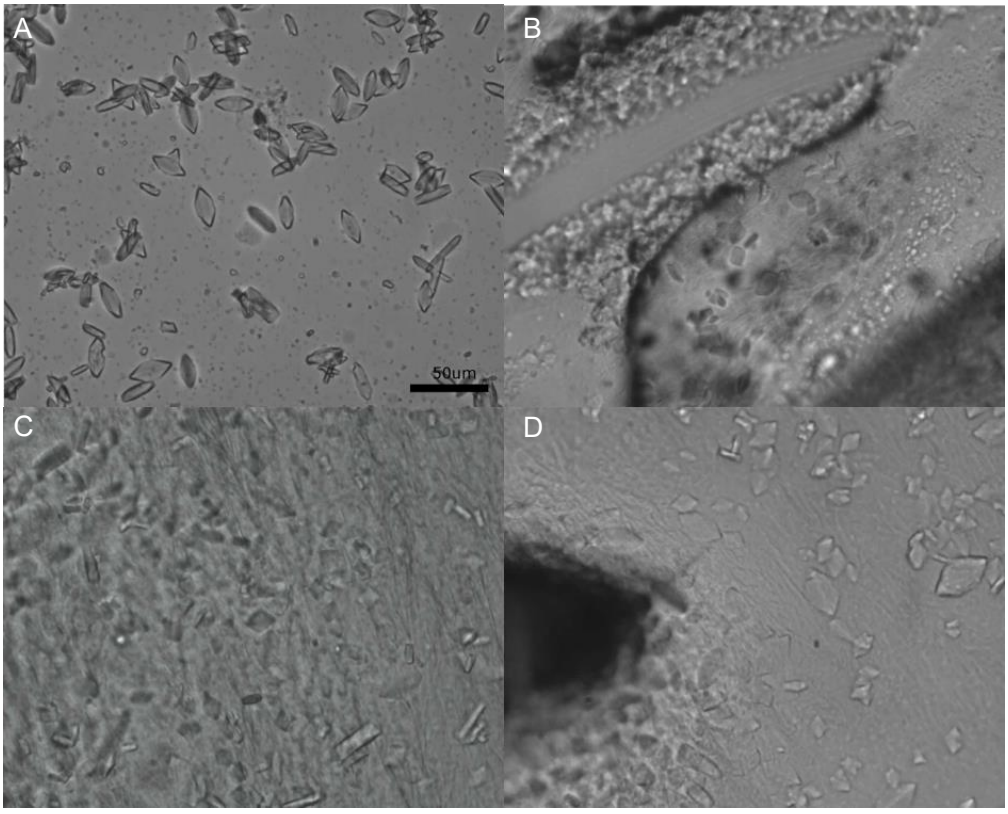

Fig. 1-4. PSII micro-crystals mixed with three kinds of greases. A, PSII micro-crystals without mixing with any greases; B, C and D, PSII micro-crystals mixed with a synthesize grease, an AZ grease and a nuclear grade grease, respectively.

The PSII micro-crystals made with the above two methods were treated by a cryoprotectant buffer containing 10% (w/v) PEG 1450, 10% (w/v) PEG 5000MME and 25% (w/v) glycerol, and frozen for examination of their resolution at SPring-8. The results showed that the micro-crystals made by the

pipetting method showed better resolutions than those produced by the seeding method in spite of their bad shapes. The maximum resolutions obtained were around 2.8 Å (Fig. 1-4E). The micro-crystals made by the pipettman method were also examined by the XFEL pulse laser at SACLA. A typical diffraction image obtained was shown in Fig. 1-5. It was found that the highest resolution obtained by the XFELs of SACLA was lower than that obtained with BL41XU of SPring-8, which is most likely due to the lower X-ray intensity of each XFEL pulse compared with the X-ray in BL41XU. Furthermore, the number of diffraction images with good resolution was extremely small with the XFEL pulses, which was far enough for the structural analysis by the SFX method.

One of the reasons responsible for this problem was considered to be the too small sizes of the micro-crystals used. Hence, the sizes of the majority of the micro-crystals were changed to 30-50 μm by adjustment of the PEG concentration and incubation time used for crystallization, the resulted crystals were examined for their diffraction resolutions by XFELs again. As a result, the maximum resolutions of the diffraction images were not much changed; however, the number of diffraction images with higher resolutions was slightly increased.

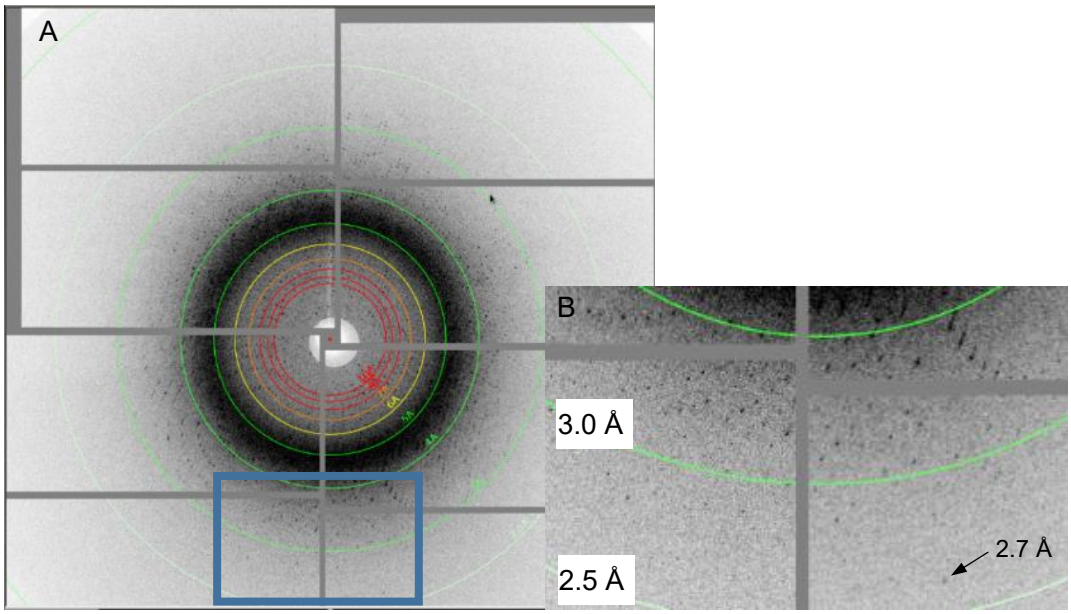

Fig. 1-5. A diffraction image obtained with an XFEL pulse from a PSII micro-crystal produced by the "pipetting method" (such as Fig. 1-2B). B is an enlarged view of the squared region in A. Arrow indicates the maximum diffraction spots.

To obtain diffraction images with higher resolutions, the method of crystallization was changed to the "tube vortex method" (Fig. 1-2C) with which, the crystal sizes were increased to 50-100 μm (Fig. 1-6). In this method, the tube utilized for crystallization was changed to a 1.5-ml centrifuge tube, which increased the probability of crystallization and therefore increased the number of PSII micro-crystals in each tube that can be harvested. In addition, the final Chl concentration used for crystallization was increased from 2.0 mg Chl ml^{-1} to 2.25 mg Chl ml^{-1}, and the mixing method was changed to a gentle mixing using a vortex. These changes appeared to increase the number of PSII micro-crystals significantly. Furthermore, the size of the crystals was controlled by controlling the length of the incubation time, PEG concentration, mixing time with the vortex and the temperature during the mixing process. By these modifications, a large number of 50-100 μm sized crystals were obtained reproducibly (Fig. 1-6A). These micro-crystals diffracted to a resolution of around 2.5-2.6 Å in some cases (Fig. 1-6B, C) by XFEL pulses.

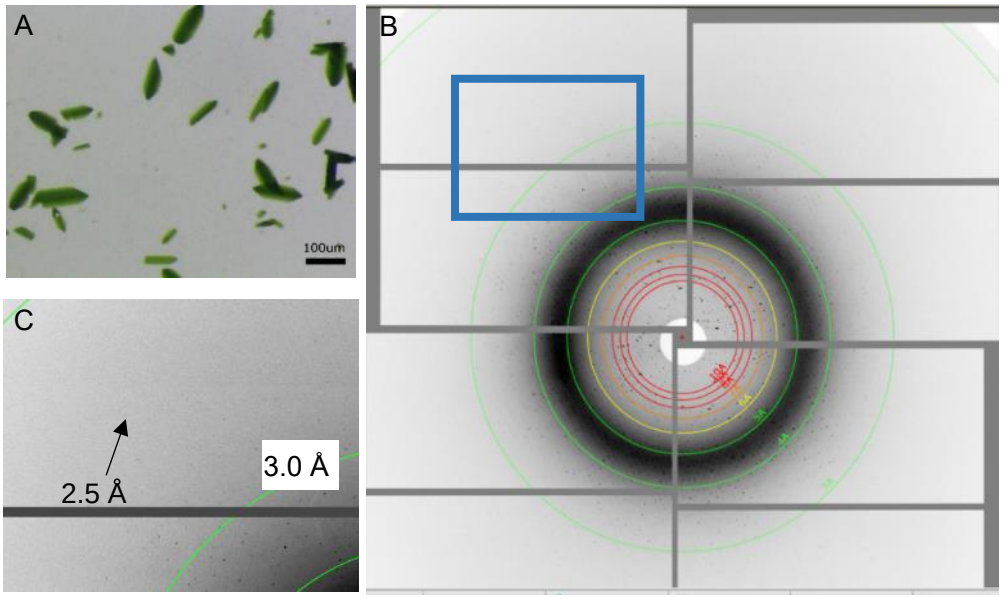

Fig. 1-6. An image of around 100 μm sized micro-crystals (A) and a typical diffraction image from one of these crystals by using one pulse of the XFEL (B). C is an enlarged view of the square region in panel B. Arrow indicates the maximum diffraction spot.

Optimization of the conditions for the treatment of cryoprotectants

To analyze reliable structure of the intermediate S-states, especially structural changes of the Mn_4CaO_5-cluster induced by single turn-over flash excitations, diffraction image datasets at around 2.3 Å or higher resolutions with the XFEL pulses are required. The PSII micro-crystals obtained by the method described above were not enough to achieve the high-resolution datasets, and it was found that a post-crystallization treatment with a suitable composition and concentration of the cryoprotectants were necessary to further improve the resolution. Accordingly, the conditions of cryoprotection were screened by an in-house X-ray machine to examine the resolutions of the micro-crystals treated with various conditions of the cryoprotectants. In order to detect diffraction spots using the weak X-rays provided by the in-house X-ray machine, the size of crystals were increased to around 200 μm by the tube vortex method (Fig. 1-7D), and they were irradiated by the X-rays for 5-10 min (the irradiation was normally performed for 1 min for larger PSII crystals) at room temperature. Diffraction images obtained upon increasing the concentration of the cryoprotectant buffer in the micro-crystal solutions in 10 steps were used as a control. The results showed that upon treatment of the cryoprotectant solutions for 7 steps, the resolution of the diffraction images were improved dramatically, and diffraction spots with maximum resolutions at around 3.6-3.7 Å were obtained (Fig. 1-7C). This indicates that treatment with the cryoprotectant buffer at concentrations at least above 14% PEG and glycerol is necessary to collect the diffraction datasets with reasonably good resolutions (bottom table in Fig. 1-7). The unit cell parameters from these crystals treated under this condition were calculated to be a= 129 Å, b= 231 Å and c= 289 Å. Thus, all of axes were slightly longer compared with the normal crystal treated by a higher concentration of the cryoprotectant buffer (1, 2). Finally, a condition was chosen where the concentrations of PEG and Glycerol in the post-crystallization buffer were slightly lower than those in the normal treatment conditions, namely 9% (w/v) PEG1450 instead of 10%, 9% (w/v) PEG 5,000MME instead of 10%, and 22% (w/v) glycerol instead of 25%. This condition was found to give almost the same resolution as that treated with the normal condition, and may also prevent damages to the PSII micro-crystals that may be caused by the treatment with too high concentrations of PEG and glycerol for a long time during the SFX experiments. Furthermore, to ensure the higher efficiency of S-state transitions as well as for the improvement of the resolutions, final concentrations of 10 mM potassium ferricyanide and 2% DMSO were added to the cryoprotectant buffer. Resolutions of the micro-crystals after these treatments were examined in BL41XU again, and it was found that diffraction images with

higher resolutions upon treatment with the new cryoprotectant conditions could be obtained. The highest resolution spots observed were at around 2.05 Å at BL41XU of SPring-8 with the frozen micro-crystals (Fig. 1-8).

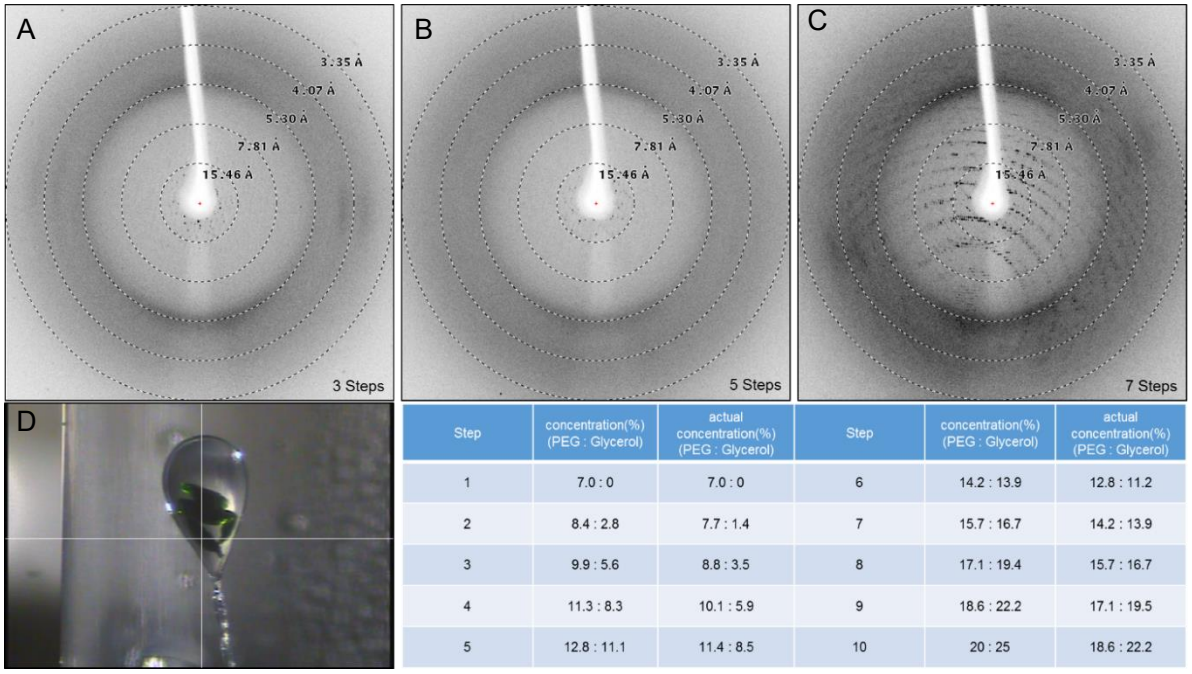

Step	concentration(%) (PEG : Glycerol)	actual concentration(%) (PEG : Glycerol)	Step	concentration(%) (PEG : Glycerol)	actual concentration(%) (PEG : Glycerol)
1	7.0 : 0	7.0 : 0	6	14.2 : 13.9	12.8 : 11.2
2	8.4 : 2.8	7.7 : 1.4	7	15.7 : 16.7	14.2 : 13.9
3	9.9 : 5.6	8.8 : 3.5	8	17.1 : 19.4	15.7 : 16.7
4	11.3 : 8.3	10.1 : 5.9	9	18.6 : 22.2	17.1 : 19.5
5	12.8 : 11.1	11.4 : 8.5	10	20 : 25	18.6 : 22.2

Fig. 1-7. Screening of the conditions for cryoprotection using the in-house X-ray machine at room temperature. A~C. Diffraction images obtained from crystals treated by cryoprotectant buffers for 3, 5 and 7 steps, respectively. Left-down side figure (D) indicates a typical middle sized crystal mounted on a cryo-loop utilized for the measurements. The cross lines in panel D indicate the approximate irradiation center of the X-rays. Table shows the concentrations of PEG and glycerol used in each step of the cryoprotectant buffer and actual concentrations in the tube after adding these solutions.

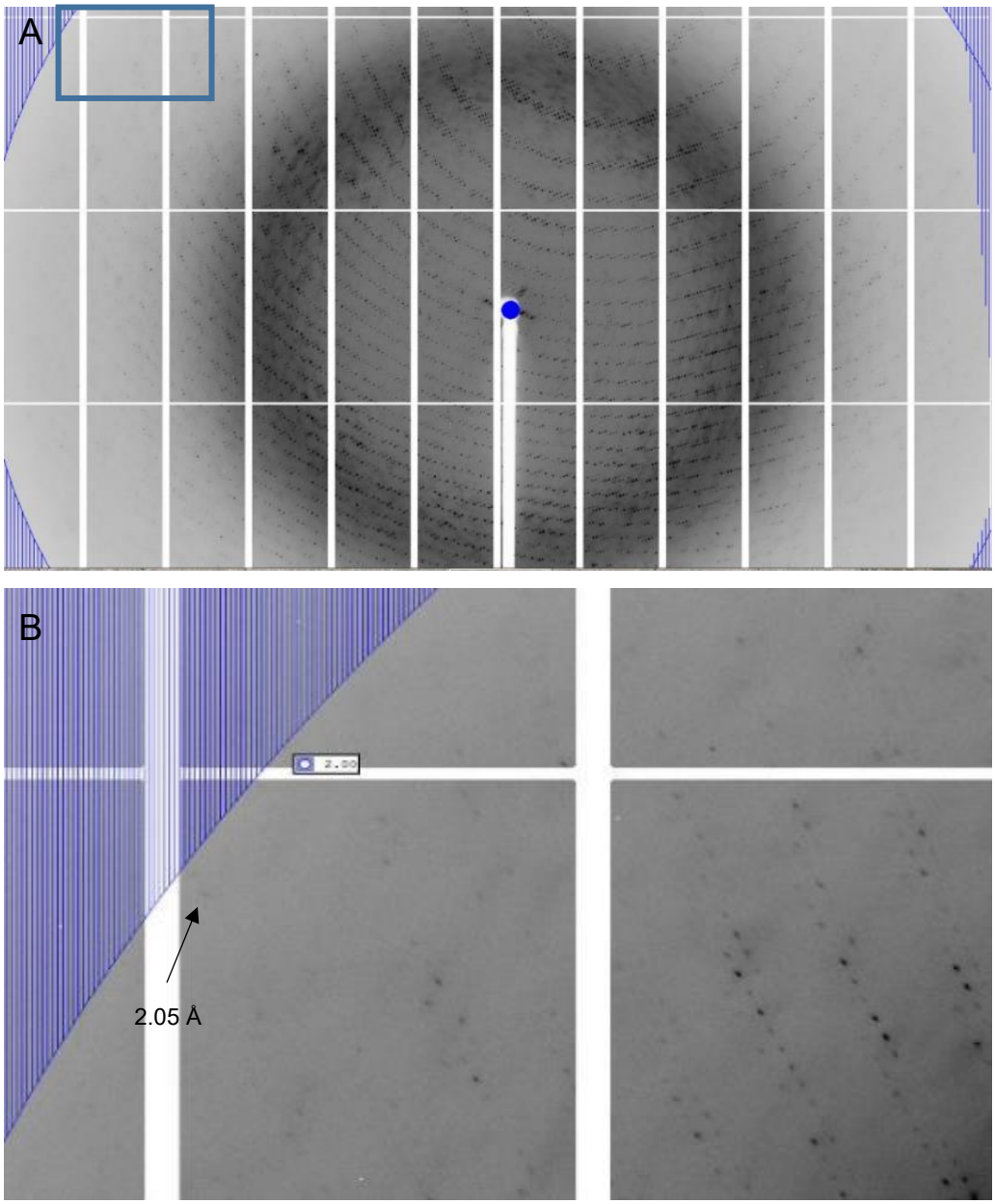

Fig. 1-8. An example of the diffraction images obtained from frozen 100 µm sized PSII micro-crystals at BL41XU of SPring-8. The micro-crystals were frozen after treatment by the cryoprotectant buffer containing 9% PEG 1450, 9% PEG 5000MME, 22% glycerol, 2% DMSO and 10 mM potassium ferricyanide. Panel B is an enlarged view of the squared region shown in panel A. Arrow indicate a diffraction spot at a maximum resolution.

The same PSII micro-crystals were used to collect the diffraction data at XFEL with the SFX method at room temperature. However, we could not obtain the diffraction images with similar quality and resolutions as those obtained with the Synchrotron X-rays. Several possibilities may be considered for this discrepancy. First, the X-ray intensity of each XFEL pulse provided by SACLA is slightly lower than that provided by BL41XU with an exposure time 0.1-1 sec. Actually, the photon numbers of each XFEL pulse of SACLA may be a magnitude lower than that of BL41XU in an exposure time of 0.5 sec. Second, the PSII micro-crystals may have suffered from damage upon mixing with the grease matrix, which is required to deliver the micro-crystals into the jet stream for the SFX experiments. Finally, since the SFX experiments with XFEL are performed at room temperature, whereas diffraction images at BL41XU were taken with the frozen crystals at 100 K, the resolutions of the micro-crystals may be better at frozen temperatures. We observed that some crystals gave rise to larger unit cell dimensions of a = 129.7Å, b = 230.69 Å and c = 306.7 Å often with the XFEL pulses at room temperature (Fig. 1-9B), and the diffraction images having these longer unit cell parameters showed a lower resolution at around 3.0 Å. This may have been caused by insufficient shrinking due to a low concentration of the cryoprotectants used or introduction of some water content from the grease used to mix with the crystals. Consequently, we found that a longer time of treatment (around 1~2 days) by the post-crystallization solution (containing 7-8% (w/v) PEG 1450) utilized as the storage buffer for the micro-crystals was important for effectively shrinking the crystals, yielding good diffracting PSII crystals (Fig. 1-9A). This shortening of the unit cell lengths largely improved the resolution of diffraction datasets obtained from the PSII micro-crystals.

With the use of a combination of the above procedures and conditions for crystal growth and post-crystallization treatment, we were able to obtain diffraction images at 2.1-2.2 Å resolutions from the PSII micro-crystals (Fig. 1-10C) using XFELs of SACLA with the pump-probe SFX experiments at room temperature, and we succeeded in collecting the diffraction datasets that were analyzed at 2.35 Å resolutions for the dark-stable S_1-state and 2 flash-induced S_3-state from the PSII micro-crystals, allowing us to see structural changes during the transition from S_1 to S_3.

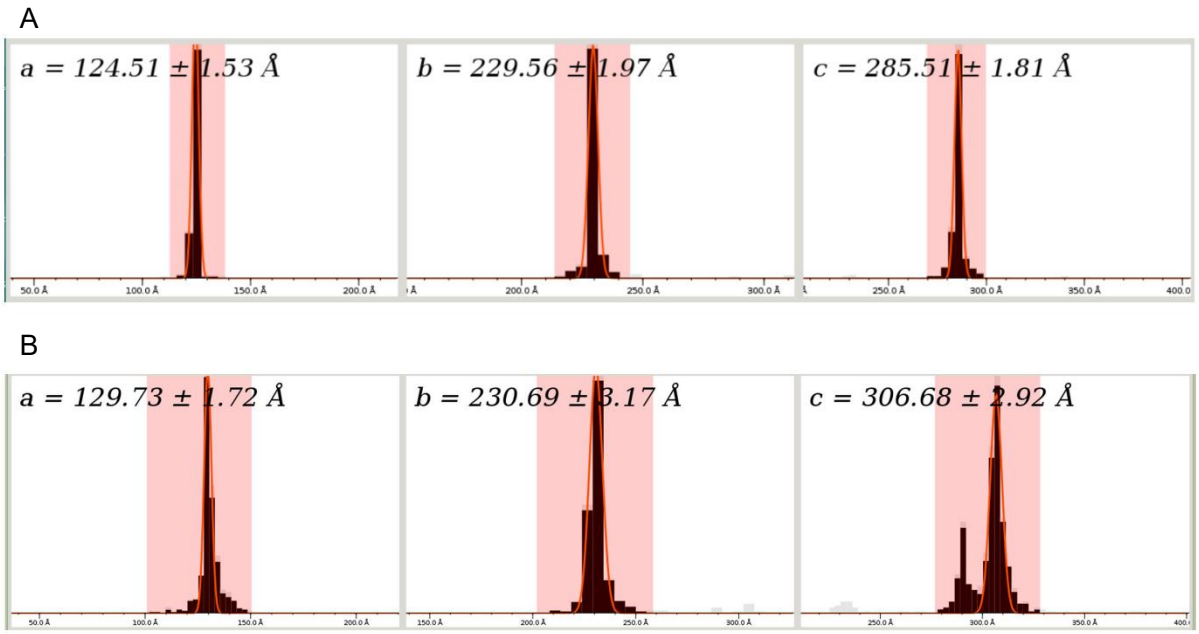

Fig. 1-9. Distributions of unit cell parameters from PSII micro-crystals treated by a post-crystallization solution (A) and without the post-crystallization treatment (B). Numbers represent the average unit cell lengths and their standard deviations.

Structural changes induced by 2-flash illumination

From the diffraction datasets obtained from the micro-crystals without light illumination (dark, S_1-state) and illuminated with 2 flashes (S_3-state), difference Fourier map between the 2F- and dark-states was calculated. The results showed main difference electron densities around the Mn_4CaO_5-cluster and the Q_B-binding site. The difference electron densities observed around the Q_B head group and its isoprenoid tail suggested a slight rotation of the Q_B molecule, which is likely caused by reduction of a part of Q_B by the 2 flashes illumination, leading to accumulation of a negative charge in a part of the Q_B molecule. The rotation of the Q_B molecule resulted in a slight shortening of the hydrogen-bonds between the head of Q_B and its nearby amino acid residues D1-His 215 and D1-Ser 264, probably due to the partial negative charge retained in the Q_B molecule.

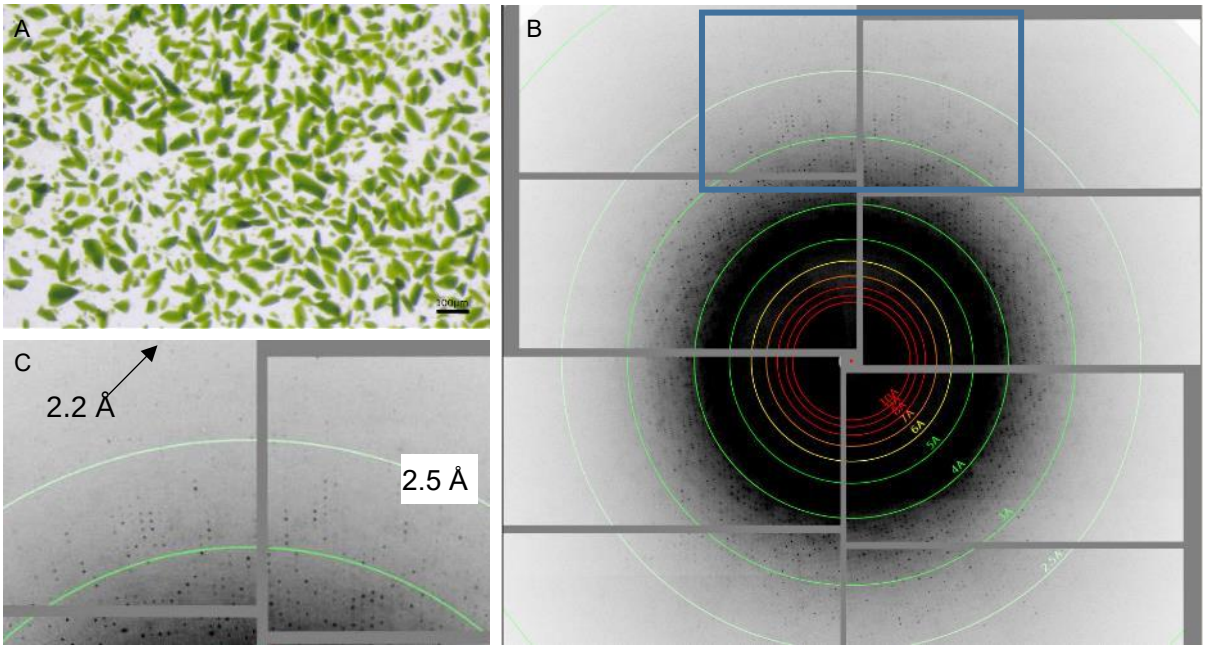

Fig. 1-10. Diffraction images of the PSII micro-crystals by a pulse of XFEL provided by SACLA, after optimization of the crystallization method and post-crystallization treatment conditions. A, PSII micro-crystals of actually utilized for the pump-probe SFX experiments. B and C, A typical diffraction image from a micro-crystal shown in panel A, taken with a single, femtosecond XFEL pulse at SACLA. Panel C is an enlarged view of the squared region in panel B. Arrow indicates the maximum diffraction spot.

In the region around Mn_4CaO_5 cluster, several difference electron densities were found. Among these, a strong positive electron density was found close to O_5, which was modelled as a new oxygen atom O6. This resulted in a Mn_4CaO_6 cluster structure for the S_3-state, as shown in Fig. 1-11. Since the newly inserted O6 is very close to O5, it is possible for these two oxygen atoms to form a molecular oxygen. These results strongly suggest that O5 provides one of the substrate oxygen atom for the dioxygen formation, and the reaction site is located around the O5 region. In addition, a strong negative electron density was observed on the water molecule W665, indicating displacement of W665 upon 2 flashes illumination. Since W665 is one of the water molecules that form a hydrogen-bond network starting from O4 of the Mn_4CaO_5 cluster and end at the lumenal surface of the PSII complex, the displacement of W665 breaks this hydrogen-bond network. This suggests that this hydrogen-bond

network functions to transport a proton during the transition from S_1 to the S_3-state, and the structural changes caused by the 2 flashes illumination that caused the breakage of the hydrogen-bond network is necessary to prevent back transport of the proton to O4. In relation to this, water molecule W567 (which is hydrogen-bonded to O4 and W665) moved towards O4, resulting in a smaller distance between W567 and O4.

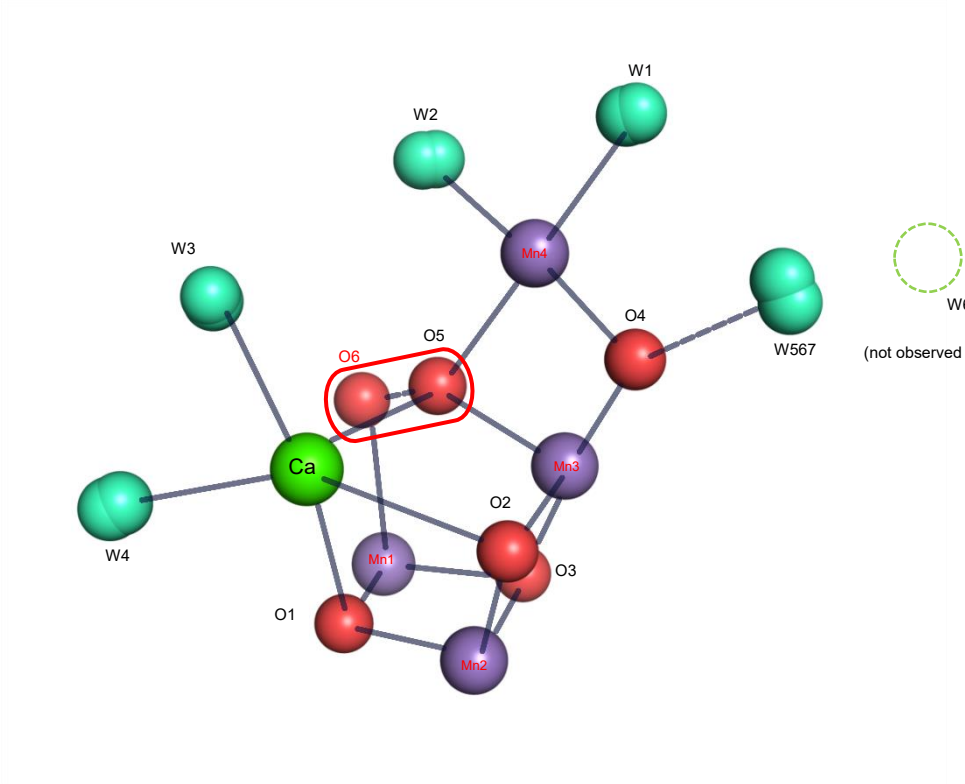

Fig. 1-11. Structural model of the Mn_4O_6Ca cluster induced by 2 flashes illumination (S_3-state). O6 is inserted near O5 atom, and W665 observed in the S_1-state structure is displaced in the S_3-sate structure. Purple balls labeled Mn1-4 represent Mn ions; red balls labeled 1-6 represent the oxygen atoms; green ball represents the calcium atom.

DISCUSSIONS

In this study, we mainly performed culture and purification of the PSII dimers in a large scale, optimization of the PSII micro-crystallization and post-crystallization conditions for structure analysis of the intermediate S-states of PSII using a pump-probe approach by the XFEL-SFX experiment. Achievement of high-quality PSII micro-crystals in a large amount was essential for this experiment. Based on the optimization process of crystallization, it was found that the crystal size should be in the range of 50-100 μm in order to obtain diffraction images at reasonably high resolution. This is in agreement with another report showing that around 50 μm-sized PSII crystals are necessary for obtaining datasets with a high resolution (11).

Three types of the micro-crystallization methods were tested. The seeding method tested in this study yielded crystals with rather regular shapes and sharp edges, but the crystals were rather thin. These crystals diffracted at lower resolutions than the crystals obtained with the pipetting method which have a rather round shape but are thicker than those produced by the seeding method. This suggests that a sufficient thickness of the crystals is more important than the length of them to obtain higher resolutions from the PSII micro-crystals. Therefore, improvement of the crystal quality by increase of crystal sizes from 30-50 μm to around 100 μm may also be a result of an increase in the thickness.

In the pipetting and tube vortex method, production of larger crystals to be used for seed solution is not necessary, and therefore they are relatively easy to use for the optimization of crystallization conditions. Since the SFX experiment requires an extremely large volume of micro-crystals, a simple method of crystallization is important for obtaining such a large amount of the PSII micro-crystals as well as for screening of the crystallization conditions to obtain high quality micro-crystals. After screening various conditions with these two methods, the tube vortex method was chosen since it gave rise higher resolution micro-crystals in a larger yield, enabling us to obtain enough PSII micro-crystals to be used in the pump-probe SFX experiments.

To obtain the high resolution from the PSII micro-crystals, they must be treated with cryo-protectant solutions to allow shrinkage of the crystals. I screened several conditions of the cryo-protectant solutions, and determined the best condition for obtaining the higher resolution. Finally, the PSII micro-crystals are mixed with a grease as the matrix to deliver the samples into a jet stream for the SFX experiment. Three types of greases were examined based on the shapes and diffraction resolutions of the PSII micro-crystals after mixing with the greases. Among these, the nuclear vacuum grease gave the best resolution,

so it was used for the matrix to deliver the PSII micro-crystals.

The PSII micro-crystals prepared above were used for the pump-probe SFX experiment, and diffraction datasets were obtained for the dark-stable S_1-state (without light illumination) and the S_3-state (after 2 flashes illumination) at 2.35 Å resolutions. Fourier difference electron density map between these two datasets showed insertion of an oxygen atom, O6 in a position close to O5 in the 2 flash-induced PSII structure. This result suggests that O6 and O5 form the O=O bond, and O5 is one of the substrates for molecular oxygen. This is in agreement with an earlier theoretical research (12). Furthermore, displacement of W 665 and approach of W567 to O4 were observed, which suggests a proton transfer through the hydrogen-bond network connected by these water molecules during the S_1-to-S_3 transition.

Since the structure of the S_3-state was successfully determined, the structure of the S-state beyond the S_3-state, namely, the S_0-state, needs to be determined to elucidate the structural changes accompanying release of the molecular oxygen. This may allow us to observe the O=O bond formation between O5 and O6 and the release of molecular oxygen. We have tried to collect the diffraction data from the PSII micro-crystals after 3 flashes illumination with the same method as that used for the S_3-state. However, no apparent difference electron densities were observed between the dark and 3 flashes illuminated states. This suggests that the PSII micro-crystals we used after the cryo-protectant treatment are unable to advance beyond the S_3-state, or have a very low efficiency for the transition beyond the S_3-state. Indeed, it was reported recently that the efficiencies of $S_2 \rightarrow S_3$ transition of PSII in the crystal state and after treatment of high concentrations of PEG largely decreased (13). Thus, the cryo-protectant treatment by high concentration of PEG used in this study may have disturbed the state transition of $S_3 \rightarrow S_0$. In the future, the post-crystallization conditions will have to be improve to ensure a high efficiency of the S-state transition beyond the S_3-state as well as a high resolution of the PSII micro-crystals.

REFFERENCES

1. Umena, Y., Kawakami, K., Shen, J.-R., and Kamiya, N. (2011) Crystal structure of oxygen-evolving photosystem II at a resolution of 1.9 Å. *Nature*, **473**, 55–60.
2. Suga, M., Akita, F., Hirata, K., Ueno, G., Murakami, H., Nakajima, Y., Shimizu, T., Yamashita, K., Yamamoto, M., Ago, H., and Shen, J.-R. (2015) Native structure of photosystem II at 1.95 Å resolution viewed by femtosecond X-ray pulses. *Nature*, **517**, 99–103.
3. Kern, J., Alonso-Mori, R., Tran, R., Hattne, J., Gildea, R. J., Echols, N., Glöckner, C., Hellmich, J., Laksmono, H., Sierra, R. G., Lassalle-Kaiser, B., Koroidov, S., Lampe, A., Han, G., Gul, S., DiFiore, D., Milathianaki, D., Fry, A. R., Miahnahri, A., Schafer, D. W., Messerschmidt, M., Seibert, M. M., Koglin, J. E., Sokaras, D., Weng, T.-C., Sellberg, J., Latimer, M. J., Grosse-Kunstleve, R. W., Zwart, P. H., White, W. E., Glatzel, P., Adams, P. D., Bogan, M. J., Williams, G. J., Boutet, S., Messinger, J., Zouni, A., Sauter, N. K., Yachandra, V. K., Bergmann, U., and Yano, J. (2013) Simultaneous femtosecond X-ray spectroscopy and diffraction of photosystem II at room temperature. *Science*, **340**, 491–495.
4. Kupitz, C., Basu, S., Grotjohann, I., Fromme, R., Zatsepin, N. A., Rendek, K. N., Hunter, M. S., Shoeman, R. L., White, T. A., Wang, D., James, D., Yang, J.-H., Cobb, D. E., Reeder, B., Sierra, R. G., Liu, H., Barty, A., Aquila, A. L., Deponte, D., Kirian, R. A., Bari, S., Bergkamp, J. J., Beyerlein, K. R., Bogan, M. J., Caleman, C., Chao, T.-C., Conrad, C. E., Davis, K. M., Fleckenstein, H., Galli, L., Hau-Riege, S. P., Kassemeyer, S., Laksmono, H., Liang, M., Lomb, L., Marchesini, S., Martin, A. V., Messerschmidt, M., Milathianaki, D., Nass, K., Ros, A., Roy-Chowdhury, S., Schmidt, K., Seibert, M., Steinbrener, J., Stellato, F., Yan, L., Yoon, C., Moore, T. A., Moore, A. L., Pushkar, Y., Williams, G. J., Boutet, S., Doak, R. B., Weierstall, U., Frank, M., Chapman, H. N., Spence, J. C. H., and Fromme, P. (2014) Serial time-resolved crystallography of photosystem II using a femtosecond X-ray laser. *Nature*, **513**, 261–265.
5. Kern, J., Tran, R., Alonso-Mori, R., Koroidov, S., Echols, N., Hattne, J., Ibrahim, M., Gul, S., Laksmono, H., Sierra, R. G., Gildea, R. J., Han, G., Hellmich, J., Lassalle-Kaiser, B., Chatterjee, R., Brewster, A. S., Stan, C. A., Glöckner, C., Lampe, A., DiFiore, D., Milathianaki, D., Fry, A. R., Seibert, M. M., Koglin, J. E., Gallo, E., Uhlig, J., Sokaras, D., Weng, T.-C., Zwart, P. H., Skinner, D. E., Bogan, M. J., Messerschmidt, M., Glatzel, P., Williams, G. J., Boutet, S., Adams, P. D., Zouni, A., Messinger, J., Sauter, N. K., Bergmann, U., Yano, J., and Yachandra, V. K. (2014) Taking snapshots of

photosynthetic water oxidation using femtosecond X-ray diffraction and spectroscopy. *Nat. Commun*., **5**, 4371.

6. Ibrahim, M., Chatterjee, R., Hellmich, J., Tran, R., Bommer, M., Yachandra, V. K., Yano, J., Kern, J., and Zouni, A. (2015) Improvements in serial femtosecond crystallography of photosystem II by optimizing crystal uniformity using microseeding procedures. *Struct. Dyn.,* **2**(4):041705.
7. Wittig, I., Karas, M., and Schägger, H. (2007) High resolution clear native electrophoresis for in-gel functional assays and fluorescence studies of membrane protein complexes. *Mol. Cell Proteomics*, **6**, 1215–1225.
8. Takasaka, K., Iwai, M., Umena, Y., Kawakami, K., Ohmori, Y., Ikeuchi, M., Takahashi, Y., Kamiya, N., and Shen, J.-R. (2010) Structural and functional studies on Ycf12 (Psb30) and PsbZ-deletion mutants from a thermophilic cyanobacterium. *Bioch. Biophys. Acta,* **1797**, 278–284.
9. Endo, K., Kobayashi, K., and Wada, H. (2016) Sulfoquinovosyldiacylglycerol has an essential role in *Thermosynechococcus elongatus* BP-1 Under phosphate-deficient conditions. *Plant Cell Physiol.,* **57**, 2461–2471.
10. Sugahara, M., Mizohata, E., Nango, E., Suzuki, M., Tanaka, T., Masuda, T., Tanaka, R., Shimamura, T., Tanaka, Y., Suno, C., Ihara, K., Pan, D., Kakinouchi, K., Sugiyama, S., Murata, M., Inoue, T., Tono, K., Song, C., Park, J., Kameshima, T., Hatsui, T., Joti, Y., Yabashi, M., and Iwata, S. (2015) Grease matrix as a versatile carrier of proteins for serial crystallography. *Nat. Methods*, **12**, 61–63.
11. Young, I. D., Ibrahim, M., Chatterjee, R., Gul, S., Fuller, F., Koroidov, S., Brewster, A. S., Tran, R., Alonso-Mori, R., Kroll, T., Michels-Clark, T., Laksmono, H., Sierra, R. G., Stan, C. A., Hussein, R., Zhang, M., Douthit, L., Kubin, M., de Lichtenberg, C., Long Vo, P., Nilsson, H., Cheah, M. H., Shevela, D., Saracini, C., Bean, M. A., Seuffert, I., Sokaras, D., Weng, T.-C., Pastor, E., Weninger, C., Fransson, T., Lassalle, L., Bräuer, P., Aller, P., Docker, P. T., Andi, B., Orville, A. M., Glownia, J. M., Nelson, S., Sikorski, M., Zhu, D., Hunter, M. S., Lane, T. J., Aquila, A., Koglin, J. E., Robinson, J., Liang, M., Boutet, S., Lyubimov, A. Y., Uervirojnangkoorn, M., Moriarty, N. W., Liebschner, D., Afonine, P. V., Waterman, D. G., Evans, G., Wernet, P., Dobbek, H., Weis, W. I., Brunger, A. T., Zwart, P. H., Adams, P. D., Zouni, A., Messinger, J., Bergmann, U., Sauter, N. K., Kern, J., Yachandra, V. K., and Yano, J. (2016) Structure of photosystem II and substrate binding at room temperature. *Nature*, **540**, 453–457.
12. Yamanaka, S., Isobe, H., Kanda, K., Saito, T., Umena, Y., Kawakami, K., Shen, J.-R., Kamiya, N., Okumura, M., Nakamura, H., and Yamaguchi, K. (2011) Possible mechanisms for the O-O bond

formation in oxygen evolution reaction at the $CaMn_4O_5(H_2O)_4$ cluster of PSII refined to 1.9 Å X-ray resolution. *Chem. Phys. Lett.,* **511**, 138–145.

13. Kato, Y., Akita, F., Nakajima, Y., Suga, M., Umena, Y., Shen, J.-R., and Noguchi, T. (2018) Fourier transform infrared analysis of the S-state cycle of water oxidation in the microcrystals of photosystem II. *J. Phys. Chem. Lett.,* **9**, 2121–2126.

Chapter 2

Effects of cryo-protectants on the efficiency of S-state transitions of oxygen-evolving photosystem II

ABSTRACT

Water oxidation in Photosynthesis II (PSII) is catalyzed by a Mn_4CaO_5-cluster and proceeds via the S-state cycle involving five intermediate S_i states (i =0-4). The structure of the S_1-state has been solved at a high resolution, and that of the S_3 state was also analyzed recently with a pump-probe approach using time-resolved serial femtosecond crystallography using X-ray free electron lasers (XFEL). In these studies, small PSII crystals are excited with two single turn-over laser flashes to develop the S-state to S_3. However, attempts to solve the structure of the S_0-state by 3 flashes illumination with the same approach were not successful, presumably due to the failure of S-state transition beyond the S_3-state with the PSII micro-crystals used. Since the crystals have been treated with cryo-protectants in order to obtain high resolutions, it has been suggested that a high concentration of cryo-protectant may affect the efficiency of the S-state transitions beyond the S_3-state. In this study, we examined the effects of the types and concentrations of cryo-protectant reagents on the efficiency of S-state transition with PSII solution samples by thermoluminescence measurement (TL). The results showed that a combination of high concentrations of polyethylene glycol (PEG) and glycerol largely affected the TL glow curves, suggesting an inhibition of the S-state transition under these conditions. In contrast, a high concentration of dimethyl sulfoxide (DMSO) in the absence and presence of low concentration of PEG did not change the TL grow curves and peak intensities following each flashes, whereas a high concentration of DMSO in combination with an increased concentration of PEG largely affected the efficiency of the transition after the S_2-state. These results suggest that high concentrations of PEG inhibits the S-state transition, especially those beyond the S_2-state.

INTRODUCTION

Previous studies have elucidated the detailed crystal structures of S_1 and S_3-state at a high resolution, and structural changes induced by the 2 flashes illumination indicated that a new oxygen atom, O6 was inserted between Mn1 and Mn4 and close to O5 in Mn_4CaO_5-cluster in the S_3-state. This result showed the possible site of O_2 formation and the substrates for the formation of molecular oxygen. However, it is still not clear that how molecular oxygen is released from its formation site, and where the new oxygen atom used as one of the substrates is supplied. To clarify these questions and elucidate the full mechanism of water oxidation and oxygen evolution in PSII, it is essential to analyze the structure after the S_3-state, namely the S_4 and S_0-states. To detect the structural changes from S_3 to the S_0-state by crystallographic analysis using TR-SFX, it is essential that the S-state of PSII in micro-crystals is advanced to the S_0-state with a high efficiency by 3 single-turnover flashes illumination, although contamination of several different S-states due to misses and double hits in the state transitions may make the analysis of flash-induced structural changes complicated. In our previous SFX work, analysis of Fourier transform infrared spectroscopy (FTIR) demonstrated that the population of the S_3-state after 2 flashes illumination was around 46% in the PSII micro-crystals after cryoprotectant treatment with high concentrations of polyethylene glycol (PEG) and glycerol (1, 2). Thus, the population of the S_0-state after 3 flashes illumination would be even lower under the same condition. Indeed, attempts to detect structural changes after 3 flashes illumination with the same PSII micro-crystals and same approach failed, suggesting that the S-state transition beyond the S_3-state was inhibited or had a very low efficiency under this condition.

In order to obtain a high efficiency of S-state transition beyond the S_3-state, it is necessary to optimize the cryo-protectant treatment conditions for the PSII micro-crystals. Thermoluminescence (TL) is the fluorescence emission derived from re-excited P680 chlorophyll arisen from the charge recombination between a positive charge on the donor side and a negative charge on the accepter side of PSII induced by charge separation. The peak position and shape of a TL-band depend the activation energy required for charge recombination of a charge particular pair. Hence, the properties of TL-bands are highly sensitive to the energetic gaps between donor and acceptor sides, depending on redox potentials of the recombination charge pairs, and can be used to monitor the properties of the donor and acceptor sides after some treatment. Indeed, TL measurements have been utilized to detect influences of a number of treatments on the property of electron transfer in PSII. For example, TL measurement has

been used to monitor the effects of treatment for the Ca depletion in PSII, such as low pH, chelaters (such as EDTA and EGTA), high concentration of NaCl and the combination of these treatments (3). The results obtained from these studies demonstrated that the state transition is inhibited after the S_3-state upon Ca depletion (4, 5), in agreement with the results obtained by EPR spectrum (6) and luminescence studies (7). Similarly, TL measurement demonstrated that electron transfers from Q_A to Q_B and state transition from S_2 to S_3 were affected by Cl^--depletion (8, 9). Thus, TL measurement has been widely utilized as a simple and powerful method to obtain information regarding the S-state transitions that reflects the redox potentials of the electron donor and accepter sides. In this chapter, to assess the effects of several cryo-protectant regents on the efficiency of S-state transitions, TL was used to monitor the S-state transitions after different kinds of the cryo-protectant treatment using PSII core dimer solution samples purified from *Thermosynechococcus vulcanus* to find the possible cause for the low efficiency of S-state transition and new cryo-protection conditions giving rise to a higher efficiency of S-state transition.

MATERIALS AND METHODS

Cell culture and Purification

Cell culture and purification of the PSII dimers were performed with the same method and conditions as used in Chapter 1.

Thermoluminescence analysis

TL measurement was performed on purified PSII core dimer complex at a concentration of 50 μg Chl ml^{-1} with a Thermoluminescence System TL400/PMT (Photon System Instruments) by a protocol of short dark adaptation (10) with slightly modifications. The sample (100 μl) was soaked into a filter paper with a diameter of 16 mm and laid on the surface of the measuring chamber. Excitation was provided at 20°C by a saturating red LED flash of 5 Hz after the short dark adaptation for 3min, then cooled immediately to -20°C. TL intensities were recorded with a heating range of 1.5°C sec^{-1} up to 70°C.

O_2 evolving activity

O_2 evolving activity was measured with the same procedure as that used in Chapter 1. For the

measurement of O_2 evolving activity with different incubation times, the PSII dimer samples were incubated at a concentration of 10 μg Chl ml^{-1} at 20ºC, and electron accepters were added just before the measurement.

RESULTS

TL analysis with PSII dimers treated by high concentrations of PEG and glycerol

TL measurements were first performed to examine the efficiency of the S-state transitions with the PSII sample treated by high concentrations of PEG and glycerol used for previous SFX experiment (2). The peak temperature of the TL curve with 1 single turn-over flash is derived from the charge recombination of S_2/Q_B^- (B_1 band), and appeared at around 51º C in the control condition (Fig. 2-1A), and the peak temperature after 2 flashes illumination (derived from charge recombination of S_3/Q_B^- (B_2 band)) appeared at around 43ºC (Fig. 2-1B). After 3 and 4 flashes illuminations, the intensities of TL peaks decreased and the peak temperature shifted to the lower temperature side slightly in the control sample. These features of the TL curves are consistent with those reported previously (10, 11). In the cryo-protectant treated sample, peak height of the B-band decreased significantly, and its peak temperature upshifted after one (60ºC) and two flashes (49ºC) illumination. Furthermore, TL curves after three and four flashes illumination showed not only shifts of B-band peak temperature but also additional peak at the region of higher temperatures. Consequently, oscillation pattern of the B-band peak heights in the cryo-protectant treated sample was damped significantly in comparison with that of control sample (untreated sample). When normalized on the basis of the TL height after 2-flashes illumination, the relative peak heights after 1 flash and 3 flashes illumination in the cryo-protectant treated sample were much higher than those of the control sample. These results indicate that the transition efficiencies after S_2 decreased by the cryo-protectant treatment.

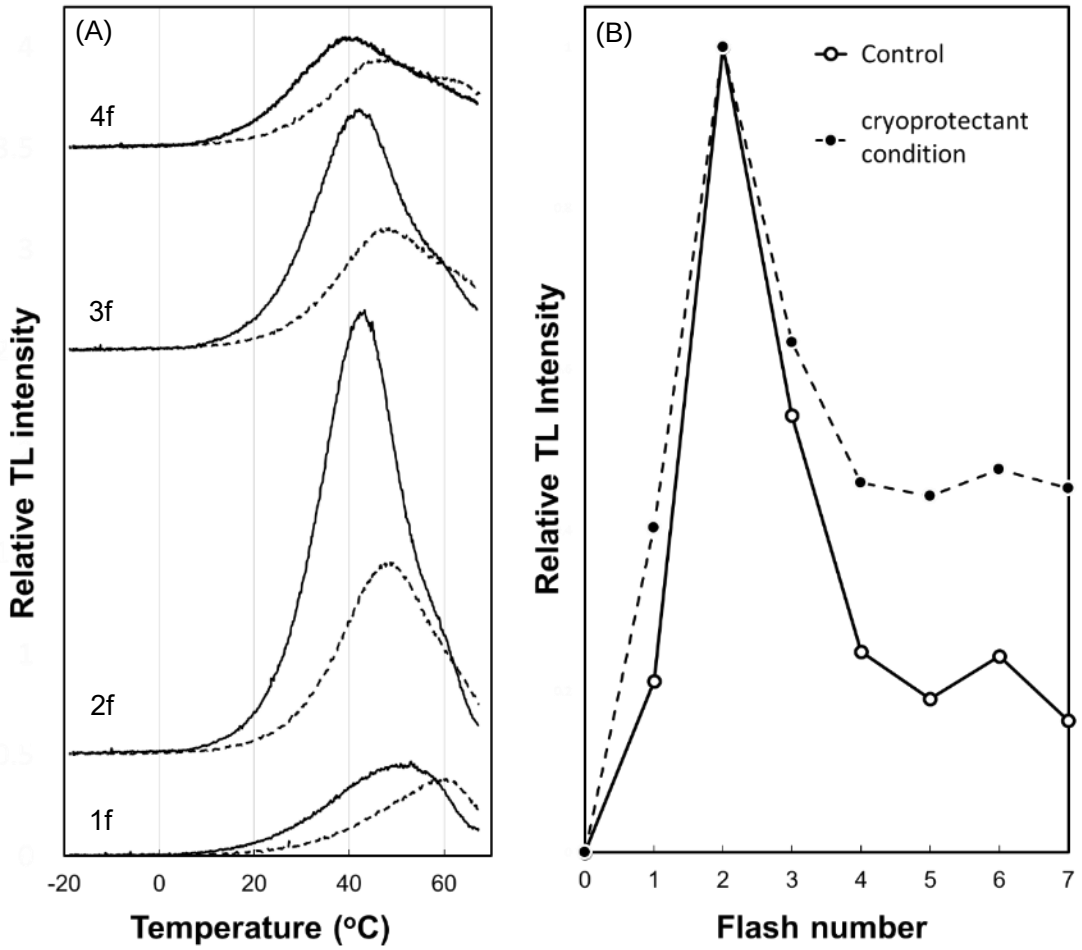

Fig. 2-1. Comparison of TL grow curves (A) and oscillation patterns of peak intensities normalized based on the height after 2-flashes (B) between control and cryo-protectant treated PSII dimers. Solid and dotted lines indicate the TL curves of control and cryo-protectant treated samples, respectively.

Comparison of TL curves between PSII samples treated with high concentrations of glycerol or DMSO

To identify the reagents that caused inhibition of the S-state transition in the cryo-protectant treated PSII dimers and search for new reagent that can serve as the cryo-protectant without causing decrease of the S-state transition, TL glow curves with PSII dimer solutions treated with a buffer containing either 20% (w/v) glycerol or 20% (w/v) DMSO were measured. As shown in Fig. 2-2, in the buffer containing 20% glycerol, the TL peak was sifted and the additional peak on high temperature region was observed

in a same manner at that seen in the PSII samples treated with a high concentration of PEG. In contrast, 20% DMSO did not affect the TL property following each flashes. These results indicate that while 20% glycerol affected the S-state transition, 20% DMSO did not significantly affect the S-state transition and thus may be used as the cryo-protectant.

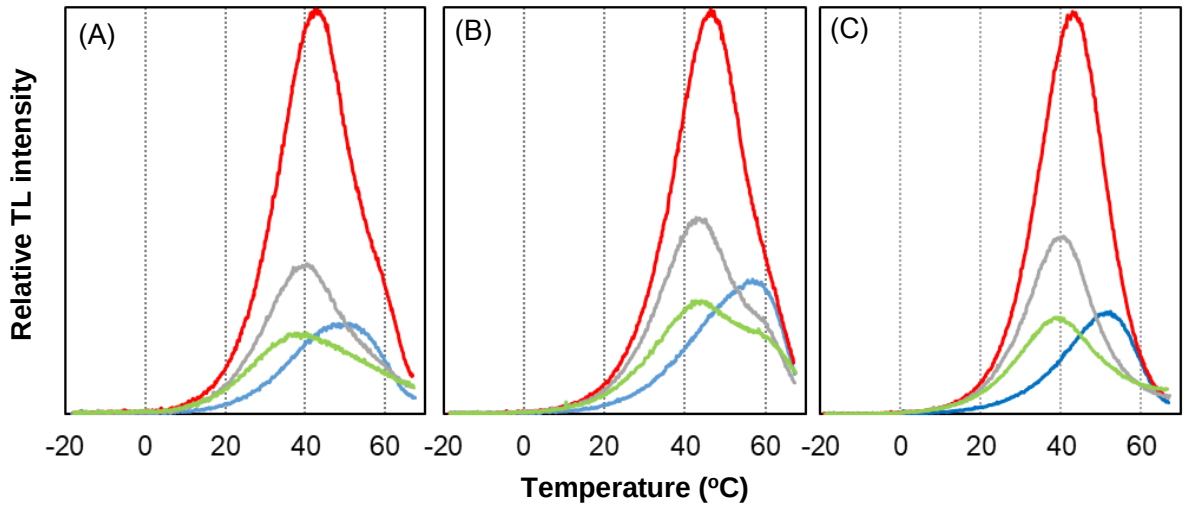

Fig. 2-2. Comparison of TL glow curves between PSII dimer diluted by storage buffer (A), the buffer containing 20% glycerol (B) and 20% DMSO (C). Blue, red, gray and green lines indicate the TL curves after 1, 2, 3 and 4 flashes respectively.

Effects of the treatment with the high concentration of DMSO on O_2 evolution activity

To examine the possible effect of the treatment with the high concentration of DMSO on the PSII activity, O_2 evolving activity of PSII dimers treated by the buffer containing 20% DMSO was measured. The result showed that the O_2 evolving activities between the control buffer without DMSO and the buffer with 20% DMSO were 1900 ± 100 and 2200 ± 210 μ mol O_2 mg Chl^{-1} h^{-1} respectively, indicating no significant differences of the PSII activity between these conditions. To further examine the effect of the treatment of DMSO by a longer time on the PSII activity, O_2 evolving activities of PSII after every one hour incubation were compared between the control buffer and the buffer containing 20% DMSO up to 4 hours. The results showed that the PSII activity gradually decreased in both samples to almost the same degree, and PSII after 4 hour incubation with 20% DMSO retained even a higher O_2 evolving

activity than that of the sample incubated with the control buffer without DMSO (Fig. 2-3). These results strongly suggest that 20% DMSO is a favorite condition for the PSII dimers to retain their O_2 evolving activity and therefore may be used as the cryo-protectant for the PSII micro-crystals.

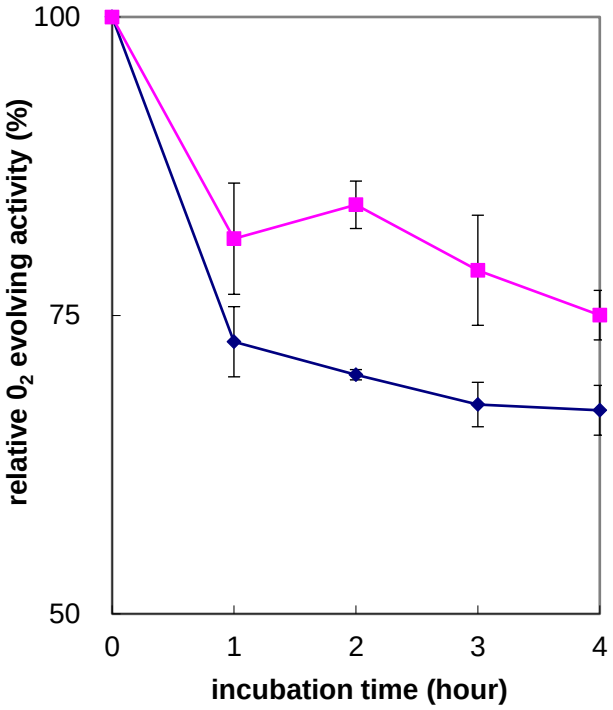

Fig. 2-3. Relative O_2 evolving activities of PSII after several hours of incubation between the storage buffer and the buffer containing 20% DMSO. Blue and violet lines indicate the O_2 evolution activities of PSII dimers incubated in the storage buffer and the buffer containing 20% DMSO, respectively. Each points were the average of 3 independent measurements.

TL intensities of PSII treated by the buffer containing 20% DMSO in combination with 14%, 16%, 18% or 20% of a PEG mixture containing the same ratio of PEG1450 and PEG5000 MME were also measured (Fig. 4A-E), and the oscillation patterns of the averaged TL peak heights were shown for each PEG conditions in Fig. 4F. As a result, the cryoprotectant condition containing a combination of high concentrations of PEG and DMSO had small influences on the shape of the TL curves and the peak temperature of the B-band (Fig. 4 A-E). However, in the buffers containing a concentration of PEG higher than 14%, the relative peak intensities after 1 and 3 flashes were higher than those observed in the control buffer without PEG, and these peak temperatures were increased with the increase in the

concentration of PEG. Comparison of oscillation patterns of the B-band showed a larger damping in 18% and 20% PEG conditions than those of the lower PEG conditions. Hence, the efficiency of the S-state transitions may be lower under higher concentrations of PEG.

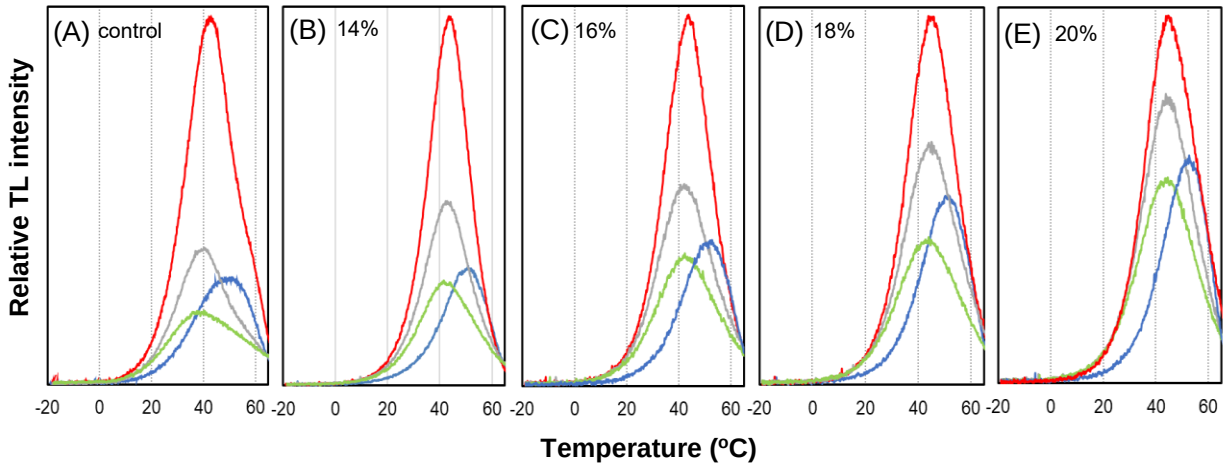

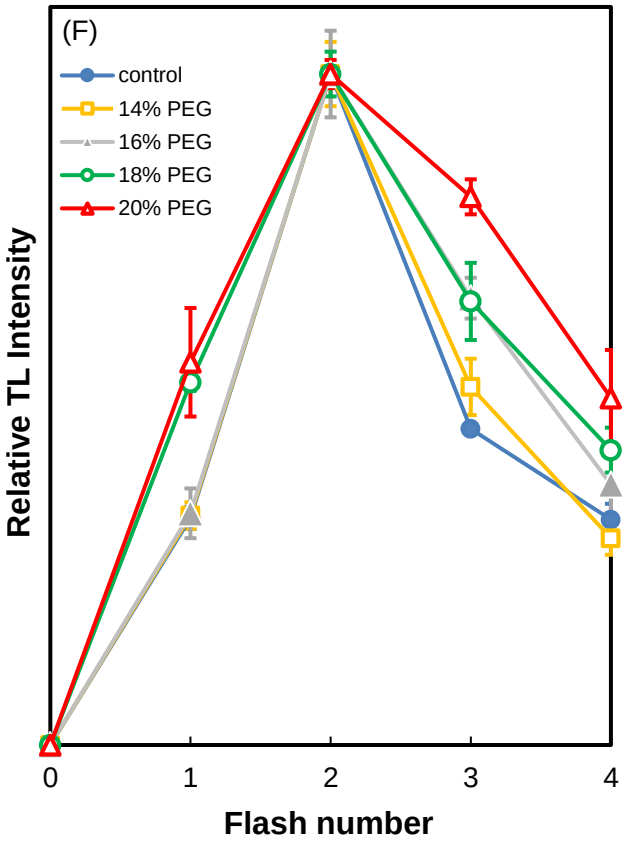

Fig. 2-4. Comparisons of TL glow curves of PSII dimer samples treated by cryo-protectant solutions containing different concentrations of PEG (A-E) and the oscillation patterns of the B-band under each PEG condition. Panels B-E show the TL glow curves in a buffer containing 20% DMSO (control PSII) (A), 20% DMSO plus 14% PEGmix (B), 16% PEGmix (C), 18% PEGmix (D), and 20% PEGmix (E). Blue, red, grey and green curves represent the TL glow curves after 1F, 2F, 3F and 4F illumination. In (F), blue line and closed circle represent the oscillation pattern of averaged TL peak intensities from condition (A), orange and closed square represent the oscillation pattern from condition (B), gray and closed triangle represent the oscillation pattern from condition (C), green and opened circle represent the oscillation pattern from condition (D), red and opened triangle represent the oscillation pattern from condition (E). Each TL peak height is the mean of three independent measurements with the standard deviation.

DISCUSSIONS

In this research, the effects of PEG, glycerol and DMSO in the cryo-protectant solution on the charge recombination between S_2/S_3 and Q_B^- of PSII were examined by TL measurements. High concentrations of PEGs have been widely used for cryo-protection of large and micro-crystals of PSII (2, 12–15). The present results however showed that a cryo-protectant solution containing 18% PEG and 22% glycerol (Fig. 2-1), or a gradual increase of PEG concentration in the presence of 20% DMSO (Fig. 2-4), affected the efficiency of the S-state transitions significantly after 2 flashes illumination with the PSII solution samples. This may be caused by a limitation of water movements by the dehydration effect of high concentrations of PEG within the PSII complex, as has been suggested by Kato et al (1). The dehydration effect of PEG may also affect the tertiary structure of some amino acid residues and ligands within PSII, causing a decrease in the O_2 evolving activity. Previous studies have shown that dehydration by PEG shifted the heme position in cytochrome *c*, resulting in changes in its redox potential (16). The structural changes were found to be below 1.0 Å, however, oxidization of the reduced cytochrome *c* was found to be remarkably promoted. Since the published crystal structures of PSII were obtained after treatment by the high concentration of PEG for freezing and shrinkage of the crystals, these structures may contain slight structural changes caused by the dehydration with the high concentration of PEG. To elucidate the possible effects of PEG on the PSII structure, structural analysis of PSII at a high resolution without the treatment with a high concentration of PEG is necessary. Cryo-

electron microscopic analysis of the PSII structure at a high resolution may provide a solution to this problem, since the cryo-electron microscopic analysis does not require crystallization and hence no high concentration of PEG is involved.

PSII dimers treated with high concentrations of glycerol showed a shift of the peak temperature of the TL emission-band to higher ones following each flash in comparison with the control sample, and additional peaks were appeared after 3 and 4 flashes illumination without decrease in the B-band intensity (Fig. 2-2). Since similar upshift of the peak temperature was found in PSII enriched membranes of spinach (17), this effect is caused by the high concentration of glycerol in the cryo-protectant solution. The appearance of similar additional peaks at higher temperatures was also observed in the Ca-deleted samples from previous TL researches (18, 19). Although little has been reported on the relationship between the effect of high concentration of glycerol and the deletion of Ca in PSII, it has been known that dissociation of extrinsic subunits caused both a deletion of Ca and decrease of oxygen evolving activity in higher plants (19, 20). These two phenomena were proposed to be caused by changes of accessibility of exogenous small molecules to the catalytic center due to the absence of extrinsic subunits. The high concentration of glycerol may also change the accessibility of exogenous small molecule to the catalytic center, resulting in the changes in the redox potential of the S-states and thus changes in TL peak temperatures resulted from charge recombination between S_2/S_3 and Q_B^-.

As an alternative cryo-protectant, 20% DMSO was used which did not significantly affect the TL-band following each flash in comparison with the control PSII samples. Although 1-2 DMSO molecules were found at a distance of around 11-13 Å from the Mn_4CaO_5-cluster in the crystal structure of PSII (21, 22), and addition of DMSO may inhibit the oxygen release because these DMSO are located inside the putative oxygen channel (21), the results of TL measurements showed no apparent effect of the high concentration of DMSO on the PSII activity. In contrast, a higher number of glycerol molecules are found close to catalytic center in the crystal structure of PSII, and the high concentration of glycerol may have caused replacement of more water molecules by glycerol molecules, thereby resulting in the inhibition of the S-state transitions and hence the changes of TL properties.

In conclusions, high concentrations of PEG largely affected the transition after S_2-state in the PSII dimer solution sample. Thus, the S-state cycle will also be inhibited by the high concentrations of PEG regardless of the crystal state or the packing pattern within the crystals. On the basis of this, screening of new cryo-protectant conditions giving rise to a high S-state transition efficiency is essential for

determination of the S-state structures beyond the S_3-state. The present results demonstrated that 20% DMSO did not affect the TL properties and O_2 evolving activity. As DMSO alone was not enough for the cryoprotectant for PSII crystals to obtain the high resolution, a combination of DMSO with a mixture of PGE1450 and PEG5000 MME was examined. It was found that a combination of 20% DMSO and up to 14% PEGmix resulted similar TL peak intensities and temperatures, suggesting that this condition did not affect the S-state transition significantly. Increase of the PEGmix concentration beyond 14% in the presence of 20% DMSO gradually affected the TL properties, suggesting the disturbances to the S-state transition. Thus, a combination of 20% DMSO and 14% PEGmix is suggested for the cryo-protectant for PSII micro-crystals. Since this condition may not be enough to allow dehydration of the PSII crystals to give a high resolution, more conditions containing a low concentration of PEG and DMSO will be screened in future.

REFERENCES

1. Kato, Y., Akita, F., Nakajima, Y., Suga, M., Umena, Y., Shen, J.-R., and Noguchi, T. (2018) Fourier transform infrared analysis of the S-state cycle of water oxidation in the microcrystals of photosystem II. *J. Phys. Chem. Lett.,* **9**, 2121–2126.
2. Suga, M., Akita, F., Sugahara, M., Kubo, M., Nakajima, Y., Nakane, T., Yamashita, K., Umena, Y., Nakabayashi, M., Yamane, T., Nakano, T., Suzuki, M., Masuda, T., Inoue, S., Kimura, T., Nomura, T., Yonekura, S., Yu, L.-J., Sakamoto, T., Motomura, T., Chen, J.-H., Kato, Y., Noguchi, T., Tono, K., Joti, Y., Kameshima, T., Hatsui, T., Nango, E., Tanaka, R., Naitow, H., Matsuura, Y., Yamashita, A., Yamamoto, M., Nureki, O., Yabashi, M., Ishikawa, T., Iwata, S., and Shen, J.-R. (2017) Light-induced structural changes and the site of O=O bond formation in PSII caught by XFEL. *Nature*, **543**, 131–135.
3. Semin, B. K., Davletshina, L. N., Ivanov, I. I., Rubin, A. B., and Seibert, M. (2008) Decoupling of the processes of molecular oxygen synthesis and electron transport in Ca^{2+}-depleted PSII membranes. *Photosynth. Res*., **98**, 235.
4. Ono, T., and Inoue, Y. (1985) S-state turnover in the O_2-evolving system of $CaCl_2$-washed Photosystem II particles depleted of three peripheral proteins as measured by thermoluminescence. Removal of 33 kDa protein inhibits S_3 to S_4 transition. *Biochim. Biophys. Acta,* **806**, 331–340.
5. Ono, T., and Inoue, Y. (1986) Effects of removal and reconstitution of the extrinsic 33, 24 and 16 kDa proteins on flash oxygen yield in Photosystem II particles. *Biochim. Biophys. Acta,* **850**, 380–389.
6. Boussac, A., and Rutherford, A. W. (1988) Nature of the inhibition of the oxygen-evolving enzyme of photosystem II induced by sodium chloride washing and reversed by the addition of calcium (2+) or strontium (2+). *Biochemistry*, **27**, 3476–3483.
7. Boussac, A., Maison-Peteri, B., Vernotte, C., and Etienne, A.-L. (1985) The charge accumulation mechanism in NaCl-washed and in Ca^{2+}-reactivated Photosystem-II particles. *Biochim. Biophys. Acta,* **808**, 225–230.
8. Vass, I., Ono, T., and Inoue, Y. (1987) Stability and oscillation properties of thermoluminescent charge pairs in the O_2-evolving system depleted of Cl^- or the 33 kDa extrinsic protein. *Biochim. Biophys. Acta,* **892**, 224–235.
9. Homann, P. H., Gleiter, H., Ono, T., and Inoue, Y. (1986) Storage of abnormal oxidants '$\sum^1$', '$\sum^2$' and '$\sum^3$' in photosynthetic water oxidases inhibited by Cl^--removal. *Biochim. Biophys. Acta,* **850**, 10–20.
10. Fufezan, C., Zhang, C., Krieger-Liszkay, A., and Rutherford, A. W. (2005) Secondary quinone in

photosystem II of *Thermosynechococcus elongatus*: Semiquinone−iron EPR signals and temperature dependence of electron transfer. *Biochemistry*, **44**, 12780–12789.

11. Sugiura, M., and Inoue, Y. (1999) Highly purified thermo-stable oxygen-evolving photosystem II core complex from the thermophilic cyanobacterium *Synechococcus elongatus* having His-tagged CP43. *Plant Cell Physiol.,* **40**, 1219–1231.
12. Kern, J., Chatterjee, R., Young, I. D., Fuller, F. D., Lassalle, L., Ibrahim, M., Gul, S., Fransson, T., Brewster, A. S., Alonso-Mori, R., Hussein, R., Zhang, M., Douthit, L., Lichtenberg, C. de, Cheah, M. H., Shevela, D., Wersig, J., Seuffert, I., Sokaras, D., Pastor, E., Weninger, C., Kroll, T., Sierra, R. G., Aller, P., Butryn, A., Orville, A. M., Liang, M., Batyuk, A., Koglin, J. E., Carbajo, S., Boutet, S., Moriarty, N. W., Holton, J. M., Dobbek, H., Adams, P. D., Bergmann, U., Sauter, N. K., Zouni, A., Messinger, J., Yano, J., and Yachandra, V. K. (2018) Structures of the intermediates of Kok's photosynthetic water oxidation clock. *Nature*, **563**, 421–425.
13. Suga, M., Akita, F., Hirata, K., Ueno, G., Murakami, H., Nakajima, Y., Shimizu, T., Yamashita, K., Yamamoto, M., Ago, H., and Shen, J.-R. (2015) Native structure of photosystem II at 1.95 Å resolution viewed by femtosecond X-ray pulses. *Nature*, **517**, 99–103.
14. Hellmich, J., Bommer, M., Burkhardt, A., Ibrahim, M., Kern, J., Meents, A., Müh, F., Dobbek, H., and Zouni, A. (2014) Native-like photosystem II superstructure at 2.44 Å resolution through detergent extraction from the protein crystal. *Structure*, **22**, 1607–1615.
15. Umena, Y., Kawakami, K., Shen, J.-R., and Kamiya, N. (2011) Crystal structure of oxygen-evolving photosystem II at a resolution of 1.9 Å. *Nature*, **473**, 55–60.
16. Sato, W., Uchida, T., Saio, T., and Ishimori, K. (2018) Polyethylene glycol promotes autoxidation of cytochrome *c*. *Biochim. Biophys. Acta Gen. Subj*., **1862**, 1339–1349.
17. Krieger, A., Rutherford, A. W., and Jegerschöld, C. (1998) Thermoluminescence measurements on chloride-depleted and calcium-depleted photosystem II. *Biochim. Biophys. Acta,* **1364**, 46–54.
18. Ono, T., and Inoue, Y. (1990) Abnormal redox reactions in photosynthetic O_2-evolving centers in NaCl/EDTA-washed PSII. A dark-stable EPR multiline signal and an unknown positive charge accumulator. *Biochim. Biophys. Acta,* **1020**, 269–277.
19. Ono, T., and Inoue, Y. (1989) Removal of Ca by pH 3.0 treatment inhibits S_2 to S_3 transition in photosynthetic oxygen evolution system. *Biochim. Biophys. Acta,* **973**, 443–449.
20. Halverson, K. M., and Barry, B. A. (2003) Sucrose and glycerol effects on photosystem II. *Biophys. J.,*

85, 1317–1325.

21. Gabdulkhakov, A., Guskov, A., Broser, M., Kern, J., Müh, F., Saenger, W., and Zouni, A. (2009) Probing the accessibility of the Mn_4Ca cluster in photosystem II: Channels calculation, noble gas derivatization, and cocrystallization with DMSO. *Structure*, **17**, 1223–1234.
22. Uto, S., Kawakami, K., Umena, Y., Iwai, M., Ikeuchi, M., Shen, J.-R., and Kamiya, N. (2017) Mutual relationships between structural and functional changes in a PsbM-deletion mutant of photosystem II. *Faraday Discuss*., **198**, 107–120.

Chapter 3

Thylakoid membrane lipid sulfoquinovosyl-diacylglycerol (SQDG) is required for full functioning of photosystem II in *Thermosynechococcus elongatus*

ABSTRUCT

Sulfoquinovosyl-diacylglycerol (SQDG) is one of the four lipids present in the thylakoid membranes, depletion of which causes different degrees of effects on photosynthetic growth and activities in different photosynthetic organisms. Crystal structure of photosystem II (PSII) has revealed the presence of four SQDGs in a PSII monomer. To clarify the functions of SQDG in PSII, we analyzed the activities of PSII from an SQDG-deficient mutant of *T. elongatus* by various spectroscopy, which showed that depletion of SQDG impaired the PSII activity slightly caused by impairment of Q_B exchange at the acceptor site. We further solved the crystal structure of the PSII dimer from the ΔSQDG-mutant at 2.1 Å resolution, and found that all of the four SQDG-binding sites are occupied by other lipids, mostly likely PG molecules. This is the first crystal structure of PSII showing that the bound lipids are compensated for by other lipids. The replacement of two SQDGs located at the monomer-monomer interface by other lipids caused monomerization of PSII dimer in the mutant, and the replacement at the third SQDG located close to the head of Q_B may be the cause for impairment of Q_B exchange at the acceptor side. These results suggest that binding of lipids is necessary in all of the SQDG binding sites to fully maintain the activity and stability of PSII, and replacement of SQDG by other lipids can partially compensate for their functions. Thus, these binding sites are evolved to best accommodate SQDGs and indispensable for the full functioning of PSII.

INTRODUCTION

Thylakoid membranes of oxygenic photosynthetic organisms contain four types of lipids, monogalactosyl-diacylglycerol (MGDG), digalactosyl-diacylglycerol (DGDG), sulfoquinovosyl-diacylglycerol (SQDG) and phosphatidyl-glycerol (PG) (1, 2). The relative content of these lipids is largely conserved among different organisms, with MGDG, DGDG and SQDG comprising the majority of the lipids and PG as a minor class (2). The roles of lipids can be classified into two-folds, one is to form the lipid bilayer whereas the other one is to associate with some specific sites of membrane protein(s) to function as an essential part of that protein(s). MGDG and DGDG are nonionic lipids and are considered to function mainly as structural lipids for the formation of the lipid bilayer, whereas SQDG and PG are acidic lipids and are probably required to maintain the balance of negative charges in the thylakoid membranes (3, 4). In addition, all of these lipids are found to bind directly to photosynthetic membrane-protein complexes such as photosystem II (PSII), photosystem I (PSI) and cytochrome b_6f (5–8), and therefore may be required to maintain the integral functions of these protein complexes. In fact, deletion of PG by inactivating the genes for PG synthesis has been shown to inhibit the growth of cyanobacteria, which is caused mainly by the decrease in the activity and stability of PSII, indicating that PG plays an important role in the PSII activity (9, 10).

The roles of SQDG have been studied in various organisms by mutagenesis to inactivate the genes responsible for the SQDG synthesis. It was found that the extent of the effects caused by deletion of SQDG is different among different organisms. In *Arabidopsis thaliana* and two species of cyanobacteria (*Synechococcus elongatus* PCC 7942 and a marine cyanobacterium *Synechococcus* sp. PCC 7002), inactivation of the genes for SQDG synthesis resulted in very little effects on their growth, oxygen evolving activity and the sensitivity to herbicides such as 3-(3,4-dichlorophenyl)-1,1-dimethylurea (DCMU) under normal growth conditions (11–13). The effects of SQDG depletion, however, became much more severe under PG-limiting conditions caused by phosphate (Pi)-deficiency or by genetic disruption of the PG biosynthesis pathway (3, 11, 14). In *Chlamydomonas reinhardtii*, deletion of the gene for SQDG synthesis resulted in a decrease of oxygen-evolving activity by 30-40% and an increase in the sensitivity to DCMU (15-17). In addition, the mutant cells showed a lower resistance to heat- or hydroxylamine (NH_2OH)-treatment (17, 18), suggesting an impairment in the oxygen-evolving complex of PSII. On the other hand, depletion of SQDG completely inhibited the growth of *Synechocystis* sp. PCC 6803 cells concomitant with a decrease in the PSII activity (19). The inhibition of growth caused

by SQDG depletion, however, was found to be caused by the inhibition in DNA synthesis instead of the inhibition of the photosynthetic activities (20), although it is not clear why depletion of SQDG inhibits DNA synthesis in *Synechocystis* sp. PCC 6803 but not in other cyanobacteria, and how this inhibition occurs. Recently, the gene *sqdB* responsible for SQDG-synthesis was disrupted in a thermophilic cyanobacterium *Thermosynechococcus elongatus* BP-1, and the resulted mutant (Δ*sqdB*) was characterized in terms of growth and photosynthetic activities (3). It was found that the Δ*sqdB* mutant had a slightly decreased growth rate and O_2 evolving activity than the WT under normal growth conditions, and both PSII dimer and PSI trimer were monomerized, with PSII dimer almost disappeared. The relative content of PG was remarkably increased in the SQDG-deletion mutant under phosphate-sufficient conditions, and the effects of SQDG became much more severe under phosphate-limiting conditions. These results suggested that SQDG may play important roles in photosynthesis and PSII, but its role is partly compensated for by PG, resulting in a phenotype similar to that of WT under phosphate-sufficient conditions. However, it is unclear if the role of SQDG is general as a structural lipid in maintaining the integrity of the lipid bilayer, or specific in maintaining the structures and functions of the photosynthetic systems, and if the SQDG-binding sites in the mutant have been occupied indeed by PG or other lipids.

High resolution structural analysis of PSII dimer from the thermophilic cyanobacterium *T. vulcanus* has revealed binding of four SQDG molecules in a PSII monomer (5, 21, 22) (Fig. 3-1A). Among them, two are located in the monomer-monomer interface (Fig. 3-1A, 1B, 1D, SQDG-1, SQDG-2, corresponding to SQDG418/A and SQDG103/L, respectively, in the pdb file 3WU2). The third one is located in the boundary between the CP47 and D2 proteins and near the quinone electron accepter Q_B (SQDG-3, corresponding to SQDG412/A of the pdb file 3WU2), and the final one is located in an area between PsbX and PsbF (cytochrome b_{559} β-subunit) (SQDG-4, SQDG407/D in the pdb file 3WU2) (Fig. 3-1A, 1C, 1E). In the structure of the PSII monomer from *T. elongatus* analyzed at 3.6 Å resolution (23), one of the two SQDGs (SQDG-1) located in the monomer-monomer interface of the dimer was not found, suggesting that SQDG may be required for the dimerization of PSII monomer in the assembly process. However, the exact roles of SQDG in PSII are still unclear, since no structure of SQDG-deleted PSII has been solved, so it is unclear if the binding sites of SQDG are replaced by other lipids/molecules or completely empty upon depletion of SQDG, and if there are any structural changes in the SQDG-binding regions caused by the depletion of SQDG.

To examine the roles of SQDG in PSII in more detail, we characterized the functions of PSII from the SQDG-deletion mutant Δ*sqdB* of *T. elongatus* by Fourier transform infrared spectroscopy (FTIR), thermoluminescence (TL) and delayed light fluorescence (DL) measurements in either thylakoid membranes or purified PSII dimers. We further crystallized and analyzed the crystal structure of PSII dimers purified from the SQDG-deletion mutant. Based on the results obtained, we discuss the functions of SQDG in PSII from a structural point of view.

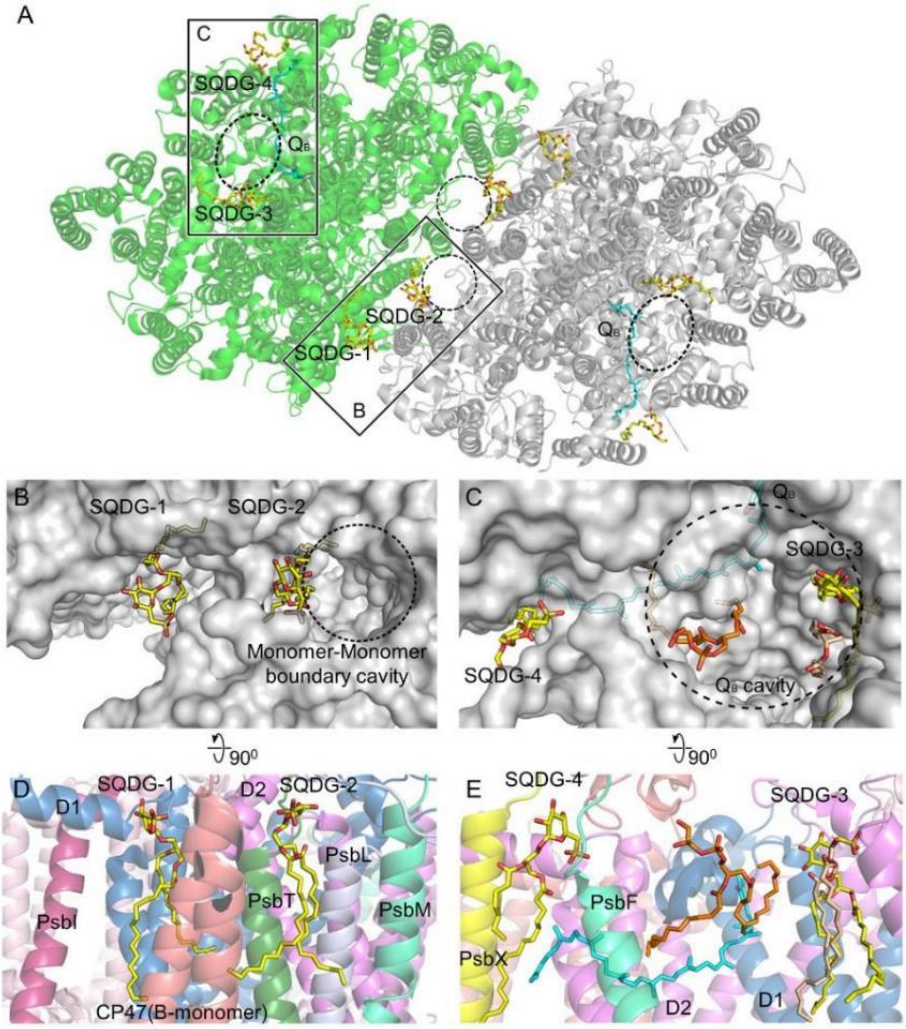

Fig. 3-1. Location of SQDG molecules in a PSII dimer of WT (pdb: 3WU2). *A.* Overall structure of WT-PSII dimer with a top view from the cytoplasmic side. *B, C.* Surface model view of the enlarged squared region in shown in panel *A. D, E.* View with a rotation of 90 degrees relative to panels *B* and *C*, respectively, in a cartoon model. All four SQDG molecules in each PSII monomer are located within the membrane close to the stromal side, with their negatively charged head groups facing the stromal

surface. In the monomer-monomer interface, two SQDGs (SQDG-1, -2) bind to each monomer in a fashion resembling a clamp. SQDG-3 is close to the Q_B cavity and binds to a position about 10 Å away from Q_B across the D1-loop. On the other hand, SQDG-4 is located between PsbX and PsbF with its tail close to the isoprenoid tail of Q_B. Color codes: SQDG, yellow stick; Q_B, cyan stick; PG, orange stick.

MATERIALS AND METHODS

Cell culture and purification

ΔSQDG strain was constructed by deleting the *sqdB* gene from *T. elongatus* as described previously (3), and the deletion of the *sqdB* gene was confirmed by PCR (Fig. 3-2). PCR was performed by previous method and by primers for check of segregation (3). Basically, cell culture and harvest were performed by using protocol of WT with slightly modification (See Chapter 1). Liquid culture of cells for small scale was grown at 45°C in the presence of 15 μg ml^{-1} chloramphenicol. For purification of the PSII dimer sample, 40 L of the mutant cells were grown for 7-9 days in the absence of chloramphenicol. The cultured cells were harvested by centrifugation at 13,800 g for 15min at 4°C (R9A rotor, HITACHI KOKI) and precipitant was washed by a buffer of 40mM KH_2O_4-KOH (pH 6.8). After centrifugation at 13,800 g for 10 min, the precipitant was suspended by the buffer of 0.4 M mannitol, 40 mM KH_2O_4-KOH (pH 6.8) and incubated 120 min after addition of 1 mM EDTA-2Na, 0.14% (w/v) lysozyme as final concentration. Incubated cell was centrifuged at 13,800 g for 10 min, the precipitated cells were suspended by buffer-D. Crude PSII of ΔSQDG was also obtained with almost the same protocol as that used for WT. After 1st LDAO treatment and centrifugation, the precipitant was suspended by buffer-D and treated by 0.36-0.45% (v/v) LDAO as the 2nd LDAO treatment. The crude PSII was purified by anion exchange chromatography. PSII dimer fraction obtained was concentrated by PEG precipitation, the precipitant was suspended by the storage buffer and stored at -180°C.

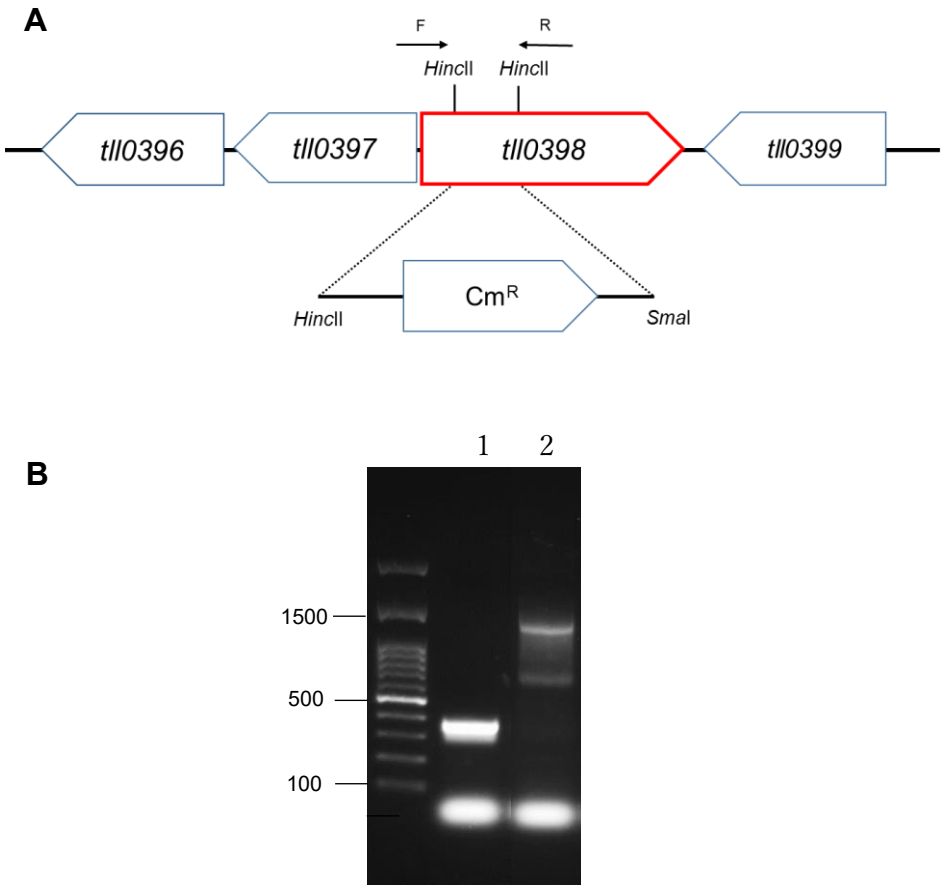

Fig. 3-2. Disruption of the *sqdB* gene (*tll0398*) in *T. elongatus BP-1*. (A) Structure of the genomic region around the *sqdB* gene (*tll0398*) of *T. elongatus BP-1*. For mutation of *sqdB* gene, a 1.5 kb chloramphenicol-resistant gene cassette (Cm^R) was inserted into the digestion site of the *sqdB* gene (3). (B) PCR analysis confirmed the insertion of the Cm^R in the *sqdB* gene with a 0.3 kb deletion of the native sequence. PCR products with genomic DNA of the wild type (WT) and the *sqdB* mutant are shown with a molecular size marker (Nippon genetics DNA ladder, NE-MWD100). Lane1: WT, Lane2; Δ*sqdB* mutant

Clear Native PAGE and gel-filtration chromatography

To analyze the purity of ΔSQDG-PSII purified by the anion exchange chromatography, CN-PAGE and gel-filtration chromatography was performed. CN-PAGE was carried out with the same method as used in Chapter 1. For gel-filtration chromatography, PSII was suspended by the storage buffer to a final concentration of 0.1 mg Chl ml^{-1}, and centrifuged at 22,000 g for 5 min, then 40 µl of sample were injected onto a Superdex-200 HR30/10 column (GE-Healthcare UK, Ltd). The sample loaded was eluted by a buffer containing 20 mM Mes-NaOH (pH 6.0), 150 mM NaCl, 0.03% β-DDM, and monitored at

280 nm. This experiment was controlled by an HPLC system (SMART system, GE Healthcare)

Oxygen evolution, TL and DL measurements

Oxygen evolution of thylakoid membranes and PSII dimers was measured with the same method as that used for WT (Chapter 1). TL measurements were performed using a laboratory-built apparatus as described previously (24). For measurement of the Q band, thylakoids (250 μg of Chl ml^{-1}) in the presence of 50 μM DCMU were illuminated with continuous white light (~55 mW cm^{-2} at the sample point) from a halogen lamp (MEJIRO PRECISION PHL-150) for 10 s at −20°C. For measurement of the B band, thylakoids (250 μg of Chl ml^{-1}) were illuminated with a single Xe flash at 5°C. The sample was quickly cooled down and then warmed at a rate of 40°C min^{-1} to record the TL glow curves.

For delayed fluorescence (DL) measurements, thylakoids (250 μg of Chl mL^{-1}) were illuminated with a series of Xe flashes (0.5 Hz) at 40°C. The DL intensity at 1.8 s after each flash was normalized based on the maximum DL intensity of each sample during the measurement with the train of flashes, and plotted against the flash number.

FTIR measurements

PSII core complexes were washed in a buffer containing 1 mM Mes-NaOH (pH 6.0), 5 mM NaCl, 5 mM $CaCl_2$, and 0.03% β-DDM and concentrated to ~4.5 mg of Chl ml^{-1} by ultrafiltration (Vivaspin 500, 100 kDa molecular mass cutoff). An aliquot of 10 μl of the concentrated PSII was mixed with 1 μL of 100 mM potassium ferricyanide on a CaF_2 plate (25 mm in diameter) and dried by a stream of nitrogen gas on ice in the dark. The resultant sample was resuspended with 1 μl of 200 mM Mes-NaOH (pH 6.0) and sandwiched with another CaF_2 plate as described previously (25). The sample temperature was kept at 10°C by circulating cold water through a copper holder.

Light-induced FTIR difference spectra were recorded using a Bruker IFS-66/S spectrophotometer equipped with an MCT detector (InfraRed D313-L) at 4 cm^{-1} resolution. The samples were stabilized at this temperature in the dark for 4 h before the spectra were recorded. For the measurements of S-state transitions, flash illumination was performed by a Q-switched Nd:YAG laser (Quanta-Ray GCR-130; 532 nm, ~7 ns full width at half-maximum) with a power of ~7 mJ $pulse^{-1}$ cm^{-2} at the sample position. The samples were illuminated by two preflashes (1 Hz) followed by dark adaptation for 30 min to synchronize all centers to the S_1-state. Twelve flashes were applied to the sample at intervals of 10 s; a

single-beam spectrum (20 scans) was measured twice before the 1st flash and once after each flash. The samples were then dark adapted for 30 min again. This whole measurement scheme was repeated six times, and the spectra were averaged (120 scans in total). Difference spectra upon individual flashes were calculated to provide structural changes during S-state transitions, while a difference spectrum between the two spectra before the 1st flash represented the noise level. Spectral fitting and simulation of the oscillation pattern were performed using Igor Pro (WaveMetrics Inc.) according to the equation described previously (25).

Lipid analysis

Lipids in the WT and ΔSQDG PSII samples were extracted by the method described previously (26) and separated by thin layer chromatography. Each lipid class was quantified by gas chromatography as described previously (27, 28).

Crystallization and structural analysis

The purified ΔSQDG-PSII dimers were crystallized using the oil batch method under conditions similar to those previously described (5, 29) with slight modifications as follows. In the first step of crystallization, many multi-clustered and needle-clustered crystals were obtained; they were collected individually, washed by a crystallization buffer containing 10% PEG1450 and used for the second time of crystallization. The crystals grew to a size of 0.7 x 0.4 x 0.1 mm^3 for 5~7days at 12^oC, and they were transferred to a cryoprotection solution by increasing the concentrations of dimethyl sulfoxide (DMSO) and PEG gradually to a final concentration of 25% DMSO and 20% PEG3,000. The crystals were then flash-frozen in a nitrogen gas stream at 100 K. X-ray diffraction data were collected at the beamlines BL41XU, BL38B1 of SPring-8, Japan at a wavelength of 1.0 Å. The dataset obtained was indexed, integrated and scaled with XDS (30). The initial phase up to 4 Å resolution was obtained by molecular replacement with the program Molrep (31) using the 1.90 Å resolution structure of native PSII (PDB accession code 3WU2) as the search model, and the structure was refined to 2.10 Å resolution with Refmac5 in the CCP4 program suit (32). WT-PSII dimers were crystallized under the same conditions, and diffraction data from the WT-PSII crystals with a similar resolution and statistic values to that of ΔSQDG-PSII were selected and analyzed (Table 2-2). In order to identify the positions of phosphorus atoms, four diffraction datasets were collected at a wavelength of 1.9 Å where the anomalous signal

from the phosphorous atoms were visible in the WT-PSII structure. These datasets were processed and merged with XDS, and the initial phases were determined by the molecular replacement as described above. Each phases were combined with CAD in the CCP4 program suit (33) to produce a high-redundancy anomalous dataset. Based on this dataset, anomalous difference Fourier map was calculated with FFT in the CCP4 program suit. The calculated anomalous map and refined model based on the dataset collected at 1.0 Å wavelength was superposed for comparisons of the positions of the lipid head group between SQDG and PG. Root mean-square deviation between the Cα atoms of WT- and ΔSQDG-PSII structures was calculated with lsqkab in the CCP4 program suit (34). Model building was performed with COOT (35), and figures were made with PyMol (36).

RESULTS

Analyses on the content of PSII dimer and oxygen evolution

Previously it was shown by blue native PAGE analysis that inactivation of the *sqdB* gene (Fig. 3-2) in the thermophilic cyanobacterium remarkably affected the stability of the PSII dimer, resulting in a large increase in the content of PSII monomer and an almost disappearance of PSII dimer in the mutant (3). In the procedure we used to purify the PSII dimer here, the elution pattern from the ion-exchange column chromatography constantly showed that the fraction containing the PSII monomer was much larger than that of dimer (Fig. 3-3). This contrasts with the situation observed in WT where the fraction of PSII dimer is much larger than that of PSII monomer, indicating that inhibition of SQDG synthesis destabilized the PSII dimer, in agreement with the previous results (3). The purification procedure we used here, however, still yielded a considerable fraction of PSII dimer, allowing us to perform the subsequent crystallization and structural analysis of the PSII dimer. The difference in the amount of PSII dimers observed in the previous and present study may be due to the different purification procedures and/or analysis methods employed. In both cases, however, it is clear that inhibition of SQDG synthesis destabilized the PSII dimer, resulting in the increase in the amount of PSII monomer. All analysis described below are performed with the PSII dimers from the mutant and compared with the PSII dimers of WT.

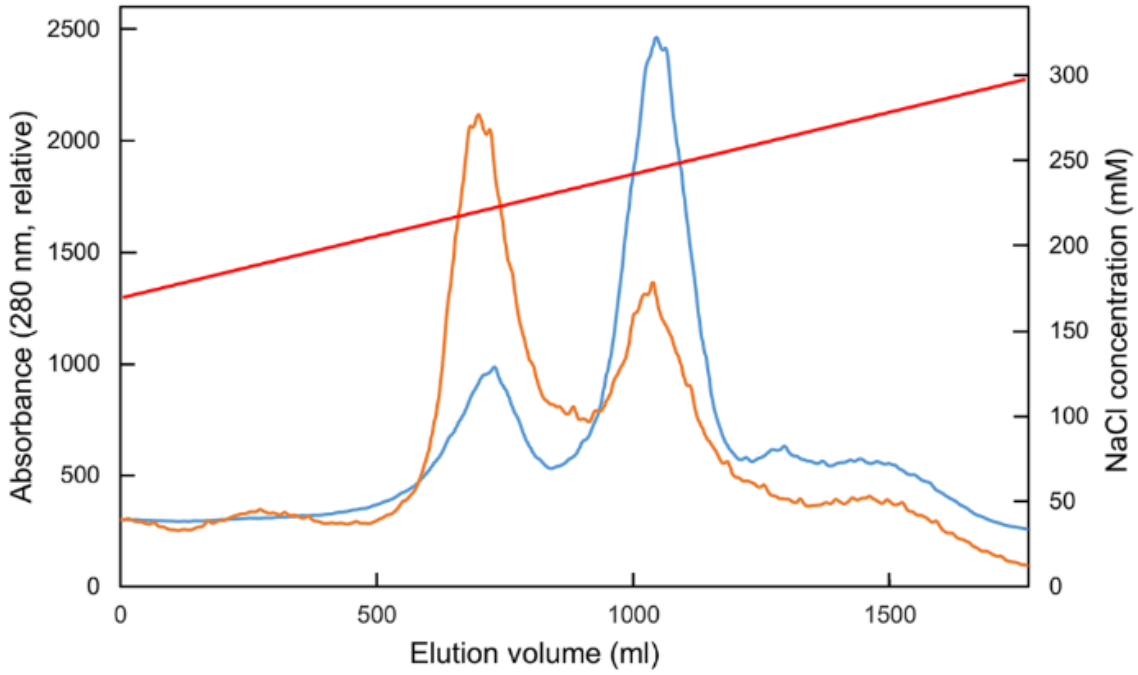

Fig. 3-3. Anion exchange column chromatography of crude PSII samples after solubilization with 1.0% β-DDM from WT (blue line) and the ΔSQDG mutant (orange line). Q-sepharose high performance was used for the column, and the samples were eluted with a liner gradient of NaCl from 170 to 300 mM, and the eluent was monitored by absorption at 280 nm.

The Δ*sqdB* mutant cells have been shown to have slightly decreased oxygen-evolving activity in the presence of PSII electron acceptors (3). We further compared the oxygen-evolving activities of isolated thylakoid membranes and PSII dimers between WT and ΔSQDG with 0.4 mM phenyl p-benzoquinone and 1 mM potassium ferricyanide as electron acceptors. The results showed that the oxygen-evolving activity of the mutant samples decreased by about 19-32% in the thylakoid membranes and purified PSII dimers (Table 3-1). This decrease is comparable with those observed with the mutant cells of *T. elongatus* reported previously (3), and also with the previous report in the *C. reinhardtii* mutant with the SQDG synthesis gene inactivated (15-17). To examine the causes for the decrease of PSII activity in detail, we performed spectroscopic analyses with the WT and ΔSQDG samples.

Table 3-1. Comparison of oxygen evolving activities of thylakoid membranes and isolated PSII dimers from the wild type and ΔSQDG mutant strains. Each values are averages of 5 independent samples.

Strain	Thylakoid membranes	PSII dimers
WT	140 ± 10	1790 ± 80
ΔSQDG	110 ± 10	1210 ± 100

Clear Native PAGE (CN-PAGE) and gel-filtration chromatography

In chromatogram of gel-filtration (Fig. 3-4A), single peak from PSII dimer solution was observed, indicating that this ΔSQDG-PSII has sufficient purity for its crystallization. The chromatogram from PSII monomer fraction indicates the contamination of PSII dimer as usual with WT-monomer. Comparison of WT- and ΔSQDG-PSII in CN-PAGE (Fig. 3-4B) also indicated that the purity of ΔSQDG-PSII is comparable to that of WT-PSII, and thylakoid membrane of ΔSQDG-PSII (lane. 2 in Fig. 3-4B) indicates large increase of PSII monomer and PSI monomer, consisting with previously report (3).

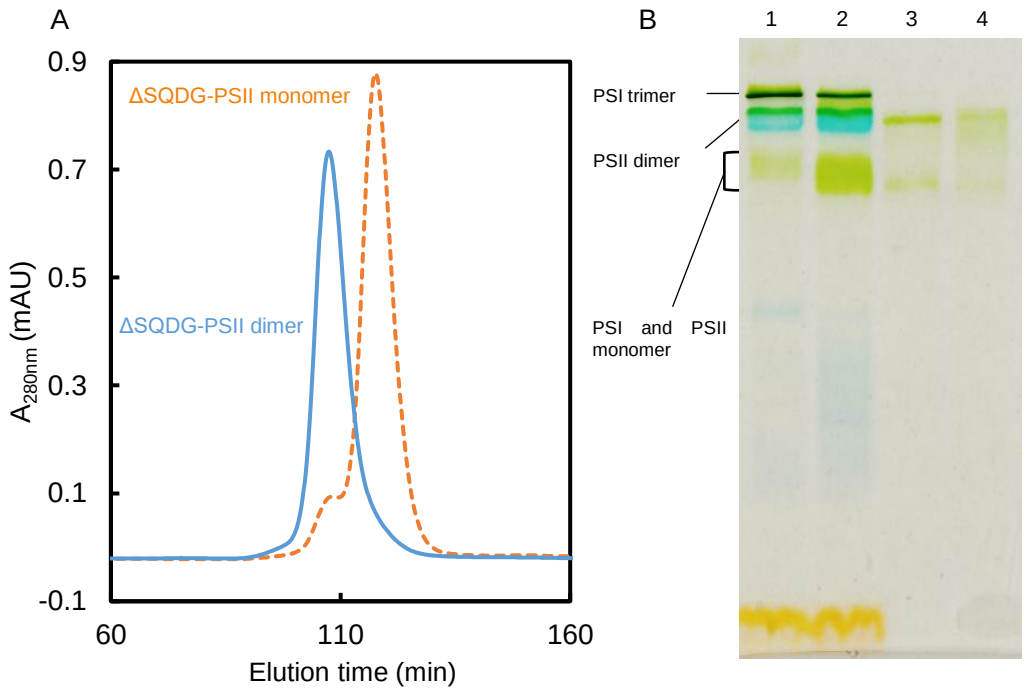

Fig. 3-4. Checking the purity of PSII dimer (A) Gel-filtration pattern of purified ΔSQDG-PSII dimer (blue solid line) compared to ΔSQDG-PSII monomer (orange dashed line). (B) Comparison of thylakoid membrane and purified PSII dimer between WT and ΔSQDG used by Clear Native PAGE. Lane 1: WT thylakoid membrane, lane 2: ΔSQDG thylakoid membrane, lane 3: WT-PSII, lane 4: ΔSQDG-PSII.

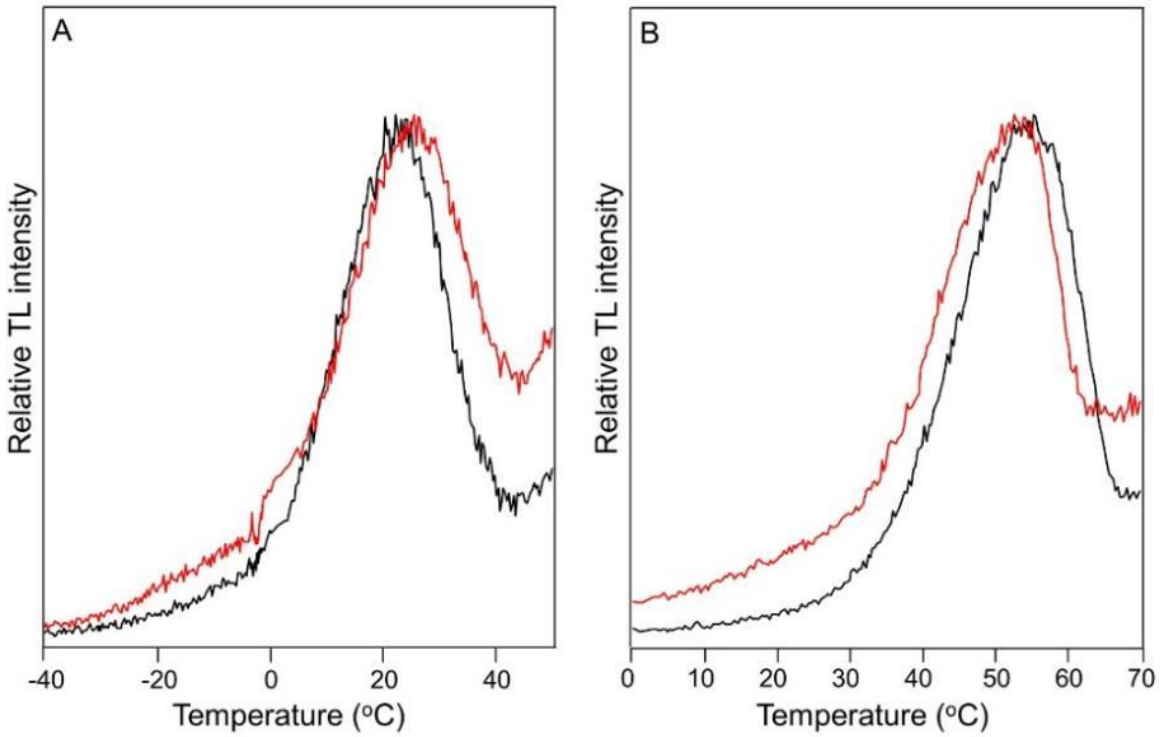

Fig. 3-5. TL glow curves of thylakoid membranes from WT and ΔSQDG. TL glow curves were measured in the presence (*A*) or absence (*B*) of DCMU. In both panels, the black curves were obtained from WT thylakoid membranes, and red curves were from the ΔSQDG thylakoid membranes.

Spectroscopic analyses (TL, FTIR and DL measurements) of the PSII activities

The S-state transitions of the WT and ΔSQDG thylakoid membranes were examined by TL in either the presence or absence of DCMU. As shown in Fig. 3-5, the TL glow curves in both the presence and absence of DCMU were very similar between the WT and the ΔSQDG mutant, suggesting that the redox potential of the S_2/S_1 couple on the electron donor side and those of Q_A/Q_A^- and Q_B/Q_B^- on the acceptor side were not significantly changed by depletion of SQDG.

The properties of S-state transition were further examined by flash-induced FTIR spectroscopy with purified PSII dimers from WT and the ΔSQDG mutant. As shown in Fig. 3-6A, the 1st and 2nd-flash induced FTIR difference spectra exhibited negative bands in the symmetric COO^- stretching region (1450−1300 cm^{-1}), whereas the 3rd and 4th-flash induced difference spectra exhibited positive bands in this region, in the WT-PSII. These features are identical to those of active PSII reported previously (25, 37), and represent the structural changes in the $S_1 \rightarrow S_2$, $S_2 \rightarrow S_3$, $S_3 \rightarrow S_0$, and $S_0 \rightarrow S_1$ transitions, respectively. The spectral features of 5th/9th, 6th/10th, 7th/11th, and 8th/12th flashes were similar to those of 1st, 2nd, 3rd, and 4th flashes, respectively, although their intensity were gradually decreased by increasing the flash numbers (Fig. 3-6A). The damping of the FTIR difference spectra is attributed to the misses in the S-state transitions, which increase the mixture of other transitions at increased flash numbers (38). All of these spectral features were found to be similar in the ΔSQDG-PSII mutant (Fig. 3-6A), suggesting that depletion of SQDG did not affect the structures and reactions of the water-oxidizing center significantly. Oscillation of the S-state transition was examined by plotting the intensity difference between the FTIR peaks at 1437 and 1401 cm^{-1} against the flash number, with normalization against the same intensity difference observed at the 1st-flash spectrum. Typical period-four oscillation patterns were observed in both WT and mutant PSII samples (closed circles in Fig. 3-6B and 3-6C). The oscillation pattern was simulated with a conventional method based on the equation employed previously, assuming an average efficiency for the different S-state transitions (25). Good fittings were obtained for both WT and ΔSQDG mutant PSIIs (open triangles in Fig. 3-6B and 3-6C), and their average efficiencies were estimated to be 88 ± 2% and 86 ± 2%, respectively. These average efficiencies were almost the same between the WT and ΔSQDG. Since the present FTIR measurements of S-state transition were performed in the presence of ferricyanide as an exogenous electron acceptor, the results obtained suggest that depletion of SQDG did not affect the PSII donor side significantly.

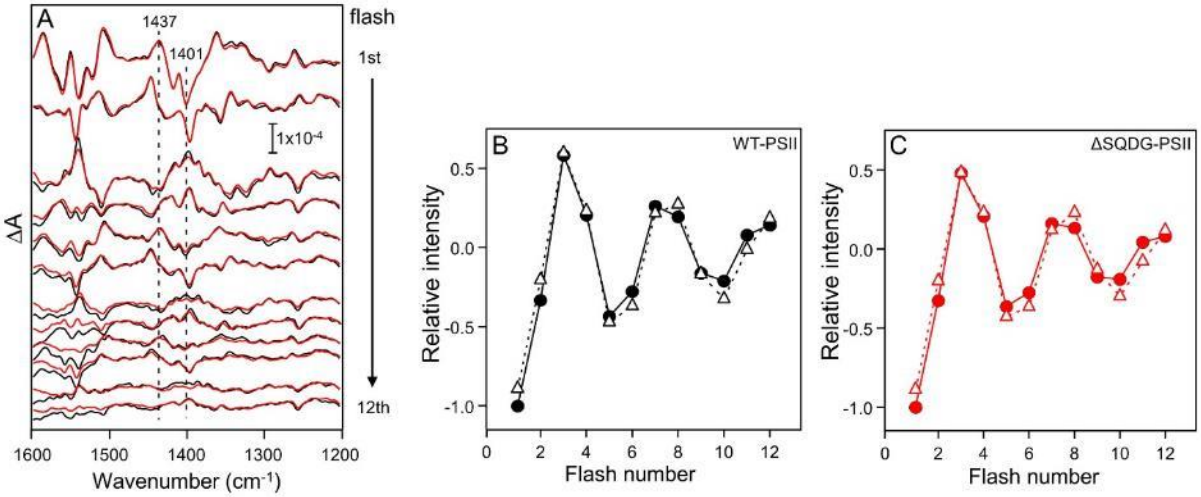

Fig. 3-6. Flash-induced FTIR difference spectra of the S-state cycle (*A*), and flash-number dependence of the relative amplitude and simulated oscillation pattern (*B, C*) in intact PSII core dimers purified from WT and the ΔSQDG mutant. *A.* FTIR measurement was performed by using 100 mM potassium ferricyanide as an electron accepter. Each line indicates the difference spectrum at each flash number from the top to bottom. Black line is obtained from WT-PSII core dimer, and red line from the ΔSQDG-PSII core dimer. *B* and *C*. Intensity differences between 1437 and 1401 cm^{-1} in the FTIR difference spectra (closed circles with solid lines) were plotted against the flash number with simulated intensities (open triangles with dotted lines). *B* and *C* indicate the oscillation patterns from the WT-PSII and ΔSQDG-PSII core dimers respectively.

The electron transfer properties of PSII from ΔSQDG mutant were further examined by DL measurements, which originates from the charge recombination and back reaction from the PSII acceptor side. As shown in Fig. 3-7, the DL intensity from the WT thylakoid membranes exhibited a typical period-four oscillation during 12 flashes illumination (black line). The oscillation pattern of the DL intensities from the ΔSQDG mutant sample was remarkably changed in the mutant in comparison with the WT (red line), with almost no further oscillations after 7th flash. Since the donor side and the electron transfer from Q_A to Q_B were not changed in the mutant based on the FTIR and TL results shown above, the DL results indicate that depletion of SQDG affected the exchange of plastoquinole after reduction of Q_B at the acceptor side.

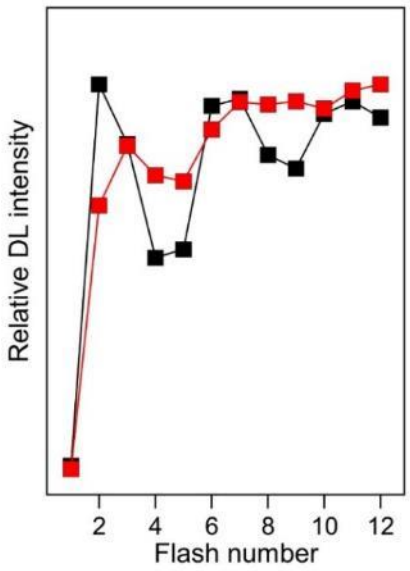

Fig. 3-7. Oscillation pattern of the S-state transition of DL intensities measured by 12 flashes. Black and red lines correspond to the oscillation patterns of the WT and ΔSQDG mutant thylakoid membranes, respectively.

Crystal structure analysis of the ΔSQDG-PSII dimer

The crystal of ΔSQDG-PSII was diffracted to a resolution of 1.9 Å at maximum (Fig. 3-8). Finally, the structure of ΔSQDG-PSII dimer was analyzed at a resolution of 2.1 Å with X-ray diffraction data collected at a wavelength of 1.0 Å (Table 3-2). The overall structure of the ΔSQDG-PSII dimer obtained is very similar to that of the native PSII, with a root-mean-squared deviation (RMSD) of 0.32 Å between the Cα atoms of WT and ΔSQDG-PSII. To examine the SQDG-binding sites in detail, we calculated the |*Fo*|-|*Fc*| difference map for the mutant PSII. The results showed that all of the four SQDG-binding sites have positive electron densities, indicating that the four SQDG-binding sites are not empty but have been occupied by some other molecules in the mutant PSII (Fig. 3-9, 3-10). Among them, the 2|*Fo*|-|*Fc*| map for the binding sites of SQDG-1, SQDG-2 and SQDG-3 clearly showed fatty acid tails of diacylglycol (Fig. 3-9A, B, C, and Fig. 3-10), suggesting that these sites are replaced by other types of lipids. However, the electron densities for their head groups are distorted and not clearly defined, which prevented us to assign the lipid classes into these sites unambiguously. Among the other classes of lipids, DGDG has a much larger head group and cannot fit with the electron density, whereas the head groups of MGDG and PG are rather similar and therefore cannot be distinguished based on the 2|*Fo*|-|*Fc*| and |*Fo*|-|*Fc*| maps. We also collected datasets at 1.9 Å wavelength and analyzed the structure to 2.4 Å

resolution in order to locate the possible phosphorus atoms by its anomalous signal; however, no anomalous signals were observed in these three sites. Thus, we modelled the molecules in these SQDG-binding sites as unknown lipids.

The head group for the SQDG-4 binding site can be modeled to a PG molecule and the anomalous scattering data collected at 1.9 Å wavelength also showed apparent anomalous signals; thus, this binding site is occupied by a PG molecule.

Lipid content of the mutant PSII dimer

To confirm which lipids may have bound to the three SQDG binding sites in ΔSQDG-PSII, we analyzed the lipid contents of the PSII dimers before and after crystallization and compared them with of the WT PSII (Table 3-3). The results showed that while the numbers of MGDG and DGDG are not much different between the WT and mutant PSII, and are also consistent with those found in the crystal structure, the number of PG is 3-5 higher in the mutant than that in the WT. This suggests that all of the SQDG molecules may have been replaced by PG in the mutant PSII.

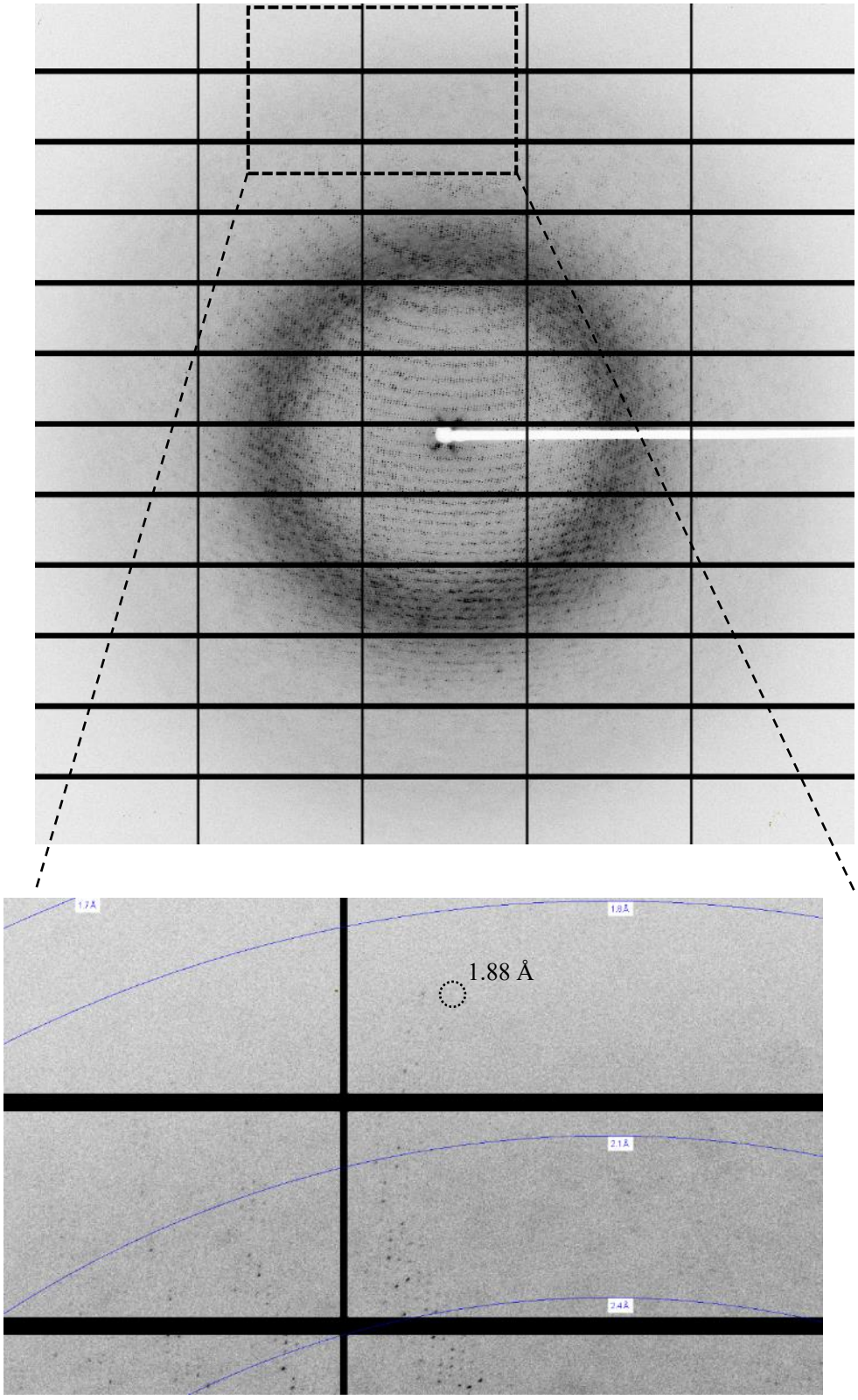

Fig. 3-8. Typical X-ray diffraction pattern of ΔSQDG-PSII crystal. The diffraction image was obtained at SPring-8, BL41XU, and utilized for this crystal structure analysis of ΔSQDG-PSII.

Table 3-2. Data collection and refinement statistics for the datasets collected at 1.0 and 1.9 Å wavelengths from the ΔSQDG-PSII and WT crystals.

Data collection	ΔSQDG-PSII		WT-PSII	
Wavelength (Å)	1.000	1.900	1.000	1.900
Space group	$P2_12_12_1$	$P2_12_12_1$	$P2_12_12_1$	$P2_12_12_1$
Unit cell (Å)	a = 122.3 b = 228.4 c = 287.1	a = 121.5 b = 228.4 c = 286.7	a=122.2 b=228.0 c=285.9	a=122.4 b=228.4, c=286.2
Resolution (Å)	20-2.10 (2.22-2.10)[a]	20-2.40 (2.46-2.40)	20- 2.10 (2.22 - 2.10)	20-2.50(2.56 - 2.50)
Unique reflections	459,862	601,068	459,932	530,440
Redundancy	6.8 (6.7)	21.74 (20.00)	6.7 (6.9)	6.2 (7.8)
Completeness	99.5 (98.5)	100 (99.8)	99.6 (99.9)	99.0 (91.2)
R_{merge}	0.087 (0.886)	0.124 (1.090)	0.066 (0.771)	0.074 (0.214)
I/σ(I)	13.7 (2.1)	18.2 (3.2)	16.4 (3.1)	19.7 (6.8)
CC(1/2)	0.998 (0.870)	0.999 (0.916)	0.999 (0.918)	0.998 (0.976) *
Refinement statistics				
R_{factor}	0.157	0.155	0.160	0.143
R_{free}	0.198	0.205	0.198	0.183
R.m.s.d. (bond) (Å)	0.021	0.018	0.022	0.018
R.m.s.d. (angle) (deg)	2.564	2.420	2.621	2.477
Ramachandran plot[b]				
Favored (%)	97.4	97.1	97.4	97.8
Allowed (%)	2.4	2.7	2.4	2.0
Outliers (%)	0.2	0.2	0.2	0.2

[a] Values in the parentheses indicate those for the highest resolution shell.

[b] Ramachandran plot was calculated with the MolProbity.

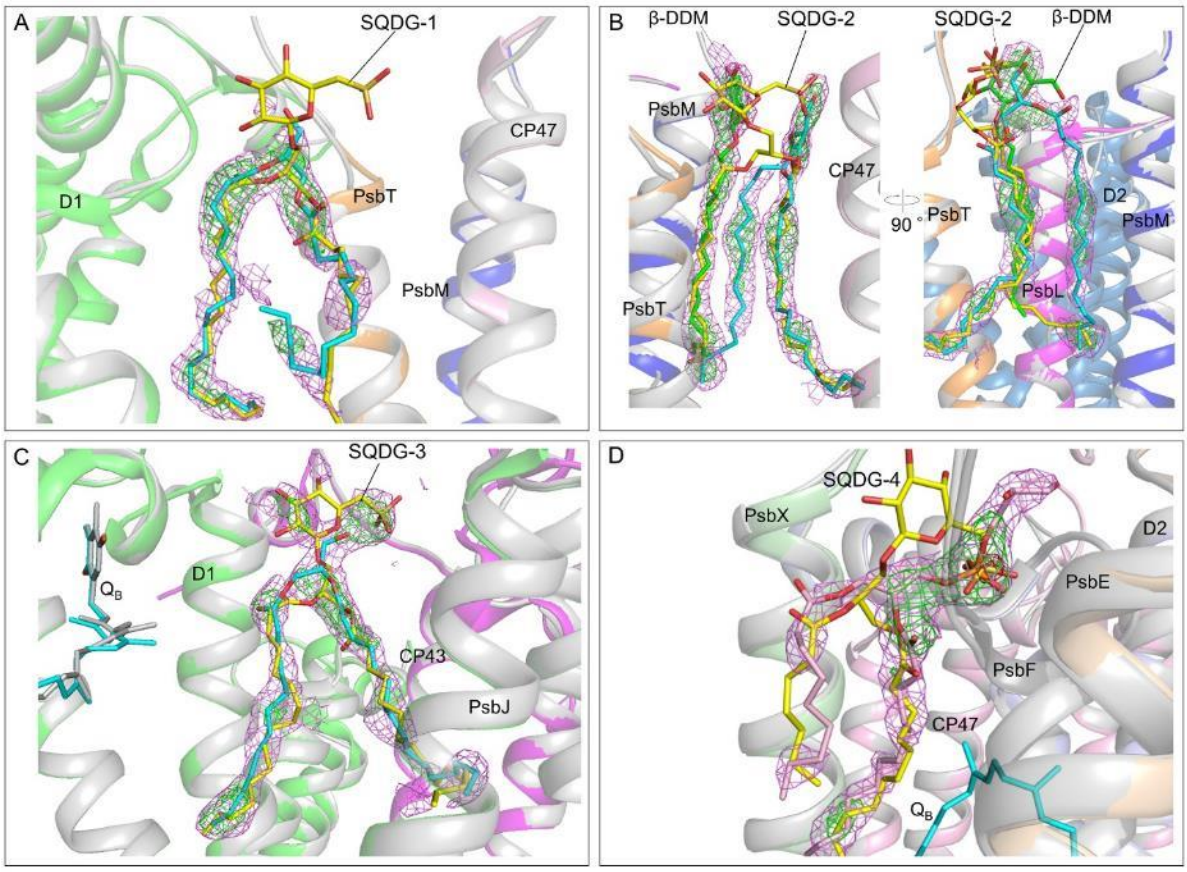

Fig. 3-9. Electron density maps around the four SQDG-binding sites in the ΔSQDG mutant and comparisons between the structures of SQDGs in WT and the substituted lipids in the mutant. In all panels, the violet and green mesh indicate 2|*Fo*|-|*Fc*| maps contoured at 0.8 σ, and SQDGs-omitted |*Fo*|-|*Fc*| maps (positive) contoured at 3.5 σ, respectively. The structures of the WT and the mutant are superimposed, where residues of WT are colored and those of the mutant are illustrated in grey. *A, B* and *C*. Electron density maps in the SQDG-1, SQDG-2 and SQDG-3 binding sites in the mutant and comparison of the structure of SQDGs in the WT with those of unknown lipids in the mutant. The unknown lipid molecules are colored in cyan, and SQDG molecules are colored in yellow. In panel *B*, two figures indicate the view from two different directions, and in the left side figure, the molecule colored in green indicates an additional β-DDM molecule in the mutant. The right side figure indicates a view rotated by 90 degrees relative to that of the left side figure. *D*. Electron density map in the SQDG-4 binding site in the mutant and comparison of the structure of SQDG in the WT with that of the PG molecule in the mutant. The PG molecule is depicted in pink. The small red mesh near the phosphorous atom of PG indicates the difference anomalous density map contoured at 4.0 σ.

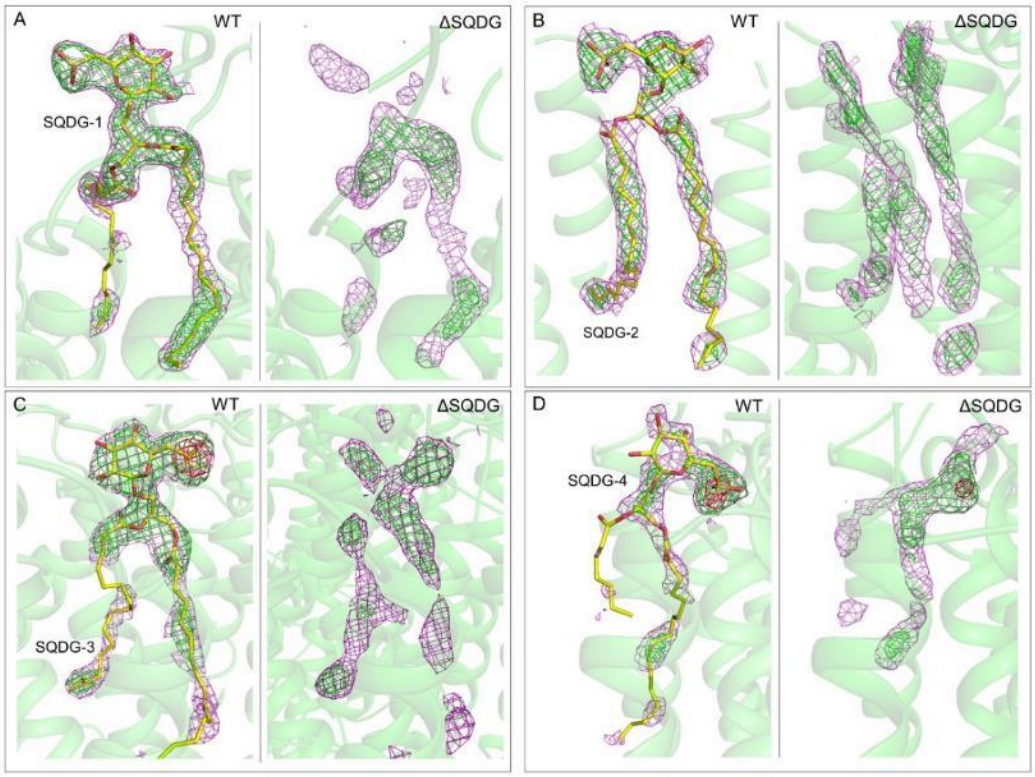

Fig. 3-10. Comparison of 2|*Fo*|-|*Fc*| and |*Fo*|-|*Fc*| electron densities and the anomalous difference densities in the four SQDG-binding sites between WT and ΔSQDG. In all panels, the violet, green and red mesh indicate 2|*Fo*|-|*Fc*| maps contoured at 0.8 σ, SQDG-omitted |*Fo*|-|*Fc*| maps (positive) contoured at 3.5 σ and anomalous difference maps countered at 4.0 σ, respectively. In WT, the density maps and anomalous difference maps were calculated from the datasets refined to 2.1 and 2.5 Å resolution collected at 0.9 and 1.9 Å wavelengths, respectively. In the WT structure, SQDG molecules depicted in yellow are fitted based on the omit 2|*Fo*|-|*Fc*| and |*Fo*|-|*Fc*| densities.

Table 3-3. Comparison of lipid composition in a PSII monomer between WT and ΔSQDG before or after crystallization.

The numbers of lipid molecules are determined based on 35 chlorophylls per PSII monomer.

		Total	MGDG	DGDG	SQDG	PG
WT-PSII	Before crystallization	24.0	8.2	6.2	4.9	4.5
	After crystallization	21.9	7.1	5.1	4.1	5.7
ΔSQDG-PSII	Before crystallization	20.6	6.5	5.0	0	9.1
	After crystallization	19.0	6.2	4.3	0	8.6
3WU2 structure		20	6	5	4	5

Structural changes caused by the depletion of SQDG

Among the two SQDGs bound in the interface between the two monomers within a dimer, SQDG-1 connects D1 from one monomer (A-monomer) with CP47 from the other monomer (B-monomer). The head group of SQDG-1 is hydrogen-bonded with D1-Trp20, D1-Asn26 of the A-monomer, and CP47-Trp113, CP47-Tyr117 of the B-monomer (Fig. 3-11A). Although depletion of SQDG did not affect the structures of the residues surrounding this binding site significantly, replacement by an unknown diacyl chain result in the breakage of most of the hydrogen-bonds, leading to a disconnection between D1 of the A-monomer and CP47 of the B-monomer (Fig. 3-11A). Even if it is replaced by a PG molecule based on the result of lipid analysis, it can form a hydrogen-bond with CP47-Trp113 only (Fig. 3-11B). This apparently weakens the interactions between the two monomers, resulting in the destabilization of the dimer in the mutant.

SQDG-2 is also located in the monomer-monomer interface. In WT, SQDG-2 is surrounded by PsbL, PsbM, PsbT subunits from the A-monomer and CP47 from the B-monomer, and forms hydrogen-bonds with PsbL-Arg14 of the A-monomer and CP47-Arg18, CP47-Trp115 of the B-monomer (Fig. 3-11B). In the ΔSQDG mutant, this SQDG is replaced again by an unknown lipid. One of the two fatty acid tails of this unknown lipid was shifted from the original position of the SQDG-2 tail and away from the A-monomer, leaving a space close to the PsbT and PsbM subunits. This space was filled by a new

n-dodecyl-β-d-maltoside (β-DDM) molecule in the mutant PSII. However, the unknown lipid and β-DDM molecule formed almost no hydrogen-bonds with the neighboring subunits. Modelling of a PG molecule into this site does not change the situation (Fig. 3-11D). Thus, the connection between the A- and B-monomers via SQDG-2 is broken in the mutant PSII. This, together with the breakage of the bridge via SQDG-1 described above, will apparently destabilize the dimer, leading to the significant monomerization of PSII in the mutant as observed in the present and previous studies.

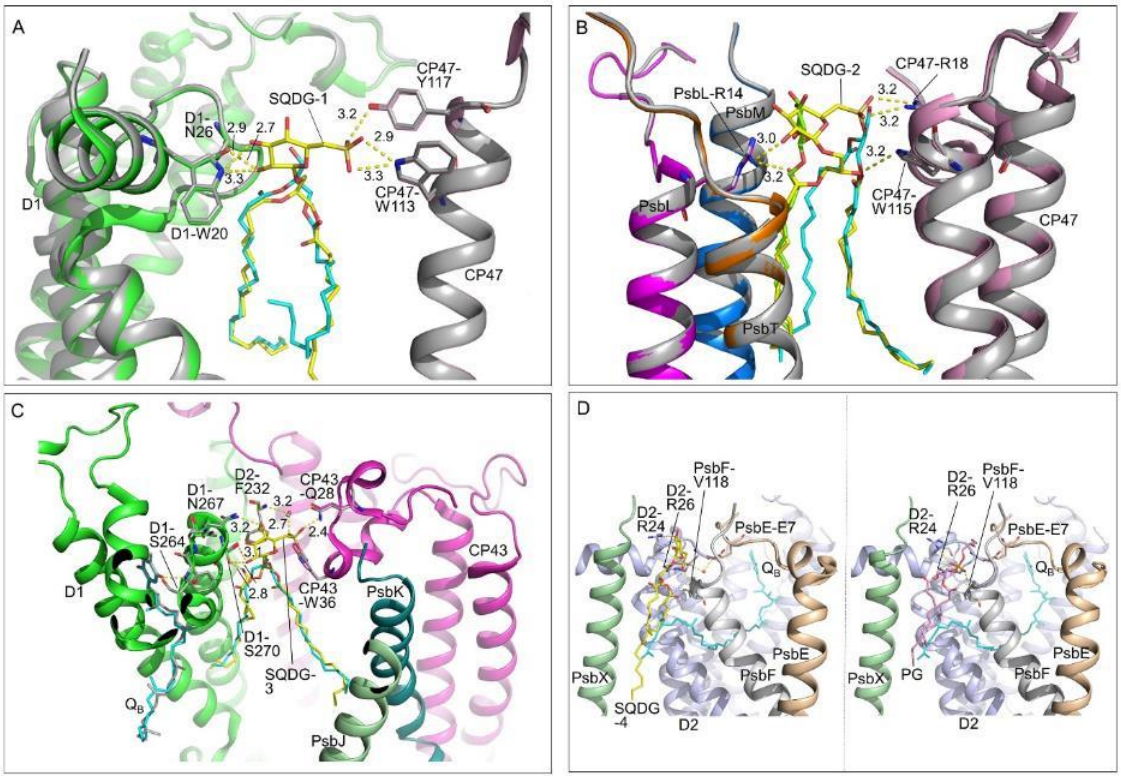

Fig. 3-11 Comparisons of the structures of the four SQDG-binding sites between WT and the ΔSQDG mutant. *A* and *B.* Comparison of the structure of the SQDG-1 and SQDG-2 binding sites between WT and the ΔSQDG mutant. The structures of the WT and the mutant are superimposed, where residues of WT are colored and those of the mutant are depicted in grey. SQDGs are depicted in yellow, and the unknown lipid molecules in the mutant are depicted in cyan. *C.* Comparison of the structure of the SQDG-3 binding site between WT and the ΔSQDG mutant. For the sake of clarity, only residues of WT are shown except the unknown lipid of the mutant which is shown in cyan. *D.* Comparison of the structure of the SQDG-4 binding site between WT (left side) and the ΔSQDG mutant (right side). In all panels except panel D, the hydrogen-bond distances are shown in Å. In panel D, the hydrogen-bond distances were omitted for the sake of clarity.

The head group of SQDG-3 is surrounded by D1 and CP43, and one of its fatty acid tails is close to PsbJ, PsbK. The head of SQDG-3 is hydrogen-bonded with D1-Asn267, D1-Ser270, CP43-Gln28, CP43-Trp36 directly, and with D2-Phe232 through a water molecule (Fig. 3-11C). Due to the replacement of SQDG-3 by an unknown diacyl chain, these hydrogen-bonds were also broken in the ΔSQDG mutant. Modelling of a PG molecule in this site does not help to maintain most of the hydrogen-bonds with the surrounding residues (Fig. 3-12F). Although the structure of the surrounding residues was not changed significantly again by this replacement, two residues hydrogen-bonded to SQDG-3, namely, D1-Asn267, D1-Ser270, are located in a loop close to the head group of Q_B, where D1-Ser264 is hydrogen-bonded to the head of Q_B (Fig. 3-11C). The breakage of the hydrogen-bonds between D1-Asn267, D1-Ser270 and SQDG-3 may affect the interaction of this loop with Q_B, thereby affecting the exchange process of this bound quinone acceptor with free plastoquinone.

SQDG-4 is surround by D2, PsbF and PsbX, and its fatty acid tails are close to the isoprenoid tail of Q_B. In the WT, the head group of SQDG-4 is hydrogen-bonded with D2-Arg24, D2-Arg-26, PsbF-Val118 directly, and with PsbE-Glu7 through a water molecule (Fig. 3-11D, left side). In the ΔSQDG mutant, this SQDG is clearly replaced by a PG molecule, which maintains the hydrogen-bonds with D2-Arg24, D2-Arg26 and PsbF-Val18 (Fig. 3-11D, right side). The phosphorus atom is fitted in the same position as that of the sulfur atom in SQDG of the WT structure. Only the water molecule connecting SQDG-4 and PsbE-Glu7 was lost in the mutant, resulting in the loss of the hydrogen-bond between the PG molecule and PsbE-Glu7. The tail of the PG molecule is also located in a position very similar to that of SQDG-4 and close to the tail of Q_B. Thus, the function of SQDG-4 may well be maintained by the PG molecule in this binding site.

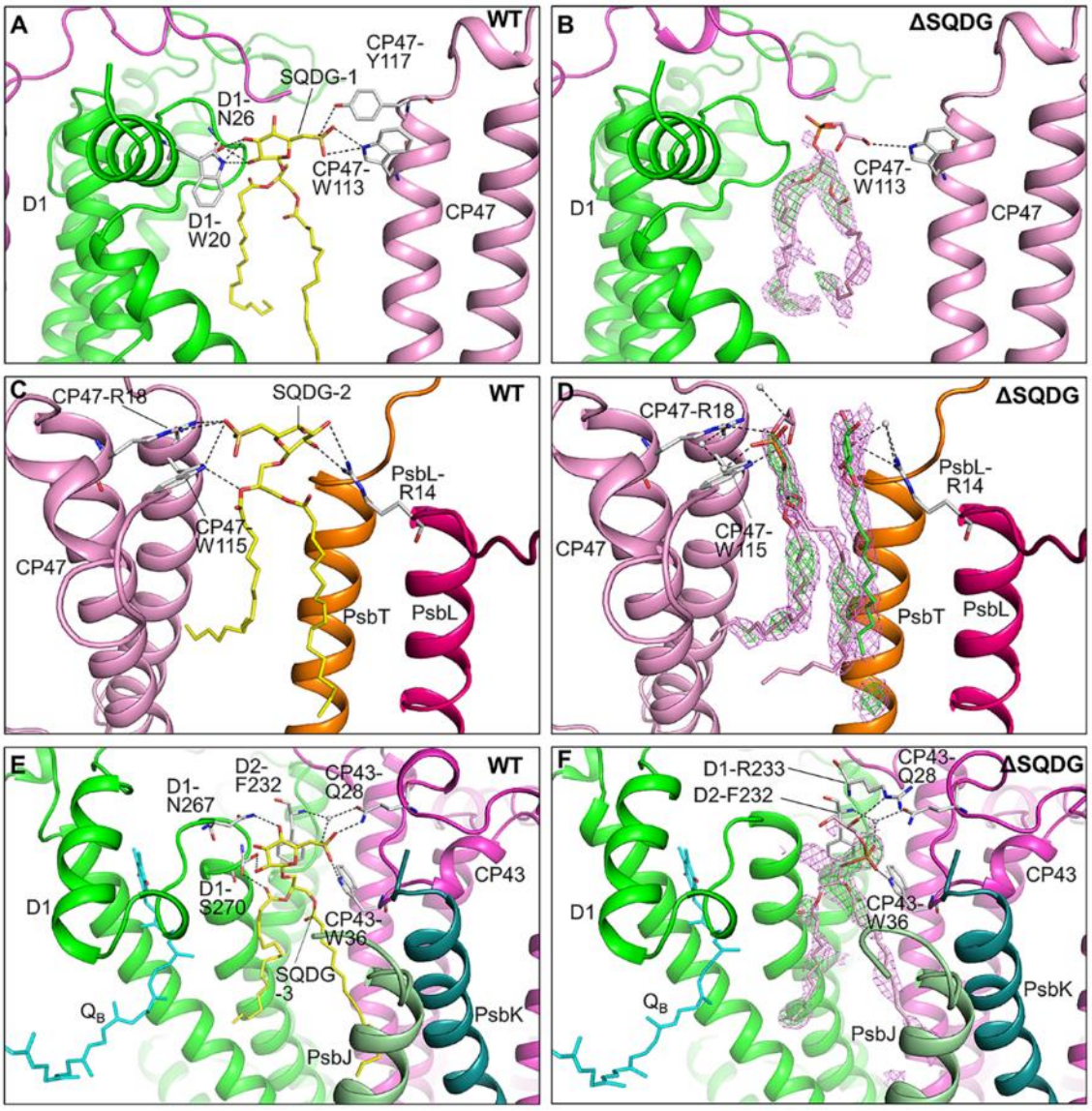

Fig. 3-12 Modelling of PG molecules into the three SQDG binding sites and their possible hydrogen-bonds with nearby residues in the mutant. The three SQDG-binding sites (SQDG-1, SQDG-2, SQDG-3) were tentatively assigned to PG molecules (panels B, D and F) and superimposed with their 2|*Fo*|-|*Fc*| maps contoured at 0.8 σ (violet) and SQDGs-omitted |*Fo*|-|*Fc*| maps (green, positive) contoured at 3.5 σ, respectively, in the mutant PSII dimers, and compared with the structures of SQDGs in the WT PSII (panels A, C and E). Dotted lines indicate the hydrogen-bonds between SQDGs and nearby residues in the WT-PSII and possible hydrogen-bonds between PG and nearby residues (including water molecules) in the ΔSQDG-PSII. PG, SQDG and β-DDM molecules are depicted as sticks in pink, yellow and green, respectively

DISCUSSIONS

In the present study, we examined the effects of depletion of SQDG on the stability and activity of PSII dimer from the thermophilic cyanobacterium *T. elongatus*. FTIR and TL measurements showed that the depletion of SQDG has little effects on both the electron donor and accepter sides, which is in agreement with the results of structural analysis showing that the overall structure of the ΔSQDG-PSII is very similar to of the WT-PSII. A slight decrease in the oxygen-evolving activity was observed upon depletion of SQDG, which is presumably caused by the effects on the Q_B exchange process at the acceptor side, as shown by the DL measurements. An important effect of SQDG depletion is the destabilization of PSII dimer, leading to a significant increase in the PSII monomer. This is in agreement with the previous results (3). However, our purification procedures used still gave rise to a certain fraction of PSII dimers, which is different from the previous analysis showing that almost all of the PSII dimer was lost in the mutant (3).

The slight effects of SQDG on PSII activity observed in the thermophilic cyanobacterium in the present and previous studies (3) are similar to those observed with other organisms (except *Synechocystis* 6803), and may be taken as evidence to indicate that SQDG is dispensable for the photosynthetic growth and PSII activity (13). However, our structural analysis of the ΔSQDG mutant PSII clearly showed that all of the 4 SQDG-binding sites have been occupied by other lipid molecules. Among them, the lipid molecules replacing SQDG-1 to SQDG-3 could not be identified unambiguously from the electron density map. In the structure of WT-PSII analyzed at the same resolution, the 2|*Fo*|-|*Fc*| and |*Fo*|-|*Fc*| maps showed clear densities for these SQDG binding sites (Fig. 3-10A, C, D). This suggests that the alternative lipid molecules do not fit well with these sites and therefore cannot bind to the nearby residues specifically, resulting in the distortions in the electron densities. On the other hand, the electron densities for the fatty acid tails in these three sites are more or less observed, allowing us to assign the positions of the tails based on the electron density map. However, the electron densities corresponding to the head group of the unknown lipids were very weak or not observed, suggesting that binding of the new, unknown lipids to these three sites are non-specific and weak, which in turn indicates that these sites are evolved to accommodate SQDG best. Since MGDG and DGDG have relatively larger head groups than that of PG, we expect that it would be easier to visualize them if these sites are replaced by MGDG and/or DGDG. The absence of electron densities for the head groups may therefore suggest that these sites have mostly been replaced by PG. This is in agreement with the results of lipid analysis

showing that the PG content is increased significantly in the mutant PSII whereas those of MGDG and DGDG remained unchanged in comparison with the WT. The replacement of SQDG by PG in the mutant also agrees with a number of studies reported previously that phosphate is required to maintain the photosynthetic growth of mutants defective in SQDG synthesis (3, 12, 19, 39). On the other hand, the binding site for SQDG-4 was shown to be replaced by a PG molecule based on its electron density as well as the anomalous signal of the phosphorus atom.

The effects of SQDG depletion on the stability of PSII dimer and exchange of bound Q_B can be explained based on the results of structural analysis. Among the four SQDG molecules in PSII, SQDG-1 and SQDG-2 are located in the interface between the two PSII monomers and contribute to the formation of the dimer by connecting different subunits from the two monomers by a number of hydrogen-bonds formed between the head group of SQDG and nearby amino acid residues. Replacement of these two lipids by unknown lipids resulted in the breakage of the hydrogen-bonds. This may have caused destabilization of the PSII dimer, resulting in the increase of PSII monomer observed in the present and previous studies (3). Even if these two sites are replaced by PG in the mutant, due to its different structure of the head group as well as the weak binding to the nearby residues, most of the hydrogen-bonds may have been weakened or lost, resulting in the destabilization of the PSII dimer. This indicates that only SQDG can fulfill the full function to stabilize the PSII dimer in these two binding sites, and replacement by other lipids was not enough to fully compensate for the function of SQDGs.

SQDG-3 is located at a position close to Q_B, and its head group forms hydrogen-bonds with residues of a D1 loop (including D1-Ser270) that also forms hydrogen-bonds with the head group of Q_B (D1-Ser264). Replacement of this SQDG by an unknown lipid in the ΔSQDG mutant broke the hydrogen-bonds with the D1 loop, which may in turn affect the hydrogen-bonds between this D1 loop and the head of Q_B. This may be the cause for the changes observed in the Q_B exchange property in the mutant. Indeed, alteration of D1-Ser270 to alanine has been shown to affect the binding of bromoxynil to the Q_B binding site, resulting in a phenotype that is more susceptible to bromoxynil (40). Similar high sensitivity to herbicides was also reported previously in several species depleted of SQDG (14, 16). This suggests that the interactions of D1-Ser270 and other nearby residues with SQDG may provide a cap to protect the Q_B-binding site, and breakage of these interactions results in the destabilization of the Q_B-binding site, leading to the easy exchange by and higher sensitivity toward herbicides.

Finally, SQDG-4 was replaced by a PG molecule, and hydrogen-bonds of SQDG-4 with nearby

amino acid residues were largely maintained by the PG molecule. Thus, this replacement may not affect the PSII activity significantly.

In conclusion, we succeeded in the crystallization and its structure analysis at a high resolution with PSII dimers derived from a single lipid deletion mutant. The apparent effects of SQDG deletion on the growth and PSII activity of the thermophilic cyanobacterium are very small. However, structural analysis revealed that all of the four SQDG-binding sites were replaced by other lipids, mostly PG, which apparently have contributed to maintain the photosynthetic growth and activity of the mutant. This in turn suggests that the four SQDG-binding sites have to be occupied by some lipid molecules, with SQDG being the optimum choice and its functions can be compensated for in part by other lipids, mostly PG. However, the replacement cannot completely reproduce the hydrogen-bonds mediated by SQDG between the A- and B-monomers and in the vicinity of Q_B, leading to the decrease in the PSII dimer stability and alterations of the Q_B exchange property. Thus, these sites are evolved to best accommodate SQDG. Our results thus demonstrated that the effects of lipid depletion and their functions in membrane proteins and their complexes must be examined on the basis of structural analysis.

REFFERENCES

1. Sato, N., and Wada, H. (2009) in *Lipids in Photosynthesis*, *Essential and Regulatory Functions* (Wada, H and Murata, N., eds), pp. 157–177, Springer, Dordrecht, Germany.
2. Mizusawa, N., and Wada, H. (2012) The role of lipids in photosystem II. *Biochim. Biophys. Acta*, **1817**, 194–208.
3. Endo, K., Kobayashi, K., and Wada, H. (2016) Sulfoquinovosyldiacylglycerol has an essential role in *Thermosynechococcus elongatus* BP-1 under phosphate-deficient conditions. *Plant Cell Physiol.*, **57,** 2461–2471.
4. Kobayashi, K., and Wada, H. (2016) in *Lipids Plant Algae Dev.,* (Nakamura, Y., and Li-Beisson, Y., eds), pp. 103–125, Springer, Switzerland.
5. Umena, Y., Kawakami, K., Shen, J.-R., and Kamiya, N. (2011) Crystal structure of oxygen-evolving photosystem II at a resolution of 1.9 Å. *Nature*, **473,** 55–60.
6. Qin, X., Suga, M., Kuang, T., and Shen, J.-R. (2015) Structural basis for energy transfer pathways in the plant PSI-LHCI supercomplex. *Science*, **348,** 989–995.
7. Mazor. Y., Borovikova, A., Caspy. I., and Nelson, N. (2017) Structure of the plant photosystem I supercomplex at 2.6 Å resolution. *Nat. Plants*, **3:17014**.
8. Hasan, S. S., and Cramer, W. A. (2014) Internal lipid architecture of the hetero-oligomeric cytochrome b_6f complex. *Structure*, **22,** 1008–1015.
9. Hagio, M., Gombos, Z., Várkonyi, Z., Masamoto, K., Sato, N., Tsuzuki, M., and Wada, H. (2000) Direct evidence for requirement of phosphatidylglycerol in photosystem II of photosynthesis. *Plant Physiol.*, **124,** 795–804.
10. Itoh, S., Kozuki, T., Nishida, K., Fukushima, Y., Yamakawa, H., Domonkos, I., Laczkó-Dobos, H., Kis, M., Ughy, B., and Gombos, Z. (2012) Two functional sites of phosphatidylglycerol for regulation of reaction of plastoquinone Q_B in photosystem II. *Biochim. Biophys. Acta*, **1817,** 287–297.
11. Güler, S., Seeliger, A., Härtel, H., Renger, G., and Benning, C. (1996) A null mutant of *Synechococcus* sp. PCC7942 deficient in the sulfolipid sulfoquinovosyl diacylglycerol. *J. Biol. Chem.*, **271,** 7501–7507.
12. Yu, B., Xu, C., and Benning, C. (2002) *Arabidopsis* disrupted in SQD2 encoding sulfolipid synthase is impaired in phosphate-limited growth. *Proc. Natl. Acad. Sci. U.S.A.*, **99,** 5732–5737.
13. Sato, N., Kamimura, R., and Tsuzuki, M. (2016) Dispensability of a sulfolipid for photoautotrophic cell growth and photosynthesis in a marine cyanobacterium, *Synechococcus* sp. PCC 7002. *Biochem.*

Biophys. Res. Commun., **477,** 854–860.

14. Yu, B., and Benning, C. (2003) Anionic lipids are required for chloroplast structure and function in *Arabidopsis*. *Plant J.*, **36,** 762–770.
15. Sato, N., Sonoike, K. Tsuzuk, M. and Kawaguchi, A. (1995) Impaired photosystem II in a mutant of *Chlamydomonas reinhardtii* defective in sulfoquinovosyl diacylglycerol. *Eur. J. Biochem.*, **234,** 16–23.
16. Minoda, A., Sato, N., Nozaki, H., Okada, K., Takahashi, H., Sonoike, K., and Tsuzuki, M. (2002) Role of sulfoquinovosyl diacylglycerol for the maintenance of photosystem II in *Chlamydomonas reinhardtii*. *Eur. J. Biochem.*, **269,** 2353–2358.
17. Minoda, A., Sonoike, K., Okada, K., Sato, N., and Tsuzuki, M. (2003) Decrease in the efficiency of the electron donation to tyrosine Z of photosystem II in an SQDG-deficient mutant of *Chlamydomonas*. *FEBS Lett.*, **553,** 109–112.
18. Sato N., Aoki M., Maru Y., Sonoike K., Minoda A., and Tsuzuki M. (2003) Involvement of sulfoquinovosyl diacylglycerol in the structural integrity and heat-tolerance of photosystem II. *Planta*, **217,** 245–251.
19. Aoki, M., Sato, N., Meguro, A., and Tsuzuki, M. (2004) Differing involvement of sulfoquinovosyl diacylglycerol in photosystem II in two species of unicellular cyanobacteria. *Eur. J. Biochem.*, **271,** 685–693.
20. Aoki, M., Tsuzuki, M., and Sato, N. (2012) Involvement of sulfoquinovosyl diacylglycerol in DNA synthesis in *Synechocystis* sp. PCC 6803. *BMC Res. Notes*, **5,** 98.
21. Guskov, A., Kern, J., Gabdulkhakov, A., Broser, M., Zouni, A., and Saenger, W. (2009) Cyanobacterial photosystem II at 2.9-Å resolution and the role of quinones, lipids, channels and chloride. *Nat. Struct. Mol. Biol.*, **16,** 334–42.
22. Suga, M., Akita, F., Hirata, K., Ueno, G., Murakami, H., Nakajima, Y., Shimizu, T., Yamashita, K., Yamamoto, M., Ago, H., and Shen, J.-R. (2015) Native structure of photosystem II at 1.95 Å resolution viewed by femtosecond X-ray pulses. *Nature*, **517,** 99–103.
23. Broser, M., Gabdulkhakov, A., Kern, J., Guskov, A., Müh, F., Saenger, W., and Zouni, A. (2010) Crystal structure of monomeric photosystem II from *Thermosynechococcus elongatus* at 3.6-Å resolution. *J. Biol. Chem.*, **285,** 26255–26262.

24. Noguchi, T., Katoh, M., and Inoue Y. (2002) A new system for detection of thermoluminescence and delayed luminescence from photosynthetic apparatus with precise temperature control. *Spectroscopy*, **16,** 89–94.
25. Suzuki, H., Sugiura, M., and Noguchi, T. (2012) Determination of the miss probabilities of individual S-state transitions during photosynthetic water oxidation by monitoring electron flow in photosystem II using FTIR spectroscopy. *Biochemistry*, **51,** 6776–6785.
26. Bligh, E.G., and Dyer, W.J. (1959) A rapid method of total lipid extraction and purification. *Can. J. Biochem. Physiol.*, **37,** 911–917.
27. Wada, H., and Murata, N. (1989) *Synechocystis* PCC6803 mutants defective in desaturation of fatty acids. *Plant Cell Physiol.*, **30,** 971–9780.
28. Sakurai, I., Shen, J.-R., Leng, J., Ohashi, S., Kobayashi, M., and Wada, H. (2006) Lipids in oxygen evolving photosystem II complexes of cyanobacteria and higher plants. *J. Biochem.,* 140, 201–209.
29. Shen, J.-R., and Kamiya, N. (2000) Crystallization and the crystal properties of the oxygen-evolving photosystem II from *Synechococcus vulcanus*. *Biochemistry*, **39,** 14739-14744.
30. Kabsch, W. (1993) Automatic processing of rotation diffraction data from crystals of initially unknown symmetry and cell constants. *J. Appl. Crystallogr.*, **26,** 795–800.
31. Vagin, A., and Teplyakov, A. (1997) MOLREP: an automated program for molecular replacement. *J. Appl. Crystallogr.*, **30,** 1022–1025.
32. Murshudov, G. N., Vagin, A. A., and Dodson, E.J. (1997) Refinement of macromolecular structures by the maximum-likelihood method. *Acta Crystallogr. D Biol. Crystallogr.*, **D53,** 240–255.
33. Kabsch, W., (1976) A solution for the best rotation to relate two sets of vectors. *Acta Crystallogr.*, **A32,** 922–923.
34. Winn, M. D., Ballard, C. C., Cowtan, K. D., Dodson, E. J., Emsley, P., Evans, P. R. R., Keegan, M., Krissinel, E. B., Leslie, A. G. W., McCoy, A., McNicholas, S. J., Murshudov, G. N., Pannu, N. S., Potterton, E. A., Powell, H. R., Read, R. J., Vagin, A., and Wilson, K. S. (2011) Overview of the CCP4 suite and current developments. *Acta Crystallogr. D Biol. Crystallogr.*, **D67,** 235-242.
35. Emsley, P., and Cowtan, K. (2004) Coot: model-building tools for molecular graphics. *Acta Crystallogr. D Biol. Crystallogr.*, **D60,** 2126–2132.
36. DeLano, W. L. (2015) *The PyMOL Molecular Graphics System,* Version 1.8, Delano Scientific LLC, San Carlos, CA.

37. Noguchi, T., and Sugiura, M. (2001) Flash-induced Fourier transform infrared detection of the structural changes during the S-state cycle of the oxygen-evolving complex in photosystem II. *Biochemistry*, 40, 1497–1502.
38. Suzuki, H., Taguchi, Y., Sugiura, M., Boussac, A., and Noguchi, T. (2006) Structural perturbation of the carboxylate ligands to the manganese cluster upon Ca^{2+}/Sr^{2+} exchange in the S-state cycle of photosynthetic oxygen evolution as studied by flash-induced FTIR difference spectroscopy. *Biochemistry*, **45,** 13454–13464.
39. Sugimoto, K., Midorikawa, T., Tsuzuki, M., and Sato, N. (2008) Upregulation of PG synthesis on sulfur-starvation for PS I in *Chlamydomonas*. *Biochem. Biophys. Res. Commun.*, **369,** 660-665.
40. Sugiura, M., Kato, Y., Takahashi, R., Suzuki, H., Watanabe, T., Noguchi, T., Rappaport, F., and Boussac, A. (2010) Energetics in photosystem II from *Thermosynechococcus elongatus* with a D1 protein encoded by either the *psbA1* or *psbA3* gene. *Biochim. Biophys. Acta*, **1797,** 1491–1499.

GENERAL CONCLUSIONS

In this study, I performed crystallization of PSII micro-crystals, screening of the optimum crystallization and cryo-protectant conditions in order to obtain high resolution diffraction datasets from the TR-SFX pump-probe experiments with XFEL pulses of SACLA, as well as functional and structural studies of a mutant PSII lacking SQDG. The PSII micro-crystals prepared in this study were successfully used to obtain reasonably high resolution datasets for the dark-stable S_1-state and 2 flashes induced S_3-state by TR-SFX, allowing us to observe the structural changes of the Mn_4CaO_5 cluster accompanying the S_1-S_3 transition. Among the structural changes observed, the most important one is the insertion of a new oxygen atom, O6 close to O5 in the Mn_4CaO_5 cluster in the 2 flash-induced PSII structure. This result suggests that O6 and O5 may form the O=O bond, and O5 is one of the substrate oxygen atoms for formation of the molecular oxygen. However, it remains unclear as to how the O=O bond is actually formed as well as how molecular oxygen is released. In order to solve this problem, it is necessary to solve the S-state structures beyond the S_3-state, namely the S_4 and S_0-states. Indeed, we tried to collect the diffraction data induced by 3 flashes illumination with the same PSII micro-crystals and same method, however, we were unable to detect any structural changes beyond the S_3-state. This was found to be caused by the high concentration of PEG and glycerol used for the cryo-protection of the PSII micro-crystals to obtain the high resolution, which is in agreement with a recent report showing that the efficiency of $S_2 \rightarrow S_3$ transition in the crystal state is lowered by treatment with a high concentration of PEG (1).

To resolve this problem, S-state transitions of PSII treated with several cryo-protectants were examined with TL. The results suggested that high concentration of PEG affected the state tarnation of $S_2 \rightarrow S_3$ in agreement with previous reports. The TL results also demonstrated inhibition of the $S_3 \rightarrow S_0$ state transition by PEG. As this effect was already observed with PSII dimer solution samples, it will happen regardless of the crystal packing pattern and distribution of PSII particles within the crystals. This illustrates why structural changes were not observed upon 3 flashes illumination under the previous condition of cryoprotectant. Thus, it is important to find a cryo-protectant condition that allows an efficient S-state transition and yet give high resolution of the PSII micro-crystals. To achieve this goal, several different types of cryo-protectants were screened for their effects on the S-state transitions by TL, and it was found that 20% DMSO alone had almost no effects on the TL glow curves and the oscillation pattern of the TL intensities vs flash numbers. Since 20% DMSO alone is not enough to serve

as the cryo-protectant for the PSII crystals, a combination of 20% DMSO with a mixture of PEG1450 and PEG500 MME were examined for their effects on the S-state transitions. The results showed that a combination of 20% DMSO and up to 14% PEGmix had no significant effects on the TL properties, whereas increase of the PEGmix concentration beyond 14% affected the TL intensities. Thus, a combination of 20% DMSO and 14% PEGmix may be used as the cryo-protectant. However, this combination may still not be enough to give the best resolution for the PSII micro-crystals, thus, other cryoprotectant conditions containing DMSO need to be screened that will give the best resolution without affecting the PSII activity.

SQDG is one type of the lipid molecules bound to the PSII complex, and 4 SQDG molecules were found to associate with a PSII monomer. In order to examine the functions of SQDG in PSII, PSII dimer from an SQDG-deletion mutant was purified, and its functions and structure were analyzed. It was found that the PSII activity was only slightly affected by the deletion of SQDG. However, structural analysis of the ΔSQDG-PSII showed that all of the 4 SQDG molecules bound to PSII were replaced by some other lipid molecules, among which, one is identified to be PG unambiguously whereas the other 3 were not identified unambiguously. Lipid analysis showed that the content of PG was apparently increased in the ΔSQDG mutant, suggesting that the other 3 SQDB-binding sites are also occupied by the PG molecules. Spectroscopic analysis suggested that the exchange of Q_B with free PQ was retarded in the SQDG-deletion mutant, and PSII dimer was destabilized significantly, resulting in a large increase in the PSII monomer in the ΔSQDG-PSII. These results suggest that PG may partially substitute for the function of SQDG, but the full functioning and stability of PSII is maintained only when SQDGs are bound to their original sites. Since two SQDG molecules are found in the monomer-monomer interface in the PSII dimer structure, destabilization of the PSII dimer may be caused by the replacement of SQDG by PG in these sites. However, the structure of ΔSQDG-PSII showed no significant changes in the B-factors of the residues around these regions, and there were also no apparent conformational changes of the amino acid residues in these regions. Thus, the mechanism of PSII dimer destabilization caused by the loss of SQDG in the monomer-monomer interface needs to be examined by other means such as the thermal stability measured by differential scanning calorimetry (2) and/or structural stability by treatment with detergent and heat.

REFFERENCES

1. Kato, Y., Akita, F., Nakajima, Y., Suga, M., Umena, Y., Shen, J.-R., and Noguchi, T. (2018) Fourier transform infrared analysis of the S-state cycle of water oxidation in the microcrystals of photosystem II. *J. Phys. Chem. Lett.,* **9**, 2121–2126.
2. Zimmermann, K., Heck, M., Frank, J., Kern, J., Vass, I., and Zouni, A. (2006) Herbicide binding and thermal stability of photosystem II isolated from *Thermosynechococcus elongatus*. *Biochim. Biophys. Acta,* **1757**, 106–114.

ACKOWLDGEMENTS

I am very grateful to Prof. Yuichiro Takahashi and Prof. Jian-Ren Shen for their important advices, warm supports and encouragements for my works. I greatly thank Dr. Akita for his support on the crystallization of PSII, and Drs. Umena and Suga for advices on the methods of crystal structure analysis. I would also like to thank Prof. Hajime Wada of Tokyo University and Dr. Kaichiro Endo of Jagiellonian University of Poland for their providing us with the SQDG-deletion mutant and assistances in the analysis of lipids of PSII, and Prof. Takumi Noguchi of Nagoya University, Dr. Miwa Sugiura of Ehime University, and Dr. Ryo Nagao of Okayama University for their helps in the analyses of the functions of the SQDG-deletion mutant. I also thank the Iwata group of Kyoto University and staff members at SACLA beamline for their helps in the SFX experiment, and the staff members of BL41XU, BL44XU and BL38XU for their helps in screening of the micro-crystal quality and diffraction data collection from the ΔSQDG-PSII crystal. Finally, I thank all the members of the Shen laboratory of Okayama University and my family for their generous support.